$B^0 \to J/\psi\, K_S^0, K_S^0 \to \pi^0\pi^0$ at the *BABAR* Experiment

David Payne

November 2001

University of Liverpool
Department of Physics

Thesis submitted to University of Liverpool for the degree of Doctor of Philosophy

Abstract

This thesis describes the study of the decay $B^0 \rightarrow J/\psi\ K^0_S$, where the K^0_S $\rightarrow \pi^0\pi^0$, using data taken at the *BABAR* experiment at SLAC. B^0 mesons are fully reconstructed via this decay. These reconstructed B^0s are used to measure the branching fraction BR($B^0 \rightarrow J/\psi\ K^0$):

$$BR(B^0 \rightarrow J/\psi K^0) = (9.6 \pm 1.5_{stat} \pm 0.7_{syst}) \times 10^4$$

This result is consistent with other measurements.

Using these reconstructed B^0s combined with a measurement of its sister B^0's flavour and a measurement of Δt (the decay time difference), a measurement of the Unitary Triangle parameter sin2β was made:

$$\sin 2\beta = 0.76 \pm 0.52_{stat} \pm 0.12_{syst}$$

This analysis contributed to the first observation of CP violation in the B system. This observation was made by BaBar in July 2001 and is published in [1].

"I'm great me"

— The boy Lard

Contents

Acknowledgements

I would like to thank Professor Erwin Gabathuler for giving me the chance to do this PhD, and for his help and encouragement over the years.

I would also like to thank Dr. Christos Touramanis, my supervisor out at SLAC. He taught me how to do this job, and had faith in my ability to do it (against all evidence to the contrary). I hope I've proved him right.

There are a great many people in the BaBar collaboration whose work I've relied on or whose help I've needed - too many to mention here. Thank you to you all.

Thanks to my fellow Slackers, a great group of people who got each other through the terrible hardship of being stuck in California for a year.

I'd particularly like to thank my fellow HEP students here at Liverpool who I've shared an office with for this past year. Andy Washbrook (whose hangovers have amused us all), Mark Tobin (bimble, hat, sombrero), Michael George (what does gan canny mean, exactly?), John Kennedy (strange lad - nice jumper though), Jake (be afraid) and Michael Kay (who I shared a year out at SLAC with). What can I say, except its your round, Andy.

My parents have a lot to answer for. My Mum is probably responsible for my interest in Particle Physics, due to accidentally leaving a book of hers by Glashow within reach of an impressionable child. Dad: sorry, but my chapter on "Payne's theory of infinite minuteness" got cut. The world just isn't ready for it yet. Thank you to you both.

Finally, I'd like to thank Sarah. And may I recommend the soon to be published "Evolution of Brightest Cluster Galaxies in X-Ray Clusters" (Brough et al.) 2001 MNRAS, a veritable rollercoaster of a paper, I laughed, I cried. By the way, isn't [9] the best title for a paper ever?

Thank you Sarah.

Chapter 1

Introduction

1.1 The measurement of $\sin 2\beta$ from $B^0 \rightarrow J/\psi K_s^0$, $K_S^0 \rightarrow \pi^0\pi^0$

CP, the simultaneous inversion of both Charge and Parity, was regarded as an inherent symmetry of the universe until 1964 [2], when it was observed to be broken in the neutral kaon meson system. Since then, it has been shown that violation of CP symmetry is expected in the Standard Model if more than two families of quarks exist . The Standard Model also predicted that a large violation of CP symmetry would occur within the B system, but until recently this had not been observed.

The B system offers opportunities to study CP violation in great detail. Measurements can be made that relate directly to theoretical parameters, and the Standard Model makes very clear predictions with small theoretical uncertainties. Largely for this reason, interest in B physics was great enough to build experiments entirely dedicated to the production and study of B mesons - B Factories. Two currently exist, *BABAR* at SLAC and BELLE at KEK.

β is a parameter describing CP violation in the B system[1]. Using a sample of events where a $B^0(\overline{B}^0)$ has decayed into an appropriate CP eigenstate, it is possible to extract a measurement of $\sin 2\beta$ using measurements of decay time

[1] α and γ complete the description in the Standard Model (see section 2.4.4).

and of B flavour. At *BABAR* , the CP eigenstates used to measure sin2β were $J/\psi K_S^0$, $\psi(2S)K_S^0$, $\chi_{c1}K_S^0$, $J/\psi K_L$ and $J/\psi K^{*2}$. The largest contribution of events came from the eigenstate $J/\psi K_S^0$, which was reconstructed both when the K_S^0 decayed to $\pi^+\pi^-$and when it decayed to $\pi^0\pi^0$. This thesis concerns events where $B^0 \to J/\psi K_s^0$, and the $K_S^0 \to \pi^0\pi^0$. These events are used to extract a measurement of sin2β.

The sin2β analysis described in this thesis is included in [1], where it is combined with all the other event samples listed above.

1.2 The Branching Fraction $BR(B^0 \to J/\psi K^0)$

B meson decays to two body final states containing Charmonium (such as $J/\psi K_S^0$) allow a very precise examination of electroweak transitions. They also permit examination of the dynamics of strong interactions in heavy meson systems. As mentioned in Section 1.1 such decays can be used to measure CP violation, but they also permit study of the non-perturbative, long range regime of QCD. The factorization hypothesis [4, 5] is generally used in calculations of hadronic decay amplitudes, but it is not at all certain that it is applicable for $B \to charmonium + X$ decays. This has been the subject of many recent phenomenological analyses [8, 9, 10]. In this thesis, a measurement of the Branching Ratio $BR(B^0 \to J/\psi K^0)$ is made using events where $B^0 \to J/\psi K_s^0$, and the $K_S^0 \to \pi^0\pi^0$. This Branching Ratio analysis has been published as part of [6]. $BR(B^0 \to J/\psi K^0)$ can be compared to that predicted by the factorization hypothesis, or corrections to it, to determine their validity. It can also be used as an input for further phenomenological analyses.

[2] $J/\psi K^*$ is not a CP eigenstate, however when the K^* decays to $K_S^0\pi^0$ it is a mixture of two eigenstates whose relative amplitudes can be determined from an angular analysis, allowing a measurement of sin2β to be made.

Chapter 2

CP Violation in the B Meson System

2.1 Neutral Meson Mixing

In order to understand the CP asymmetry exhibited in the B system, it is necessary to first discuss the mixing of neutral mesons in general and the effect that the introduction of CP violation has on that mixing.

2.1.1 General Neutral Meson Mixing

The Schrödinger equation for a single particle can be written as

$$\frac{\partial|\psi\rangle}{\partial t} = -im|\psi\rangle \tag{2.1}$$

$(\hbar = c = 1)$, with the solution

$$|\psi(t)\rangle \propto e^{-imt} \tag{2.2}$$

This states that the wave function oscillates with a frequency dependent on the mass of the particle. If the particle is unstable, its amplitude decreasing according to an exponential decay law, an extra term appears:

$$\frac{\partial|\psi\rangle}{\partial t} = -im|\psi\rangle - \frac{1}{2}\Gamma|\psi\rangle \tag{2.3}$$

with the solution becoming

$$|\psi(t)\rangle \propto e^{-imt}e^{-\Gamma t/2} \tag{2.4}$$

This can be re-written as

$$\frac{\partial|\psi\rangle}{\partial t} = -iA|\psi\rangle \tag{2.5}$$
$$|\psi(t)\rangle \propto e^{-iAt} \tag{2.6}$$

where A is a complex number with $Re(A) = m$ and $Im(A) = -\Gamma/2$.

We now consider a general system of two states, which may have different masses and decay constants. They can mix into one another such that ψ_1 has a contribution proportional to the amplitude of ψ_2, and vice versa. This leads to matrix elements such as:

$$\mathcal{M}_{12} = \langle\psi_1|\widehat{H}|\psi_2\rangle = M_{12} - i\Gamma_{12}/2 \tag{2.7}$$

where M_{ij} and Γ_{ij} are elements of mass and decay matrices respectively. There are now two equations

$$i\frac{\partial}{\partial t}\begin{pmatrix} |\psi_1\rangle \\ |\psi_2\rangle \end{pmatrix} = \begin{pmatrix} \mathcal{M}_{11} & \mathcal{M}_{12} \\ \mathcal{M}_{21} & \mathcal{M}_{22} \end{pmatrix}\begin{pmatrix} |\psi_1\rangle \\ |\psi_2\rangle \end{pmatrix} \tag{2.8}$$

representing the coupled modes. Starting from an initially pure state ψ_1, at any time in the future you will in general have a mixture of $\psi_1$and ψ_2. However, the modes can always be decoupled by diagonalising the matrix $\mathcal{M}$ to give the mass eigenstates.

2.1.2 Particle/Anti-particle Neutral Meson Mixing (CP Symmetric)

If we consider $|\psi\rangle$ $|\overline{\psi}\rangle$ (i.e. a particle - anti particle pair) instead of $|\psi_1\rangle$ $|\psi_2\rangle$, CPT invariance requires that the masses and total widths of the two states must be equal, making the diagonal elements of $\mathcal{M}$ equal. If we impose CP symmetry, the off diagonal elements must also be equal:

$$i\frac{\partial}{\partial t}\begin{pmatrix} |\psi\rangle \\ |\overline{\psi}\rangle \end{pmatrix} = \begin{pmatrix} A & B \\ B & A \end{pmatrix}\begin{pmatrix} |\psi\rangle \\ |\overline{\psi}\rangle \end{pmatrix} \tag{2.9}$$

Diagonalizing gives eigenvalues of A+B and A-B. The two decoupled modes are

$$|\psi_+\rangle = \frac{1}{\sqrt{2}}(|\psi\rangle + |\overline{\psi}\rangle) \tag{2.10}$$

$$|\psi_-\rangle = \frac{1}{\sqrt{2}}(|\psi\rangle - |\overline{\psi}\rangle) \tag{2.11}$$

with decoupled equations

$$i\frac{\partial|\psi_+\rangle}{\partial t} = M_+|\psi_+\rangle - i|\Gamma_+/2|\psi_+\rangle \tag{2.12}$$

$$i\frac{\partial|\psi_-\rangle}{\partial t} = M_-|\psi_-\rangle - i|\Gamma_-/2|\psi_-\rangle \tag{2.13}$$

which have the solutions

$$|\psi_+(t)\rangle \propto e^{-iM_+t}e^{-\Gamma_+t/2} \tag{2.14}$$

$$|\psi_-(t)\rangle \propto e^{-iM_-t}e^{-\Gamma_-t/2} \tag{2.15}$$

where

$$M_\pm = Re(A \pm B) \tag{2.16}$$

$$-\Gamma_\pm/2 = Im(A \pm B) \tag{2.17}$$

The original states $|\psi\rangle$ and $|\overline{\psi}\rangle$ are eigenstates of the strong interaction. These decoupled states are eigenstates of mass and CP. In particular

$$\widehat{CP}|\psi_\pm\rangle = \pm|\psi_\pm\rangle \tag{2.18}$$

2.1.3 Particle/Anti-Particle Neutral Meson Mixing (with *CP* Asymmetry)

To allow for the possibility of CP violation, the mixing equation must be rewritten as:

$$i\frac{\partial}{\partial t}\begin{pmatrix} |\psi\rangle \\ |\overline{\psi}\rangle \end{pmatrix} = \begin{pmatrix} A & \frac{p}{q}B \\ \frac{q}{p}B & A \end{pmatrix}\begin{pmatrix} |\psi\rangle \\ |\overline{\psi}\rangle \end{pmatrix} \tag{2.19}$$

where p and q are complex numbers obeying $|p|^2 + |q|^2 = 1$. Diagonalising gives the decoupled states:

$$|\psi_1\rangle = (p|\psi\rangle + q|\overline{\psi}\rangle) \tag{2.20}$$

$$|\psi_2\rangle = (p|\psi\rangle - q|\overline{\psi}\rangle) \tag{2.21}$$

with masses and widths:

$$M_{1,2} = Re(A \pm B) \tag{2.22}$$

$$-\Gamma_{1,2}/2 = Im(A \pm B) \tag{2.23}$$

2.2 Time Evolution of Neutral B_d Mesons

This section lays down a model independent description of B meson evolution. It goes on to show the connection between the experimental observable $a_{f_{CP}}$ and the CP violation parameter $Im\lambda_{f_{CP}}$.

2.2.1 Evolution of a B Meson

From equations 2.20 and 2.21, consider the B_L and B_H mass eigenstates of the neutral B_d meson as linear combinations of the flavor eigenstates.

$$|B_L\rangle = p|B^0\rangle + q|\overline{B^0}\rangle \tag{2.24}$$

$$|B_H\rangle = p|B^0\rangle - q|\overline{B^0}\rangle \tag{2.25}$$

The mass and width differences (Δm_B and $\Delta\Gamma_B$) between the two states are defined as:

$$\Delta m_B \equiv M_H - M_L \tag{2.26}$$
$$\Delta\Gamma_B \equiv \Gamma_H - \Gamma_L \tag{2.27}$$

The lifetime difference is expected to be negligible [11], and we will assume so here:

$$|\Delta\Gamma_B|/\Gamma_B < 10^{-2} \tag{2.28}$$

This limit comes from the observation that $\Delta\Gamma_B$ arises from decay channels that are common to B^0 and $\overline{B}^0$, which are known to have branching fractions of 10^{-3} or less. It should be noted that $\Delta\Gamma_B$ has not yet been experimentally measured, however this assumption is regarded as safe and model independent. $\Delta m_B/\Gamma_B$ has been measured[12]:

$$x_d \equiv \Delta m_B/\Gamma_B = 0.73 \pm 0.05 \tag{2.29}$$

From equations 2.28 and 2.29 it can be seen that $\Delta\Gamma_B \ll \Delta m_B$, independent of model. Hence it is logical to label mass eigenstates in terms of their mass - B_H and B_L refer to "heavy" and "light".

Any B state can be written as an admixture of B_H and B_L, with amplitudes that evolve as

$$a_H(t) = a_H(0)e^{-iM_H t}e^{-\Gamma_H t/2} \tag{2.30}$$
$$a_L(t) = a_L(0)e^{-iM_L t}e^{-\Gamma_L t/2} \tag{2.31}$$

It can be seen from equations 2.30 and 2.31 that a pure B^0 state at time $t = 0$ has $a_L(0) = a_H(0) = 1/(2p)$, and a pure $\overline{B^0}$ has $a_L(0) = -a_H(0) = 1/(2q)$.

Since the lifetime difference is expected to be negligible , we can use the approximation $\Gamma_H = \Gamma_L = \Gamma$, which gives the time evolution of these states as:

$$|B^0(t)\rangle = g_+(t)|B^0\rangle + (q/p)g_-(t)|\overline{B^0}\rangle \tag{2.32}$$
$$|\overline{B^0}(t)\rangle = (p/q)g_-(t)|B^0\rangle + g_+(t)|\overline{B^0}\rangle \tag{2.33}$$

where

$$g_+(t) = e^{-iMt}e^{-\Gamma t/2}cos(\Delta m_B t/2) \tag{2.34}$$
$$g_-(t) = e^{-iMt}e^{-\Gamma t/2}isin(\Delta m_B t/2) \tag{2.35}$$

and

$$M = (M_H + M_L)/2 \tag{2.36}$$

2.2.2 Evolution of the Coherent $B^0\overline{B}^0$ State

At *BABAR* , B^0 and $\overline{B}^0$mesons are produced exclusively through the process $e^+e^- \rightarrow \Upsilon(4S) \rightarrow B^0\overline{B}^0$. A $B^0\overline{B}^0$ pair produced at the $\Upsilon(4S)$ will be in a coherent $L = 1$ state. Each of the particles must evolve as described in 2.32 and 2.33. However, they must evolve in phase so that at any time there is exactly 1 B^0 and 1 $\overline{B}^0$. This continues until one decays, at which point the other continues to evolve.

From Equations 2.32 and 2.33 the two B state

$$S(t_1, t_2) = \frac{1}{\sqrt{2}}(|B_1^0(t,\theta)\rangle|\overline{B_2}^0(t,\theta)\rangle - \overline{|B_1}^0(t,\theta)\rangle|B_2^0(t,\theta)\rangle)\sin\theta \tag{2.37}$$

can be written as

$$\begin{aligned} S(t_1, t_2) =& \frac{1}{\sqrt{2}}e^{-(\Gamma/2+iM)(t_1+t_2)} \\ & \{\cos(\Delta m_B \Delta t/2)(B_1^0\overline{B_2}^0 - \overline{B_1}^0 B_2^0) \\ & - i\sin(\Delta m_B \Delta t/2)(\frac{p}{q}B_1^0 B_2^0 - \frac{q}{p}\overline{B_1}^0\overline{B_2}^0)\}\sin(\theta) \end{aligned} \tag{2.38}$$

where 1 and 2 are arbitrary labels for the Bs, θ is the angle between them and the beam in the $\Upsilon(4S)$ rest frame and Δt is the time difference between them, $t_1 - t_2$. Δt must be zero as the Bs evolve together, hence the equation reduces to $\frac{1}{\sqrt{2}}e^{-(\Gamma+2iM)t}(B_1^0\overline{B_2}^0 - \overline{B_1}^0 B_2^0)$.However, as soon as one particle decays, time "stops" for that particle and Δt becomes non-zero.

From equation 2.38, it is possible to obtain the amplitude for decays of B_1 to state f_1 at time t_1, and B_2 to state f_2 at time t_2:

$$\begin{aligned} A(t_1, t_2) =& \frac{1}{\sqrt{2}} e^{-(\Gamma/2+iM)(t_1+t_2)} \\ & \{\cos(\Delta m_B \Delta t/2)(A_1\overline{A_2} - \overline{A_1}A_2) - \\ & i\sin(\Delta m_B \Delta t/2)(\frac{p}{q}A_1A_2 - \frac{q}{p}\overline{A_1A_2})\}\sin(\theta) \end{aligned} \tag{2.39}$$

To measure CP asymmetries it is necessary to have one B decay to a CP eigenstate ($\Rightarrow A_{f_{CP}} = \eta_{f_{CP}} A_{\overline{f}_{CP}}$). It is also necessary for the other B to decay into a state that uniquely identifies its flavour ($\Rightarrow A_{f_{tag}} \neq 0, \overline{A}_{f_{tag}} = 0$ or vice versa). When this tag identifies the tagging B as a B^0 ($A_{f_{tag}} \neq 0, \overline{A}_{f_{tag}} = 0$) it can be shown [17] that equation 2.39, integrated over θ, then becomes:

$$\begin{aligned} R(t_{tag}, t_{CP}) =& Ce^{-(\Gamma/2+iM)(t_{tag}+t_{CP})}|\overline{A}_{tag}|^2|A_{f_{CP}}|^2 \\ & \times \{1 + |\lambda_{f_{CP}}|^2 + \cos(\Delta m_B \Delta t/2) \\ & - 2\sin(\Delta m_B \Delta t/2) Im(\lambda_{f_{CP}})\} \end{aligned} \tag{2.40}$$

where

$$\lambda_{f_{CP}} \equiv \frac{q}{p}\frac{\overline{A}_{f_{CP}}}{A_{f_{CP}}} = \eta_{f_{CP}}\frac{q}{p}\frac{\overline{A}_{\overline{f}_{CP}}}{A_{f_{CP}}} \tag{2.41}$$

,

$$\Delta t = t_{f_{CP}} - t_{f_{tag}} \tag{2.42}$$

and C is a normalisation factor. When the tagging B is identified as a $\overline{B}^0$, an identical expression to 2.40 applies, except that the signs of the sin and cos terms are reversed. If the approximation $|q/p| = 1$ holds, then the amplitudes for the two opposite tags are the same. Thus the difference of the two rates, divided by their sum,

$$a_{f_{CP}}(\Delta t) \equiv \frac{\Gamma(\overline{B}^0(\Delta t) \to f_{CP}) - \Gamma(B^0(\Delta t) \to f_{CP})}{\Gamma(\overline{B}^0(\Delta t) \to f_{CP}) + \Gamma(B^0(\Delta t) \to f_{CP})} \tag{2.43}$$

is

$$a_{f_{CP}} = \frac{(1 - |\lambda_{f_{CP}}|^2)\cos(\Delta m_B \Delta t) - 2Im\lambda_{f_{CP}}\sin(\Delta m_B \Delta t)}{1 + |\lambda_{f_{CP}}|^2} \tag{2.44}$$

In the case where $|\lambda_{f_{CP}}| = 1$[1] (see Section 2.3.3), this reduces to:

$$a_{f_{CP}} = Im\lambda_{f_{CP}}\sin(\Delta m_B \Delta t) \tag{2.45}$$

This provides a link between the experimentally observable $a_{f_{CP}}$ and the quantity $Im\lambda_{f_{CP}}$.

2.3 The Three Types of *CP* Violation in *B* Decays

There are three categories of *CP* violation expected to occur in *B* mesons:

1. *CP* violation in decay, when the amplitude for a decay and its *CP* conjugate have different magnitudes (*direct CP violation*).
2. *CP* violation in mixing, which may produce a measurable effect in semileptonic decays (*indirect CP violation*).
3. *CP* violation in the interference between decays with and without mixing, which can occur in decays into final states that are common to both B^0 and $\overline{B^0}$.

[1] $|\lambda_{f_{CP}}| \neq 1$ implies direct *CP* violation (see section 2.3.1). The Standard Model does not permit it in the decay $B^0 \to J/\psi K^0_S$ (see section 2.5.2).

2.3.1 *CP* Violation in Decay

If A_f and $\overline{A_f}$ are the decay amplitudes to the final state f from B and $\overline{B}$ respectively, $\left|\frac{\overline{A_{\overline{f}}}}{A_f}\right|$ is a quantity describing possible asymmetry in decay that is independent of phase conventions and physically meaningful. Two types of phases can appear in A_f and $\overline{A_{\overline{f}}}$, "weak" and "strong" . *CP* conjugation involves taking the complex conjugate of the amplitude. Hence any complex terms in Lagrangians will appear in complex conjugate form in the CP conjugate amplitude. The end result is that the phases will appear in A_f and $\overline{A_{\overline{f}}}$ with opposite signs. In the standard model, these come exclusively from the electroweak sector of the theory (via the CKM matrix), and are usually referred to as "weak phases". The weak phase of a single term is convention dependent, but the difference between two phases is an observable.

"Strong phases" can appear in amplitudes even when the Lagrangian has no imaginary part. They must appear in A_f and $\overline{A_{\overline{f}}}$ with equal sign, so do not violate *CP*. As before, only relative phases in different terms have physical meaning.

It is useful to write each contribution to A as the product of its magnitude A_i, its weak phase term $e^{i\phi_i}$ and its strong phase term $e^{i\delta_i}$. Then A_f can be written as:

$$A_f = \sum_i A_i e^{i(\delta_i + \phi_i)} \tag{2.46}$$

and the convention independent quantity is:

$$\left|\frac{\overline{A_{\overline{f}}}}{A_f}\right| = \left|\frac{\Sigma_i A_i e^{i(\delta_i - \phi_i)}}{\Sigma_i A_i e^{i(\delta_i + \phi_i)}}\right| \tag{2.47}$$

By inspection, if *CP* is conserved, all the ϕ_i must be equal. This leaves only an arbitrary phase which can be set to zero. Thus:

$$\left|\frac{\overline{A_{\overline{f}}}}{A_f}\right| \neq 1 \Rightarrow CP \text{ violation} \tag{2.48}$$

This is *CP violation in decay*, or *direct CP violation.* It arises from interference between the terms in the decay amplitude. An example would be from charged B decays,

$$a_f = \frac{\Gamma(B^+ \to f) - \Gamma(B^- \to \overline{f})}{\Gamma(B^+ \to f) + \Gamma(B^- \to \overline{f})} \tag{2.49}$$

CP violation in decay also occurs in neutral B meson decays, along with the two other types of CP violation described below. Final state interactions make direct CP violation hard to relate to CKM parameters.

2.3.2 *CP* Violation in Mixing

Comparing equation 2.19 with 2.8 and 2.7, the relations $\frac{p}{q} = M_{12} - i\Gamma_{12}/2$ and $\frac{q}{p} = M_{21} - i\Gamma_{21}/2$ can be extracted by eye. This leads to a second physically meaningful (and phase convention independent) quantity,

$$\left|\frac{q}{p}\right|^2 = \left|\frac{M_{12}^* - i\Gamma_{12}^*/2}{M_{12} - i\Gamma_{12}/2}\right| \tag{2.50}$$

which concerns the mixing of the B. If CP is conserved, the mass eigenstates must be CP eigenstates, and the relative phase between M_{12} and Γ_{12} disappears. Therefore

$$\left|\frac{q}{p}\right| \neq 1 \Rightarrow CP \text{ violation} \tag{2.51}$$

This is *CP violation in mixing,* or *indirect CP violation.* It arises because the mass eigenstates are different from the CP eigenstates. It could be measured in the B system using semileptonic decays:

$$a_{sl} = \frac{\Gamma(\overline{B^0}(t) \to l^+\nu X) - \Gamma(B^0(t) \to l^-\overline{\nu}X)}{\Gamma(\overline{B^0}(t) \to l^+\nu X) + \Gamma(B^0(t) \to l^-\overline{\nu}X)} \tag{2.52}$$

or in terms of $|q/p|$,

$$a_{sl} = \frac{1 - |q/p|^4}{1 + |q/p|^4} \tag{2.53}$$

(since $\langle l^- \overline{\nu} | \widehat{H} | B^0(t) \rangle = (q/p) g_-(t) \overline{A}$, $\langle l^+ \nu | \widehat{H} | \overline{B^0}(t) \rangle = (q/p) g_-(t) A$).

These asymmetries are expected to be small [11], $\mathcal{O}(10^{-2})$, and will be hard to relate to CKM parameters because of hadronic uncertainties.

2.3.3 *CP* Violation in the Interference Between Mixing and Decay

This third type of *CP* violation occurs only in B decays to final *CP* eigenstates (f_{CP}), to which both $B^0$and $\overline{B^0}$ can decay. The decay to the final eigenstate f_{CP} can then occur either as the direct decay $B^0 \to f_{CP}$ or with the B mixing before it decays, $B^0 \to \overline{B}^0 \to f_{CP}$ (+c.c. in both cases). The *CP* violating term then arises through interference between these two possibilities.

From section 2.3.2, *CP* conservation implies that $|q/p| = 1$ (no *CP* violation through mixing). Section 2.3.1 shows that *CP* conservation also requires that $|\overline{A}_{\overline{f}_{CP}} / A_{f_{CP}}| = 1$ (no direct *CP*). However, *CP* these two conditions are not sufficient. For *CP* to be conserved, it is also nesecary for the relative phase between (q/p) and $(\overline{A}_{\overline{f}_{CP}} / A_{f_{CP}})$ to vanish. From the definition of λ given in equation 2.41, this means that

$$\lambda \neq \pm 1 \Rightarrow CP \text{ violation} \tag{2.54}$$

$\lambda \neq \pm 1$ in both *CP violation in decay* and *CP violation in mixing,* because respectively $\left| \frac{\overline{A}_{\overline{f}}}{A_f} \right| \neq 1$ and $\left| \frac{q}{p} \right| \neq 1$ (i.e. $|\lambda| \neq \pm 1$). However, it is possible for *CP* violation to occur if $|\lambda| = \pm 1$, but $Im\lambda \neq 0$. This is known as *CP violation in the interference between mixing and decay.*

2.4 The Standard Model View of CP Violation

In this section, we examine the origins and consequences of CP violation in the Standard Model. For a more complete treatment of this subject, see [15, 16]

2.4.1 The CKM Matrix

In the weak basis, flavor changing charged current interactions have the form:

$$\mathcal{L}^{CC}_{quarks} = -\frac{g}{\sqrt{2}}(\overline{u'}_L, \overline{c'}_L, \overline{t'}_L)\gamma \begin{pmatrix} d'_L \\ s'_L \\ b'_L \end{pmatrix} W^{\dagger}_{\mu} + h.c. \tag{2.55}$$

where u', c', t', d', s', b' denote weak eigenstates. When this is written in terms of the mass eigenstates, it becomes:

$$\mathcal{L}^{CC}_{quarks} = -\frac{g}{\sqrt{2}}(\overline{u}_L, \overline{c}_L, \overline{t}_L)\gamma V_{CKM} \begin{pmatrix} d_L \\ s_L \\ b_L \end{pmatrix} W^{\dagger}_{\mu} + h.c. \tag{2.56}$$

V_{CKM}, the CKM (Cabibbo-Kobayashi-Maskawa) matrix embodies cross-generational mixing in the quark sector of the Standard Model. It is a unitary matrix in flavor space. Its components $V_{i,j}$ are the coupling constants of quarks i and j to the $W^{\pm}$. For n generations of quarks, it is an $n \times n$ complex matrix.

If there were two generations of quarks, the mixing matrix could be parameterized by three phases and one angle:

$$\begin{aligned} V &= \begin{pmatrix} \cos\theta_C e^{i\alpha} & \sin\theta_C e^{i\beta} \\ -\sin\theta_C e^{i\gamma} & \cos\theta_C e^{i(\beta+\gamma-\alpha)} \end{pmatrix} \\ &= \begin{pmatrix} e^{i\alpha} & 0 \\ 0 & e^{i\gamma} \end{pmatrix} \begin{pmatrix} \cos\theta_C & \sin\theta_C \\ -\sin\theta_C & \cos\theta_C \end{pmatrix} \begin{pmatrix} 1 & 0 \\ 0 & e^{i(\beta-\alpha)} \end{pmatrix} \end{aligned} \tag{2.57}$$

The phases have no physical significance, as they can be removed with a redefinition of the quark fields u_L, c_L, s_L relative to d_L, after which the matrix takes the standard Cabibbo [13] form:

$$V = \begin{pmatrix} \cos\theta_C & \sin\theta_C \\ -\sin\theta_C & \cos\theta_C \end{pmatrix} \tag{2.58}$$

However, with three quark generations, V is a 3×3 matrix:

$$V = \begin{pmatrix} V_{ud} & V_{us} & V_{ub} \\ V_{cd} & V_{cs} & V_{cb} \\ V_{td} & V_{ts} & V_{tb} \end{pmatrix} \tag{2.59}$$

and therefore has 18 real parameters. However, it is a unitary matrix, which imposes 9 constraints reducing the number of independent parameters to 9. Three of these can be represented as Euler angles, the other 6 are phases. Only one of these phases is physical, however, since the other 5 can be removed through a suitable redefinition of V. This leaves us with 4 parameters, 3 real angles and 1 complex phase. A standard way of parameterizing the CKM matrix to reflect this is

$$V = \begin{pmatrix} c_{12}c_{13} & s_{12}c_{13} & s_{13}e^{-i\delta} \\ -s_{12}c_{23} & c_{12}s_{23}s_{13}e^{i\delta} & s_{23}c_{13} \\ (s_{12}s_{13} - c_{12}c_{23}s_{13}e^{i\delta}) & (-c_{12}s_{23} - s_{12}c_{23}s_{13}e^{i\delta}) & c_{23}c_{13} \end{pmatrix} \tag{2.60}$$

where $c_{ij} \equiv \cos\theta_{ij}$ and $s_{ij} \equiv \sin\theta_{ij}$, with $\theta_{ij}(i \neq j)$ being the three mixing angles and δ is the complex phase.

It is this irremovable complex phase that is the source of CP violation. Consider the CP transformation laws:

$$\overline{\psi}_i\psi_j \rightarrow \overline{\psi}_j\psi_i \tag{2.61}$$

$$\overline{\psi}_i\gamma^\mu W_\mu(1-\gamma_5)\psi_j \rightarrow \overline{\psi}_j\gamma^\mu W_\mu(1-\gamma_5)\psi_i \tag{2.62}$$

it is apparent that the mass terms and gauge interactions must be CP invariant if all mass and coupling terms are real. In particular, the coupling of $W^\pm$ to quarks has the form

$$gV_{ij}\overline{u}_i\gamma_\mu W^{+\mu}(1-\gamma_5)d_j + gV^*_{ij}\overline{d}_j\gamma_\mu W^{-\mu}(1-\gamma_5)u_i \qquad (2.63)$$

which is invariant under a CP transformation only if all couplings and masses are real (or there is a mass basis and choice of phase convention where all couplings and masses are real). Therefore, δ cannot be 0 or π.

This complex phase is not in itself sufficient to imply CP violation. For that, the phase must be impossible to redefine away. For this to be true, all quark masses must be different and none of the three mixing angles can be 0 or $\pi/2$ [14].

2.4.2 The Jarlskog Invariant

$\theta_{ij} \neq 0, \pi/2$ and $\delta \neq 0, \pi$ are requirements of CP violation (see Section 2.4.1). A useful means of expressing these requirements was noticed by Jarlskog [19] - for any choice of i,j,k,l = 1,2,3

$$Im(V_{ij}V_{kl}V^*_{il}V^*_{kj}) = J\sum_{m,n=1}^{3}\epsilon_{ikm}\epsilon_{jln} \qquad (2.64)$$

and the above requirements are equivalent to $J \neq 0$.

This quantity J is phase convention independent (hence is known as the Jarlskog invariant), and is a measure of "how much" CP violation there is - all CP violating amplitudes are proportional to J in the Standard Model. Expressing J in terms of the CKM parameterization shown in equation 2.55,

$$J = c_{12}c_{23}c^2_{13}s_{12}s_{23}s_{13}\sin\delta \qquad (2.65)$$

which shows explicitly the requirements on δ and θ_{ij}.

2.4.3 The Wolfenstein Parameterization

A different, and useful approximate parameterization of the CKM matrix is due to Wolfenstein [18]. Its origins are in the observation that, empirically:

- Diagonal elements are ~ 1
- $|V_{12}| \simeq |V_{21}| \sim \lambda$
- $|V_{23}| \simeq |V_{32}| \sim \lambda^2$
- $|V_{13}| \simeq |V_{31}| \sim \lambda^3$

where $\lambda \equiv \sin\theta_c \simeq 0.221$

Its therefore useful to write an approximate version of V_{CKM} with terms that are expansions in λ.

$$V = \begin{pmatrix} 1-\frac{\lambda^2}{2} & \lambda & A\lambda^3(\rho - i\eta) \\ -\lambda & 1-\frac{\lambda^2}{2} & A\lambda^2 \\ A\lambda^3(1-\rho-i\eta) & -A\lambda^2 & 1 \end{pmatrix} + \mathcal{O}(\lambda^4) \tag{2.66}$$

In this representation:

- $\frac{|V_{ub}|}{|V_{cb}|} = \lambda\sqrt{\rho^2+\eta^2}$
- $\frac{|V_{td}|}{|V_{cb}|} = \lambda\sqrt{(1-\rho)^2+\eta^2}$
- $\frac{|V_{ts}|}{|V_{cb}|} = 1$

2.4.4 The Unitarity Triangle

The Unitarity of the CKM matrix implies a series of relationships between its elements. Three are very useful for describing the Standard Model's predictions for CP violation:

$$V_{ud}V_{us}^* + V_{cd}C_{cs}^* + V_{td}V_{ts}^* = 0 \tag{2.67}$$
$$V_{us}V_{ub}^* + V_{cs}C_{cb}^* + V_{ts}V_{tb}^* = 0 \tag{2.68}$$
$$V_{ud}V_{ub}^* + V_{cd}C_{cb}^* + V_{td}V_{tb}^* = 0 \tag{2.69}$$

Each of these can be conveniently represented as a triangle in the complex plane.

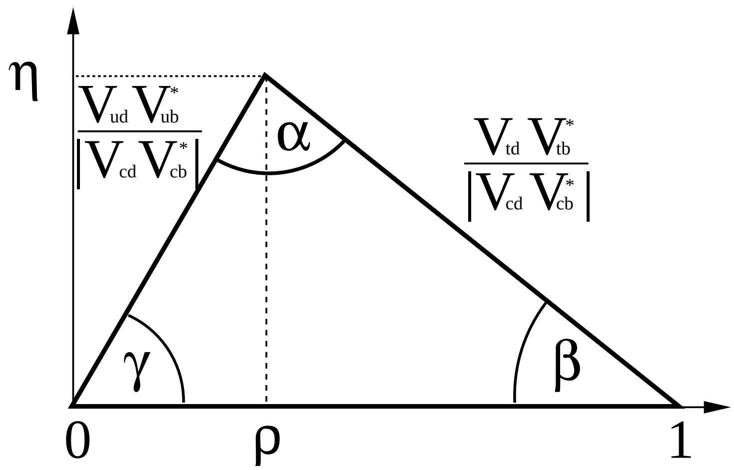

Figure 2.1: The Unitary Triangle

It can be seen that there are some important connections between the Jarlskog Invariant and the unitary triangles - the area of the triangles is $|J|/2$ (all triangles must therefore have the same area) and the sign of J gives the direction of the complex vectors.

Equation 2.69 relates specifically to the B sector, and so is the one of particular interest here. The convention is to divide through by $V_{cd}V_{cb}^*$ so that one side now lies between 0 and 1 on the real axis. This will be referred to from now on as *the* Unitary Triangle. The coordinates of the free vertex are labeled $(\rho\,\eta)$. It is shown in Figure 2.1.

The three angles are denoted α, β and γ where

$$\alpha \equiv \arg\left[-\frac{V_{td}V_{tb}^*}{V_{ud}V_{cb}^*}\right], \beta \equiv \arg\left[-\frac{V_{cd}V_{cb}^*}{V_{td}V_{tb}^*}\right], \gamma \equiv \arg\left[-\frac{V_{ud}V_{ub}^*}{V_{cd}V_{cb}^*}\right] \tag{2.70}$$

These angles are physical quantities and are measurable in CP asymmetries in B decays. In the Standard Model β is, to a good approximation, the phase between the neutral B mixing amplitude and its leading decay amplitudes.

2.5 *CP* violation in $B^0 \to J/\psi K_S^0$

This section examines the Standard Model predictions for the decay $B^0 \to J/\psi K_S^0$. It shows the relation between the experimentally observable quantity

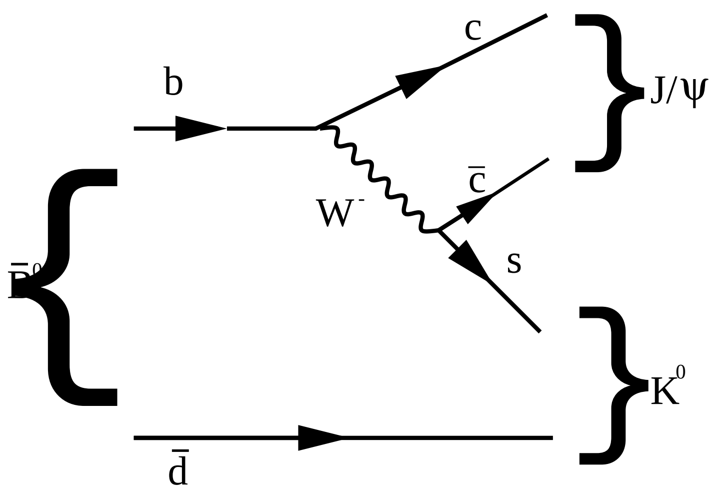

Figure 2.2: Leading Tree diagram for $\overline{B}^0 \to J/\psi K^0$

$a_{f_{J/\psi K^0_S}}$ and the Unitary Triangle parameter β.

2.5.1 The Decay $B^0 \to J/\psi K^0$

The tree and leading level penguin diagrams for this decay are shown in Figures 2.2 and 2.3.

As can be seen from the diagrams, the quark bound to the b has no role in the decay and is just a passive observer, hence these are known as spectator processes. For the tree process, the basic interaction Hamiltonian for Charmonium final states is:

$$H_{Weak} = \frac{G_f}{\sqrt{2}} V_{cb} V^*_{cs} (\overline{s}c)(\overline{c}b) \tag{2.71}$$

Where the terms $(\overline{s}c)$ and $(\overline{c}b)$ represent the vertex interactions ($\overline{s}$ here being the annihilation of an $\overline{s}$ quark or the creation of an s, *etc*). Penguin diagrams also contribute (although they are expected to be small, see [20]) and lead to an additional term in the interaction Hamiltonian:

$$H_{Effective} = \frac{G_F}{\sqrt{2}} V_{cb} V^*_{cs} \left[c_1(\mu)(\overline{s}c)(\overline{c}b) + c_2(\mu)(\overline{c}c)(\overline{s}b) \right] \tag{2.72}$$

Where $c_1(\mu)$ and $c_2(\mu)$ account for gluon interactions, and can in principle be accounted for from QCD.

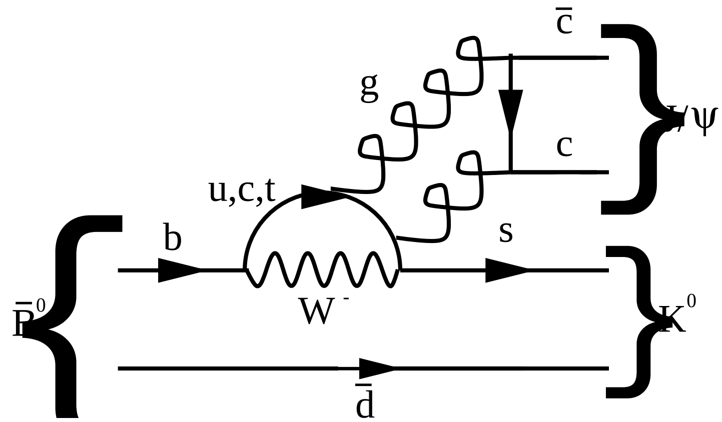

Figure 2.3: Leading Penguin Diagram for $\overline{B}^0 \to J/\psi K^0$

There is one important point to note here - although the contribution of the Penguin diagram must be considered, for the leading diagram its phase is $V_{cb}V_{cs}^*$, just as for the tree diagram.

2.5.2 *CP* Asymmetry in $B^0 \to J/\psi K^0_S$

As mentioned in section 2.5.1, the decay $B^0 \to J/\psi K^0$ involves only a single phase (to a very good approximation). This makes it very unlikely to exhibit direct *CP* violation (detailed estimates show the level of uncertainty to be of order 10^{-3} [20]). It can also be seen from section 2.5.1 that

$$\frac{\overline{A}(J/\psi K^0)}{A(J/\psi K^0)} = \frac{V_{cb}V_{cs}^*}{V_{cb}^*V_{cs}} \tag{2.73}$$

Returning to q/p (from equations 2.24 and 2.25), in the Standard Model, it is possible to calculate the ratio Γ_{12}/M_{12}, and it is found to be $\sim 10^{-2}$ [21]. Thus equation 2.42 becomes

$$\frac{q}{p} \simeq \sqrt{\frac{M_{12}^*}{M_{12}}} = \frac{V_{tb}^*V_{td}}{V_{tb}V_{td}^*} \tag{2.74}$$

which also implies $|q/p| \simeq 1$.

So far we have only considered $B^0 \rightarrow J/\psi K^0$ - the actual decay is $B^0 \rightarrow J/\psi K^0_S$, for which it is necessary to include the phase from the $K^0 - \overline{K}^0$ mixing amplitude,

$$\left(\frac{q}{p}\right)_K = \frac{V_{cs}V_{cd}^*}{V_{cs}^*V_{cd}} \tag{2.75}$$

Thus from the definition of λ in equation 2.59,

$$\begin{aligned}
\lambda_{J/\psi K^0_S} &\simeq \frac{V_{cb}V_{cs}^*}{V_{cb}^*V_{cs}} \cdot \frac{V_{tb}^*V_{td}}{V_{tb}V_{td}^*} \cdot \frac{V_{cs}V_{cd}^*}{V_{cs}^*V_{cd}} && (2.76)\\
&= \frac{V_{cb}}{V_{cb}^*} \cdot \frac{V_{tb}^*V_{td}}{V_{tb}V_{td}^*} \cdot \frac{V_{cd}^*}{V_{cd}} && (2.77)\\
&= \left(\frac{V_{cd}V_{cb}^*}{V_{tb}^*V_{td}}\right)^* \cdot \left(\frac{V_{cd}V_{cb}^*}{V_{tb}^*V_{td}}\right)^{-1} && (2.78)\\
&= \frac{\left|\left(\frac{V_{cd}V_{cb}^*}{V_{tb}^*V_{td}}\right)\right|}{\left|\left(\frac{V_{cd}V_{cb}^*}{V_{tb}^*V_{td}}\right)\right|} e^{-2i\arg\left(\frac{V_{cd}V_{cb}^*}{V_{tb}^*V_{td}}\right)} && (2.79)\\
&= -e^{-2i\beta} && (2.80)
\end{aligned}$$

Where β is the angle of the unitary triangle defined in equation 2.71. Hence

$$Im\lambda_{J/\psi K^0_S} = \sin 2\beta \tag{2.81}$$

(given the approximations stated in the text). Combined with equation 2.45, this implies:

$$a_{f_{J/\psi K^0_S}}(\Delta t) = \sin 2\beta \sin(\Delta m_B \Delta t) \tag{2.82}$$

Thus a measurement of the decay rate difference (between tagging B is $B^0, \overline{B}^0$) to the final state $B^0 \rightarrow J/\psi K^0_S$ is a direct measurement of $\sin 2\beta$. In this thesis, a measurement of $\sin 2\beta$ is made using $a_{f_{J/\psi K^0_S}}$.

2.6 Factorization in $B^0 \to J/\psi K_S^0$

In addition to the CP measurement, it is possible to use $B^0 \to J/\psi K_S^0$ decays to test the factorization hypothesis [4, 5]. The $\overline{s}$ and d (or c.c.) quarks in the decay can form one or more mesons, in a process known as hadronisation. This thesis is interested only in the occasions when they join together to form a K^0 (or $\overline{K}^0$). The factorization hypothesis states that the Hamiltonian can be separated into two parts, i.e.

$$\left\langle \overline{c}c + \overline{s}d | T | \overline{b}d \right\rangle \propto \langle \overline{c}c | J^{\mu} | 0 \rangle \langle \overline{s}d | J_{\mu} | B \rangle \tag{2.83}$$

where the first term on the right hand side is governed by the decay constant $f_{J/\psi}$ and the second term is governed by the hadronic from factors for $B \to K$ transitions [8].

Factorization makes the assumption that the process can be divided up into two groups of quarks that do not interact with each other. This is not necessarily valid for all decays. The factorization approach has been seen to work extremely well in semileptonic B decays, where $W^{\pm} \to l^{\pm}\nu$, because the lepton cannot interact via gluons with the other particles. For factorization to be valid in the decay $B^0 \to J/\psi K^0$ it is necessary to assume that the $c\overline{c}$ pair moves away from the interaction region quickly enough to ignore gluon interactions between the two groups of quarks.

Using the Branching Fraction measurement made in this thesis, it is possible to test the predictions made by the Factorization hypothesis, and determine to what extent it is valid in B decays in general.

Chapter 3

The Detector

3.1 e^+e^- *B* Factories

The design of an experiment to study *CP* violation physics in the *B* sector presents some extreme challenges to the accelerator. A vast amount of integrated luminosity is required. Sizeable datasets from branching fractions $\sim 10^{-4}$ are needed for measurements of sin2β. The obvious requirement for studying *B* physics is to produce B_d mesons with the minimum production of background (non *B*) events. The $\Upsilon(4S)$ resonance is just above the energy needed for pair production of B_d, and effectively all its decays are to $B^0\overline{B}^0$ or B^+B^-[12]. Hence running at the $\Upsilon(4S)$ means high signal to background, no fragmentation products and clean events with reduced combinatorial backgrounds. It also allows exact kinematic constraints to be placed on reconstructed *B*s.

Many of the *CP* violating effects in the *B* system are time dependent, and indeed integrate over time to zero. Very accurate decay time measurements are needed. These can be done by using an asymmetric collider, so that the centre of mass is rapidly moving with respect to the lab frame. Decay time can then be inferred from displaced vertices.

B physics also makes great demands of a detector. If decay times are to be measured from displaced vertices, the vertex position must be known to an extraordinary precision. Since the accelerator is asymmetric, the detector as a whole must be built asymmetrically to provide the best acceptance. If it is to cope with the high luminosity delivered by the accelerator, it must be able to withstand high levels of radiation, be able to operate under high background conditions, and be able to control, process and store the torrents of information. And on top of this, it must also reconstruct charged particles down to low momenta with high efficiency and good momentum resolution, reconstruct photons with good resolution of energy and angle, and accurately and efficiently identify particle type.

Two such experiments - B factories - exist, BaBar at SLAC and Belle at KEK. This chapter describes the form and performance of the equipment that BaBar uses to accomplish its goals. A complete description of the BaBar experiment in the year 2000 can be found in [28]. This has been used as the source of the technical detail quoted in this chapter.

The co-ordinate system used in this chapter and throughout the rest of this thesis is defined as:

- The z axis follows[1] the direction of the beam (+ve in the direction of the high energy beam).
- The y axis points directly upward
- The x axis points radially out from the centre of the PEP-II ring.
- θ and ϕ are the polar and azimuthal angles, with $\theta = 0$ defined as the direction of the high energy beam.

3.2 The PEP-II Asymmetric Collider and the SLAC linac

3.2.1 Function of PEP-II

The PEP-II B Factory is an e^+e^- colliding beam storage ring complex designed to produce a luminosity greater than $3 \times 10^{33} cm^{-2} s^{-1}$. It operates at a centre of mass energy of 10.58 GeV, the mass of the $\Upsilon(4S)$ resonance. The machine is asymmetric, colliding a 9.0 GeV electron beam with a 3.1

[1]The axis is actually offset by $20 mrad$.

GeV positron beam, corresponding to a boost of $\beta\,\gamma = 0.56$[1] to the centre of mass relative to the lab frame.

3.2.2 Description of PEP-II

The electrons and positrons are provided by the two mile long SLAC Linac and fed into the $400m$ radius PEP II ring. The asymmetry of the beams makes two storage rings necessary. The electrons travel in the High Energy Ring (HER), and the positrons in the Low Energy Ring (LER). The beams collided at one point only, head on.

The high intensity of the Linac makes it optimal to re-charge the beams in "top off" mode. Roughly every forty minutes, when the current in the rings has dropped off and the luminosity is below 90% of its peak value, the running of the detector is suspended for a few minutes while the Linac injects into PEP-II. This keeps the data free from accelerator noise and keeps the luminosity close to peak at all times. The beams are never dumped during normal operation, and take 10-15 minutes to recover from a complete loss.

3.2.3 Performance of PEP-II

Some of the relevant design parameters for PEP II are shown in table 3.1 along with typical values during the period in which data was taken. High integrated luminosity was achieved through reliability and the ability to maintain stable beams. In 2000 PEP II reached a luminosity of $3.1 \times 10^{33} cm^{-2} s^{-1}$ and in 2001 it has reached $4.2 \times 10^{33} cm^{-2} s^{-1}$.

3.3 The Silicon Vertex Tracker (SVT)

3.3.1 Function of the SVT

To study time dependent effects, *BABAR* must be able to measure decay vertices with very great accuracy: the SVT provides that capability. It also provides stand-alone tracking for low p_t particles ($p_t < 120 MeV$) and is

[1] β is the velocity p/E and $\gamma = \sqrt{(1-\beta^2)}$

Parameters	Design	Typical
Energy HER/LER (GeV)	9.0/3.1	9.0/3.1
Current HER/LER (A)	0.75/2.15	0.7/1.3
Number of bunches	1658	553-829
Bunch spacing (ns)	4.2	6.3-10.5
$\sigma_{L_x}(\mu m)$	110	120
$\sigma_{L_y}(\mu m)$	3.3	5.6
$\sigma_{L_z}(\mu m)$	9	9
Luminosity ($10^{33} cm^{-2} s^{-1}$)	3	2.5
Luminosity (pb^{-1}/day)	135	120

Table 3.1: PEP-II storage ring parameters

the first level of charged particle tracking in general. It was designed to be of low mass, to minimize multiple scattering, and radiation hard , as beam background hits it harder than any other part of the detector. dE/dx measured in the detector is also used in PID.

3.3.2 Description of the SVT

The structure of the SVT is show schematically in Fig 3.1 and Fig 3.2a . The SVT is constructed from 52 modules, organized in five radial layers. The three inner layers are crucial for maximising vertex and tracking resolution. The outer two layers are needed for tracking of low p_t particles that don't reach the drift chamber. The arching structure of the two outer layers is intended to maximize solid angle coverage whilst minimizing scattering. The SVT is built asymmetrically to maximize angular coverage in the center of mass - acceptance in polar angle theta is $-0.87rad < \theta_{lab} < 0.96rad$ ($-0.95rad < \theta_{CM} < 0.87rad$). Radiation exposure is monitored by a system of 12 PIN diodes placed close to the first silicone layer.

3.3.3 Performance of the SVT

The average hit reconstruction efficiency of the SVT is above 98%. Good hit resolution was achieved through an accurate alignment procedure. The hit

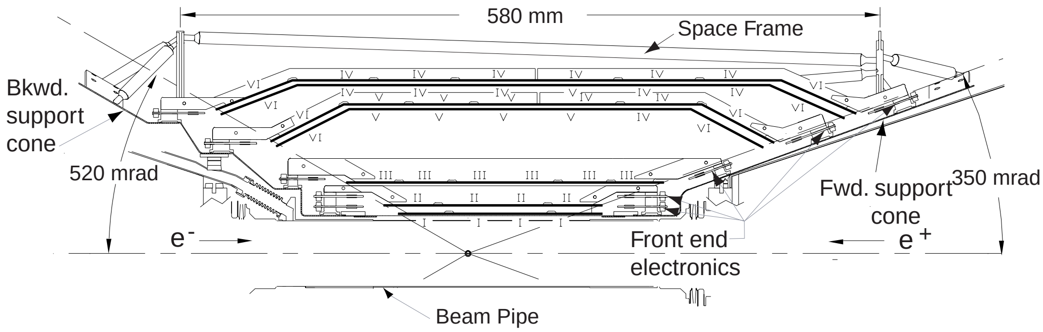

Figure 3.1: Side view of SVT

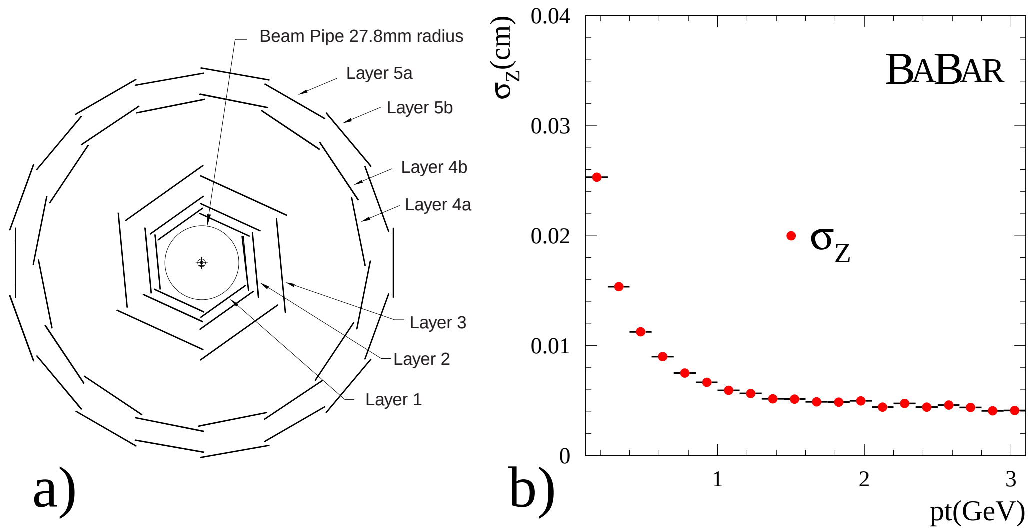

Figure 3.2: a)End view of SVT, b) SVT resolution in z

resolution in the z co-ordinate[1] is shown in Fig 3.2b . Two track vertices, such as J/ψ to $l^+l^-$are reconstructed with a typical resolution of 70 microns in z.

3.4 The Drift Chamber (DCH)

3.4.1 Function of the DCH

The drift chamber is BaBar's main tracking device. It enables tracks to be reconstructed in 3 dimensions and measures a charged particle's transverse momentum from the curvature of its track in the 1.5T magnetic field. The dE/dx of the tracks is measured by deducing the deposited energy from the pulse heights in cells. The drift chamber also provides a basic component of the Level 1 trigger (Section 3.8).

3.4.2 Description of the DCH

Physically, the DCH is a 280 cm long cylinder, with an inner radius of 23.6cm and an outer radius of 80.9 cm. The chamber is mounted asymmetrically about the interaction point to accommodate the boost. It has a number of features to minimize the material in front of the Calorimeter - the beryllium inner wall (0.28 radiation lengths), the thin outer half of the forward end-plate (15mm aluminium), and the carbon-fiber outer cylinder (see Fig 3.3).

Internally, the DCH consists of 7104 hexagonal cells, approximately 1.8cm wide by 1.2cm high, arranged in 40 concentric layers between a radius of 25.3 and 79.0 cm (Figs 3.3 and 3.4). This provides charged particle tracking between $-0.92rad < cos\theta_{lab} < 0.96rad$, where theta is the polar angle. The forty layers are subdivided into ten "superlayers" of four layers each. In each superlayer, the sense and field wires are organized with the same orientation. The DCH is aranged with two stereo superlayers between each axial superlayer.

Each of the hexagonal cells consists of a 20 micron rhenium-tungsten

[1] The resolution in z is of particular interest because it is the limiting factor in the resolution of vertex displacement, and therefore of Δt (see CP chapter).

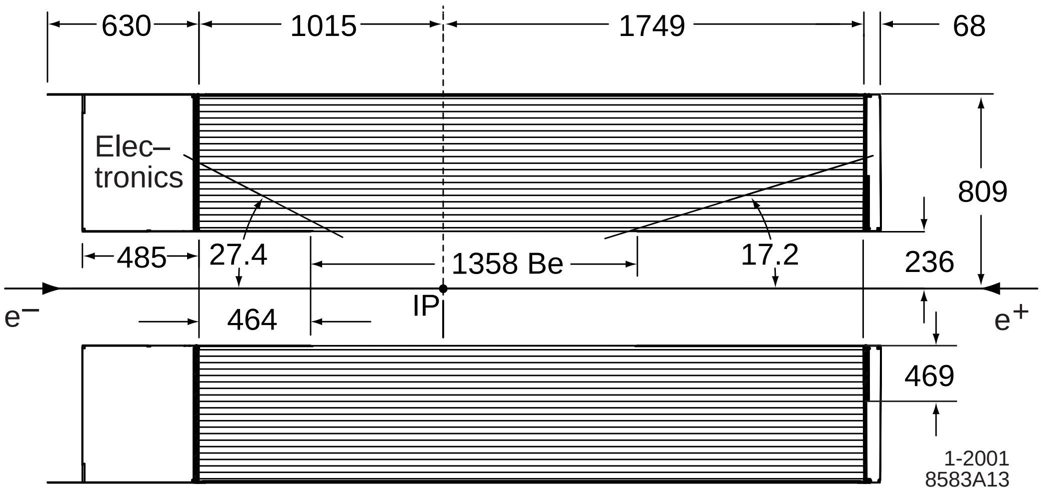

Figure 3.3: DCH side view

sense wire operating nominally in the range 1900-1960 V, surrounded by 6 cathode wires, approximately half of which are shared with neighboring cells. Multiple scattering is reduced by the low mass gas (4/1 He/isobutane) and by keeping the material within the detector fiducial volume at a minimum.

3.4.3 Performance of the DCH

Typically, σ_{p_t}/p_t=0.47%, and $\sigma_{dE/dx}/(dE/dx)$=7.5%. Fig 3.5b shows the drift chamber efficiency as a function of p_t and Fig 3.5a shows the effectiveness of dE/dx for particle identification.

3.5 The DIRC (Direct Internally Reflection Cherenkov)

3.5.1 Function of the DIRC

The DIRC is devoted to particle identification. It is vital for $K^{\pm}/\pi^{\pm}$ separation, both in event selection (although not in the main analysis described in this thesis) and in identifying kaons to be used for B flavour tagging.

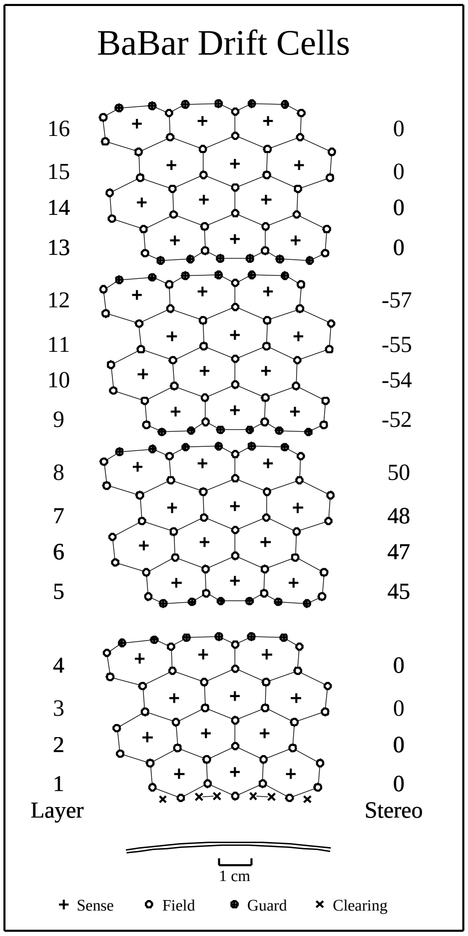

Figure 3.4: DCH cell structure

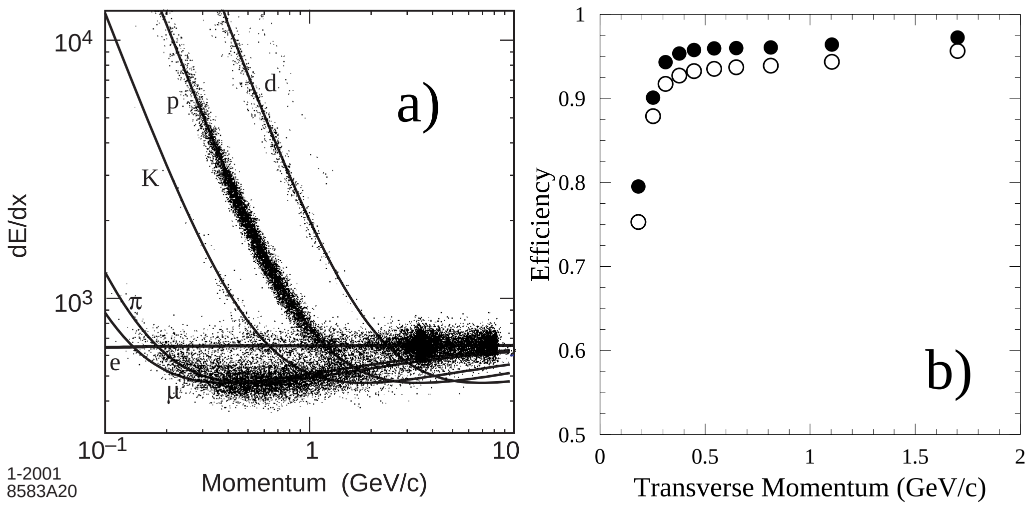

Figure 3.5: a) dE/dx vs Momentum in DCH, b) DCH efficiency vs P_t with the drift chamber at 1960V (dot) and 1900V (circle)

3.5.2 Description of the DIRC

Surrounding the DCH is an array of 144 fused silica quartz bars, each approximately 17mm thick, 35 mm wide and 4.9m long (see Fig 3.6). Bars are joined together end to end in groups of 3. Particles above the Cherenkov threshold radiate photons in the quartz. The angles of the photons with respect to the particle that emitted them are measured with an array of 10,752 photomultiplier tubes located in a low magnetic field volume outside the return yoke of *BABAR* . The polar angle coverage is $-0.84rad < cos\theta_{lab} < 0.90rad$.

The 144 quartz bars are arranged in 12 “barboxes” that penetrate through the magnetic end-plug of BaBar. Cherenkov photons travel down the length of the bar and exit through a wedge and a quartz window into a water tank that optically couples the quartz bars to the photo-multiplier array.

The Cherenkov angle can be deduced from the direction of the charged particle and the location of the photo-multiplier. Spurious hits from beam induced backgrounds can be effectively excluded because a single charged particle is projected as a circle onto the photomultiplier “wall”.

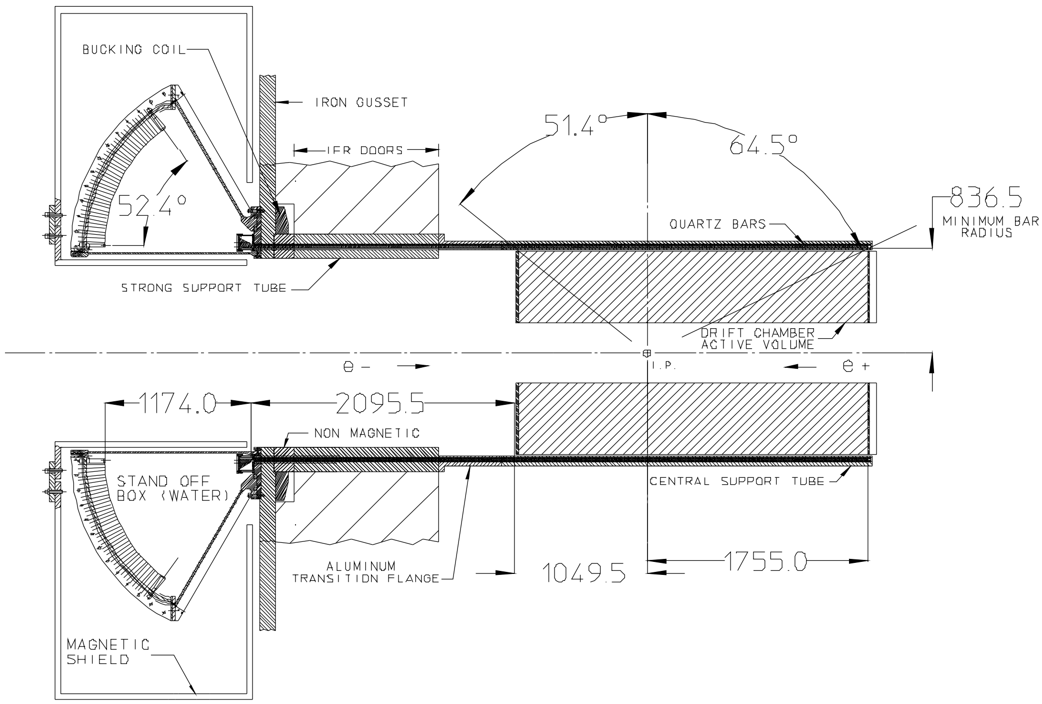

Figure 3.6: Side view of DIRC

3.5.3 Performance of the DIRC

The angular resolution for a single photon is about $10.2mr$ and there are an average of 30 photons per track. This gives a "per track" resolution of $2.8mr$. At $3GeV$, Kaons and Pions can be resolved to approximately 3σ. Fig 3.7 shows efficiency and miss-ID for Kaons identified in the DIRC.

3.6 Electromagnetic Calorimeter (EMC)

3.6.1 Function of the EMC

The EMC is designed to accurately measure the energy deposited in it by particles as they pass through. As such it is able to detect photons, which leave no other trace in the detector. K_L detection and identification also makes use of the EMC. Deposited energy asociated with charged tracks can be used for particle identifiaction, discriminating between electrons, pions and muons. Additionally, the EMC serves as a component in the level 1

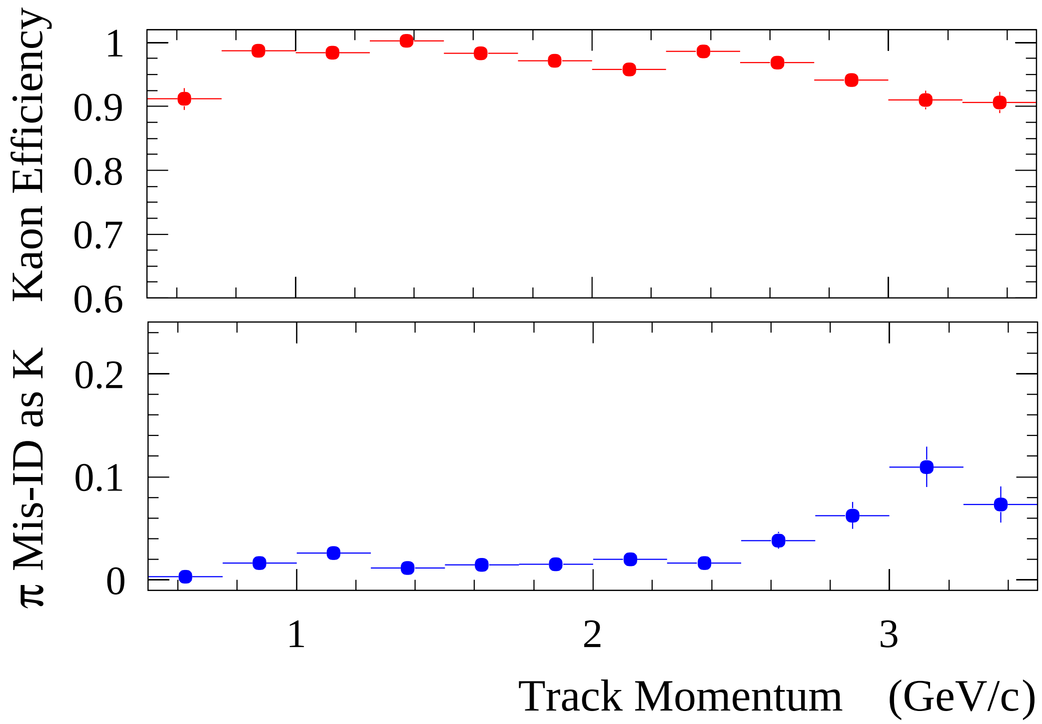

Figure 3.7: Efficiency and Miss-ID for Kaons

trigger (Section 3.8).

3.6.2 Description of the EMC

The EMC contains 6580 CsI crystals doped with thallium ($\sim$ 1000 ppm). Each crystal is a truncated trapezoidal pyramid, 16 - 17.5 radiation lengths long. The front faces are about 5cm by 5cm. In the EMC barrel, the crystals are arranged quasi-projectively, in 48 polar rows by 120 azimuthal rows. There is also an endcap section, in the forward direction only, in which there are eight rows of crystals. The coverage of the EMC is $-0.78rad < cos\theta_{lab} < 0.96rad$, (see Fig 3.8).

Each crystal is wrapped with a diffuse reflective material and housed in a thin carbon fiber composite mechanical structure. There are 280 such modules in the barrel, and 20 in the endcap. Crystals are read out with two independent $2cm^2$ large area PIN photo diodes attached to their rear faces.

Many different methods are combined for calibration and monitoring.

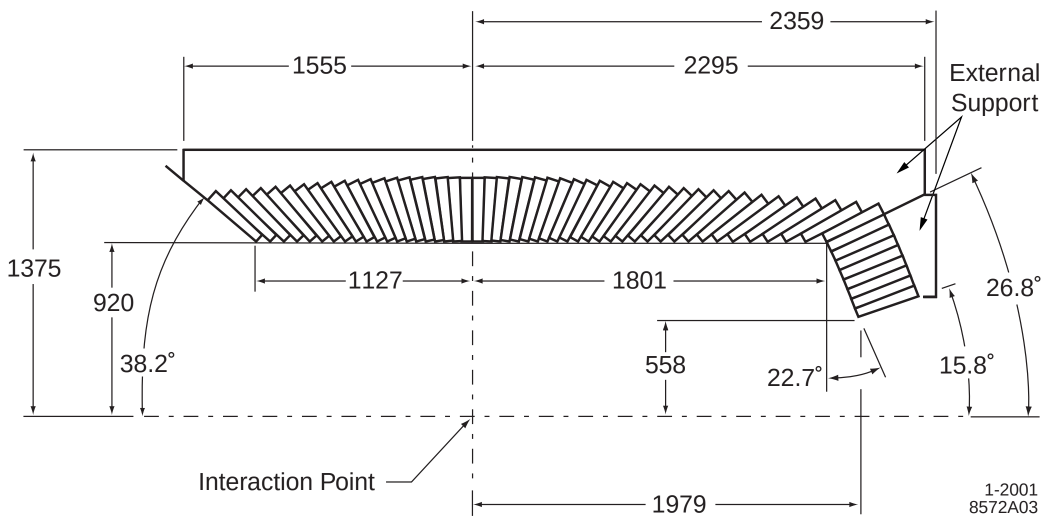

Figure 3.8: Geometry of the EMC

Charge injection into the front end of the amplifiers, a fibre-optic/xenon light pulser system injecting light into the rear of the crystal, and a circulating radioactive source at the front face of the crystal are all used. Signals from data (π^0, radiative and non radiative Bhabhas, $\gamma\gamma$ and $\mu^+\mu^-$ events) provide additional calibration points. Source and Bhabha calibrations are updated weekly to track the small changes in light yield with integrated radiation dose. Light pulser runs are carried out daily to monitor relative changes at the $< 0.15\%$ level.

3.6.3 Performance of the EMC

The efficiency of the EMC is $> 96\%$ for detection of photons with $E > 20MeV$. The lost photons are almost exclusively due to conversions in the material before the EMC. The resolution should follow the dependence $\frac{\sigma_E}{E} = \frac{x}{\sqrt[4]{E(GeV)}} \oplus y$. Measurements with $\pi^0, \eta, \chi_{c1} \rightarrow J/\psi\gamma$ and Bhabhas give values of $x = 2.32 \pm 0.30\%$ and $y = 1.85 \pm .12\%$. See Fig 3.9a.

The positional resolution can also be measured from π^0 and η decays. Typically, it was found to be $3.9mr$ in both θ and ϕ (see Fig 3.9b). This is comparable to the size of a single crystal.

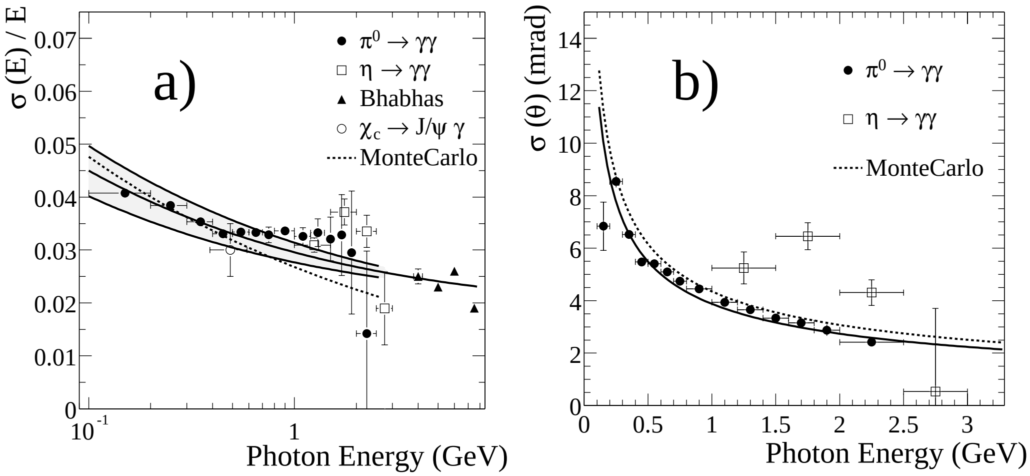

Figure 3.9: a) $\sigma(E)/E$ in Monte Carlo compared to the best fit to what is observed from data (from π^0, η, χ_c and Bhabhas), b) $\sigma(\theta)$ in Monte Carlo and from Data (π^0 and η)

3.7 Instrumented Flux Return (IFR)

3.7.1 Function of the IFR

The IFR is used to identify muons and neutral hadrons. It was designed to have a large solid angle coverage, good efficiency and the ability to identify even low momentum muons ($p < 1GeV/c$).

3.7.2 Description of the IFR

The flux return for the 1.5 T solenoidal magnet has been instrumented with nearly 900 Resistive Plate Chambers (RPCs). They are interleaved with the iron plates that make up the yoke. There are 19 RPC layers in the barrel region and 18 layers in the forward and backward end-caps. Between these layers are iron plates of varying widths. The iron plate thickness is graded from 2cm for plates closest to the interaction region to 10cm for the outermost layers for a total depth of iron of ≥65cm in the barrel and ≥60cm in the end caps (see Fig. 3.10). This arrangement is intended to improve performance for low momentum muons.

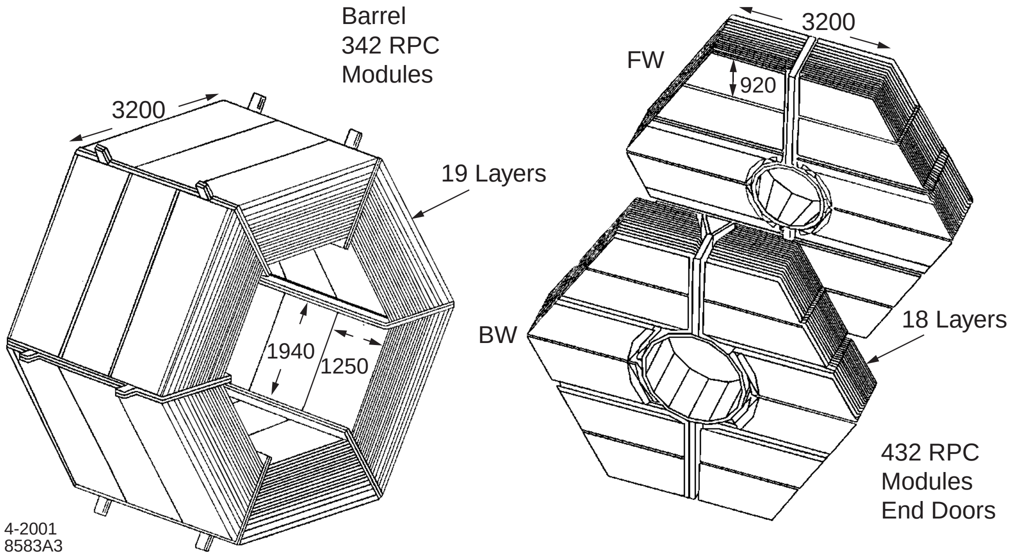

Figure 3.10: The IFR: Barrel (left) and Forward and backward end-caps (right)

An additional two layer RPC is located between the EMC and the solenoid cryostat. It is intended to provide information on particles with too little momentum to penetrate the first layer of iron in the yoke.

The IFR (barrel and end-caps) provides a coverage of $0.3rad < \theta_{lab} < -0.4rad$.

3.7.3 Performance of the IFR

In terms of the analysis presented in this thesis, the important aspect of the IFR's performance is its use in muon PID. Figure 3.11 shows the efficiency and pion miss-ID of a typical muon ID selection. Efficiency is above 80% for $p > 1\ GeV/c$, and $6 - 8\%$ of pions are incorrectly identified as muons ($\sim 2\%$ of these are actually due to pion decay).

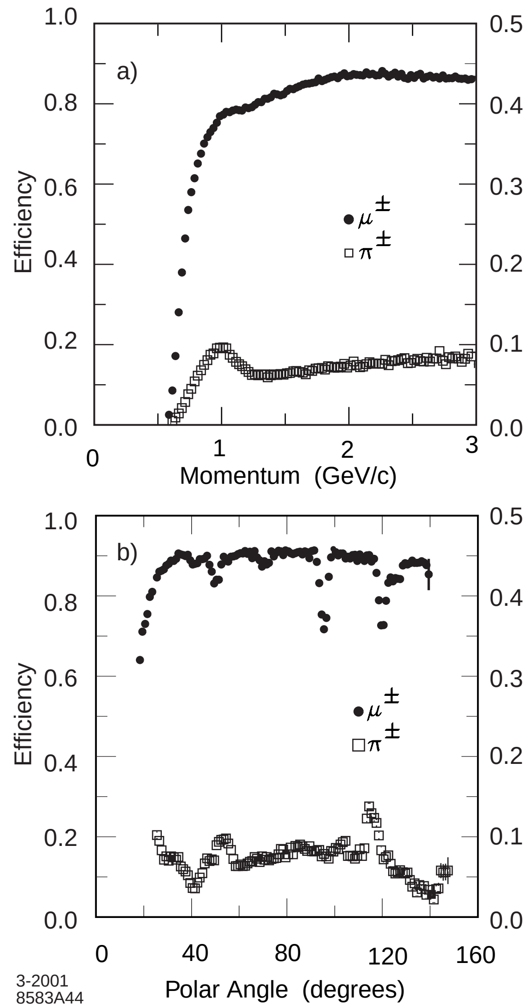

Figure 3.11: Muon efficiency (left scale) and pion mis-ID (right scale) as a function of momentum (top) and polar angle ($1.5 < p < 3.0\ GeV/c$) (bottom), loose selection criteria.

3.8 Level 1 Trigger

3.8.1 Function of the L1T

The L1T serves to reduce the amount of events that the Level 3 Trigger (see 3.10) has to deal with. It performs a fast and efficient selection based on limited information to exclude events that are very unlikely to contain interesting physics.

3.8.2 Description of the L1T

The L1T descisions are made purely in hardware. It is made up of the drift chamber trigger (DCT), the calorimeter trigger (EMT), the IFR trigger (IFT) and the global trigger (GLT). The DCT identifies short and long tracks, and hight p_t tracks. The loosest criteria is for short tracks, which are accepted down to 120 MeV/c if they reach superlayer five in the drift chamber. Long tracks, which reach the outer layer of the DCH are required to have $p_t > 180MeV/c$. The EMT identifies deposits in the calorimeter passing various energy thresholds, the lowest being 100 MeV (for use in minimum ionising particle identification). All high energy ($> 700MeV$) deposits in the calorimieter are also noted. The IFT is used to trigger on $\mu^+\mu^-$ and cosmic ray events, for diagnostic purposes, and does not contribute to normal data taking.

The GLT combines information from the DCT and the EMT and makes the pass/fail decision. As well as triggers designed to pass specific processes ([28] gives the full list) there are two general physics selections: $\geq$ 3 short tracks, $\geq$ 2 long tracks and $\geq$ 2 deposits of more than $100MeV$ in the calorimeter, or $\geq$ 1 deposit of more than $800MeV$ in the calorimeter plus $\geq$ 2 short tracks, $\geq$ 1 long track. It operates in continuous sampling mode, processing input data and generating output trigger information at fixed time intervals.

3.8.3 Performance of L1T

The L1T system is designed to be able to trigger independently from pure DCT or EMT triggers with high efficiency for most physics sources. $B^0\overline{B^0}$ events are triggered at $> 99\%$ efficiency from either one alone, and 99.9% efficiency from the two combined. Tau and two photon events do not have a fully efficient pure EMT trigger and rely mainly on DCT triggers.

For a typical run, the level 1 trigger operates at 700 Hz. It has the capacity to operate at significantly more than 2kHz, hence there is no significant dead time.

For a rate of 700Hz at design luminosity, Bhabha events and other e^+e^- interactions contribute about 120 Hz. Cosmic rays account for 130 Hz. The dominant source of background causing the remaining non physics triggers is the interaction of lost particles with the beam line components. For typical beam currents, the high energy beam is the source of three times as much background as the low energy beam.

To extract the perfomrance of the L1T, random and cyclic triggers are used at low rates.

3.9 Level 2 Trigger

There is no level 2 trigger. It will be introduced to cope with higher luminosity running as *BABAR* evolves.

3.10 Level 3 Trigger (L3T)

3.10.1 Function of the L3T

The level 3 trigger is the first system able to “see” events as a whole. It performs a more sophisticated selection based on the characteristics of the event to reduce the processing and storage load downstream.

3.10.2 Description of L3T

The L3T processes data from from the drift chamber and the calorimeter using two independent algorithms to form track and cluster objects from each respectively. The Level 3 Drift chamber algorithm uses lookup tables to perform fast track finding and 3-D track fitting, and is efficient for tracks with $p_t > 250MeV/c$. The level 3 calorimeter algorithm also uses a lookup table method, in this case to form clusters from crystal data. To reduce noise, the crystals with less than 30 MeV are excluded. The cluster objects formed are accepted if energy $> 100MeV$.

The Level 3 logging decision is based on general event shapes, rather than on the identification of individual processes. An exception is made for Bhabha events, which have to be vetoed to reduce their rate. ($\sim 100Hz$ at design luminosity). The physics trigger is an OR of two independent filters. The track filter requires either one track with $p_t > 800MeV/c$ coming from the interaction point, or two tracks with $p_t > 250MeV/c$ and looser vertex cuts. The cluster filter accepts events with large numbers of clusters (> 4) or with a large energy deposits (2 clusters with $E_{CM} > 350MeV$) in the Electromagnetic Calorimeter. In both cases, a high effective mass, calculated from the clusters, is required ($> 1.5GeV$).

Both filters are subject to a veto algorithm that identifies Bhabha events based on clean signatures in the Drift Chamber and the Calorimeter. The veto has no impact on hadronic events, and only has noticeable effect on very few types of events like $\tau^+\tau^- \to e^+\nu\overline{\nu}\ e^-\nu\overline{\nu}$.

In addition to the "physics" events that pass the L3T in the conventional way, various other events are passed to form samples for calibration and monitoring. A prescaled sample of Bhabha events, flattened in θ, is preserved for calibration purposes. In addition, other events such as radiative Bhabha events, cosmics, and random triggers are allowed to pass. 0.01% of all L1T events are allowed to pass in order to extract the L3T acceptance for different physics processes.

3.10.3 Performance of L3T

The typical logging rate at design luminosity is $\sim 90Hz$. The efficiency of the track filter for $B\overline{B}$ events is 99%, while the efficiency of the cluster filter is 94%.

3.11 Data and Monte Carlo Samples

3.11.1 Data Sample

Two slightly different data sets were used for the two analysis results presented here. For the branching fraction measurement, $20.7fb^{-1}$ of data taken at the $\Upsilon(4S)$ was used, corresponding to $(22.7 \pm 0.4) \times 10^6$ $B\overline{B}$ pairs. This is referred to as "Run 1". The most significant change in the detector during this time was in the drift chamber - its voltage was raised from $1900V$ to $1960V$, with $11.2fb^{-1}$ of data taken at $1900V$, and $9.4fb^{-1}$ at $1960V$.

For the measurement of sin2β, the $20.7fb^{-1}$ of "Run 1" data plus $8.4fb^{-1}$ of "Run 2" data was used, a total of around 32 million $B\overline{B}$ pairs. This additional data was not used for the branching fraction measurement because studies into track reconstruction and PID efficiencies had not been carried out at the time of writing. However, vertex resolution and tagging efficiency had been closely studied, allowing this data to be used for the sin2β measurement.

3.11.2 Monte Carlo Samples

A GEANT3 based Monte Carlo simulation was used to provide all the simulated data used in this analysis. A large quantity of Generic Monte Carlo was generated by the *BABAR* collaboration, $B\overline{B}$, $c\overline{c}$ and uds. This was used for background studies. The most significant single source of background was found to come from $B \to J/\psi + X(J/\psi \to ll)$ events. A large sample of these events was generated. Care was taken to ignore all the $J/\psi \to ll$ events in the generic backgrounds where this was appropriate to avoid double counting. Similarly, all true signal events were ignored in the $J/\psi \to ll$ sample when it was used to study background. To study the signal, 28,000 $B^0 \to J/\psi K_S^0, J/\psi \to ll, K_S^0 \to \pi^0\pi^0$ Monte Carlo events were used. Table

Sample	No. of events	Equivalent luminosity
$B^0 \to J/\psi K_S^0, J/\psi \to ll, K_S^0 \to \pi^0\pi^0$	28,000	-
$J/\psi \to ll$	143,000	$49.3 fb^{-1}$
$J/\psi \to ll$ with p^*cut at $1.5 GeV$	274,000	$238.7 fb^{-1}$
$B^0\overline{B}^0$	2,657,500	$5.06 fb^{-1}$
B^+B^-	3,682,800	$7.01 fb^{-1}$
$c\overline{c}$	5,757,800	$4.43 fb^{-1}$
$u\overline{u}/d\overline{d}/s\overline{s}$	9,149,900	$4.38 fb^{-1}$

Table 3.2: Monte Carlo Sample

3.2 shows the number of events of each type and the approximate equivalent luminosities.

Monte Carlo was produced by "overlaying" the generated physics events onto random events from real data, taken during periods when the beams were not crossing. In this way, accelerator induced backgrounds are included in the simulation.

To ensure correct modelling of a changing detector, the Monte Carlo simulation uses data on the actual condition of *BABAR* (voltage in the drift chamber, dead channels etc.). Monte Carlo samples are generated in batches corresponding to particular months of operation, and conditions data and non-crossing background events from the appropriate month are used. The number of generated events in each batch is proportional to the luminosity collected during that month.

Corrections were performed on this Monte Carlo to make it describe the data more accurately. They are described in Chapter 4, Section 4.2.

3.11.3 The $J/\psi \to l^+l^-$ Skim

To reduce CPU usage, a skim is performed so that only events with a good $J/\psi \to ll$ candidate are considered. The definition of this skim is:

- Events must pass the L3T selection in the standard way, as multi-hadron events, rather than as one of the samples used for calibration and monitoring (Section 3.10.2)

- The event must pass the multihadron selection used by the "B counting" analysis [22]. This is a simple selection based on event shape and number of tracks which seeks to exclude non $B\overline{B}$ events. It is described in detail in Section 4.1.
- A J/ψ or $\psi(2S) \to ll$ candidate must be reconstructed from the event that passes some very loose selection. This is identical to the loose selection described in Section 4.2.2 except that the accepted dilepton mass range is extended up to $4.2GeV$.

Events passing this skim are stored so that this CPU intensive first stage is not repeated. Both Data and Monte Carlo are skimmed in the same way.

Chapter 4

Reconstruction

4.1 Introduction

This chapter describes the reconstruction and selection of $B^0 \to J/\psi K^0_S (K^0_S \to \pi^0\pi^0)$ decays. Events selected using this method will then go on to be used for branching fraction and sin2β measurements in Chapters 5 and 6 respectively.

Section 2 describes selection on event variables. Section 3 describes the reconstruction of the J/ψ. In section 4, the reconstruction and selection of the K^0_S candidate is discussed. Section 5 contains the method of reconstruction of the B candidate, and the final cuts that are applied to it.

4.2 Pre-Selection

Events must pass the multi-hadron selection used by the "B counting" analysis [22] before candidates are reconstructed:

- The event must satisfy either the L3 EMC or L3 DCH triggers (see Section 3.10).
- The event vertex[1] must be within $0.5cm$ of the beam spot in x-y and within $6cm$ in the z co-ordinate[2].

[1] The event vertex is calculated by an iterative procedure that begins by vertexing all the tracks in the event, then discards those which contribute too large a χ^2 until the vertex is stable.

[2] The point of closest approach of a high momentum track to the beam spot is measured

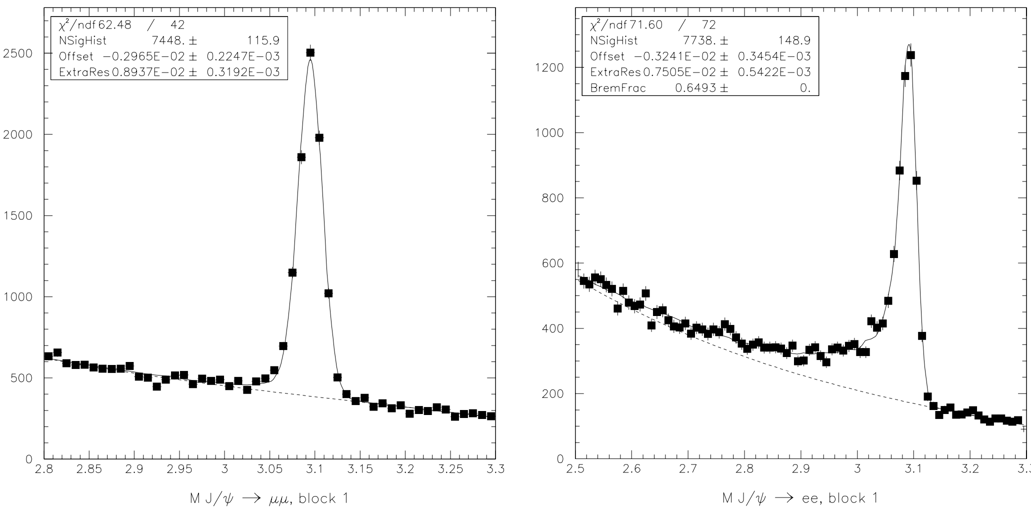

Figure 4.1: $J/\psi \to \mu^+\mu^-$ Inclusive, 1900V data (left), $J/\psi \to e^+e^-$Inclusive, 1900V data (right)

- Using only tracks in the region $0.41 < \theta_{lab} < 2.54$ and neutrals with energy $> 30MeV$ within $0.41rad < \theta_{lab} < 2.409rad$:
  - There must be at least 3 good tracks (defined in section 4.3.1).
  - R_2 (the ratio of the second to the zeroth Fox-Wolfram moment [25]) from these tracks and neutrals must be less than 0.5.
  - The total energy must be greater than $4.5GeV$.

Extensive studies have shown that this selection is $95.4 \pm 1.4\%$ efficient for $B\overline{B}$ events.

4.3 Reconstruction and Selection of the J/ψ

The tell tale signature of this channel is the presence of a $J/\psi \to ll$ candidate. The signal is clear above background, as shown in Fig 4.1 (much more so than the $K^0_S \to \pi^0\pi^0$, see Fig 4.4). In addition, PID can be used to reject fakes constructed from pions (see section 4.3.4), and the helicity of the J/ψ can be

with a resolution of $23\mu m$ in xy and $29\mu m$ in z (determined with dimuon events) [28]. The resolution of the beam spot is $\sim 100\mu m$ in the xy plane and $9mm$ in z.

used as a further discriminator (see section 4.5.1). In this analysis, J/ψ s are reconstructed when they decay to e^+e^-or $\mu^+\mu^-$. Both decays have branching ratios of $\sim 6\%$[12].

4.3.1 Track selection

Tracks are required to provide at least 12 hits in the drift chamber (a minimum requirement for momentum and dE/dx to be well measured). They must also have $p_T > 100MeV/c$, and the track must pass close to the nominal interaction point (within 1.5cm in xy and 3 cm in z). These will be referred to as *GoodTrackLoose* throughout the rest of this thesis.

4.3.2 Reconstruction and loose selection

J/ψ candidates are reconstructed from two oppositely charged tracks (defined in section 4.3.1).

For $J/\psi \to \mu^+\mu^-$ reconstruction:

- Both tracks are assigned the muon mass.
- Both tracks must pass the MIP selection (defined in Section 4.3.4).
- One track must pass the loose muon selection (defined in Section 4.3.4).
- The invariant mass is required to be in the range 2.8 to $3.3GeV/c^2$.

For $J/\psi \to e^+e^-$reconstruction:

- Both tracks are assigned the electron mass.
- The list is made from all combinations of tracks after applying a bremsstrahlung recovery procedure (described in section 4.3.3)
- One of the tracks is required to pass either the loose electron selector or the DCH Only selector (if not associated with an EMC cluster) (both described in section 4.3.4). No PID is required on the other track.
- The invariant mass is required to lie between 2.5 and $3.3GeV/c^2$.

If the same pair of tracks can be used to create both a $J/\psi \to \mu^+\mu^-$ and a $J/\psi \to e^+e^-$candidate, the $J/\psi \to \mu^+\mu^-$ is discarded.

4.3.3 Bremsstrahlung recovery

Bremsstrahlung radiation from electrons causes a large radiative tail in the $J/\psi \rightarrow e^+e^-$candidate mass distribution, resulting in a much lower efficiency for $J/\psi \rightarrow e^+e^-$candidates than for $J/\psi \rightarrow \mu^+\mu^-$. Photons are emitted very close in angle to the parent $e^{\pm}$ for both internal bremsstrahlung and bremsstrahlung in the detector material. A recovery algorithm is used to select photons close[1]to the direction of electrons and performs four vector additions to recreate the momenta of electrons before they emitted radiation. Around 20% of photons emitted as bremsstrahlung are recovered this way.

4.3.4 Lepton PID

A number of variables are used in Lepton ID. To identify electrons, information from both the drift chamber (dE/dx) and the calorimeter (E/p, number of crystals in which shower is detected and shower shape in the form of LAT [CITE]) is used. The cuts are summarised in Table 4.1.

To identify muons, information from the calorimeter and the IFR is used. The calorimeter allows a cut on deposited energy. With IFR information, it is possible to cut on:

- The number of IFR layers in which a hit is recorded (N_{layers})
- The total number of interaction lengths from the interaction point to the last layer of the IFR to be hit (N_{λ})
- The difference between N_{λ} and the expected value for a muon ($|N_{\lambda} - N_{\lambda}(expected)|$)
- Average number of strips hit per layer ($< N_{hit} >$)
- RMS strips hit per layer (RMS_{hit})

[1]For electrons, $\phi_{e^-} - 50mrad < \phi_{\gamma} < \phi_{e^-centroid}$ where $\phi_{e^-}$is the direction in ϕ of the track, ϕ_{γ} the direction of the photon and $\phi_{e^-centroid}$ the position in ϕ of the centroid of the calorimeter cluster associated with the track. Similarly for positrons, $\phi_{e^+} + 50mrad > \phi_{\gamma} > \phi_{e^+centroid}$. Also, photons must be within $35mrad$ of the track in θ. All photons within these ranges are used.

	DCH Only	Loose	Tight
$dE/dx_{measured-expected}$	-2σ to $+4\sigma$	-3σ to $+7\sigma$	-3σ to $+7\sigma$
E/p	-	0.65-5.0	0.75-1.3
$N_{crystals}$	-	> 3	> 3
LAT	-	-	0.0-0.6
Efficiency(%)	94.9	97.2	95.4
MissID(%)	21.6	4.8	1.2

Table 4.1: Electron PID summary

	MIP	Loose
$E_{EMC}(GeV)$	< 0.5	< 0.5
N_{layers}	-	> 1
N_λ	-	> 2
$\lvert N_\lambda - N_\lambda(exp)\rvert$	-	< 2.0
$< N_{hit} >$	-	< 10
RMS_{hit}	-	< 6
f_{hit}	-	> 0.2
χ^2_{IFR}	-	$< 4 \times N_{layers}$
χ^2_{match}	-	$< 7 \times N_{layers}$
Efficiency(%)	99.6	86.2
Miss ID(%)	57.9	7.0

Table 4.2: Muon PID summary

- If the track is in the forward IFR endcap, the "Continuity" (defined as f_{hit} =number of layers hit / number of layers between first and last layers to be hit)
- χ^2 of a polynomial fit to the IFR clusters (χ^2_{IFR})
- χ^2 of the geometric match between the associated track and the clusters in the IFR (χ^2_{match})

The cuts are summarised in table 4.2.

4.3.5 Final Selection

The invariant mass cuts are tightened to 3.06-3.14 for $J/\psi \to \mu^+\mu^-$ and to 2.95-3.14 for $J/\psi \to e^+e^-$. When the J/ψ decays to e^+e^-, one track is required to pass either the tight electron selector (described in Section 4.3.4) or the DCH Only selector (if not associated with an EMC cluster). No further PID is required for $J/\psi \to \mu^+\mu^-$ decays.

A fit is performed to determine the decay vertex of the J/ψ, and a kinematic fit is performed, with this vertex and the PDG [12] mass as constraints. The kinematic variables determined in this fit are used to reconstruct the B.

4.4 K^0_S to $\pi^0\pi^0$

Since neutral particles lack any tracking information, a candidate particle which decays only to neutrals has its mass and momentum determined using the amount and position of energy deposits in the calorimeter, and an assumed point of decay. At BaBar, this is the primary vertex by default. This default is a very poor choice for the K^0_S, which flies a significant distance before decaying. To improve the momentum and energy resolutions of the K^0_S, an attempt was made to determine its decay point (similar methods have been used in other experiments, the first in CPLEAR [23]). This section describes the reconstruction method for $K^0_S \to \pi^0\pi^0$ used in this analysis, and the properties (mass, energy position resolution) of K^0_S reconstructed in this way. It also includes a measurement of the relative efficiency ($K^0_S \to \pi^+\pi^-$/ $K^0_S \to \pi^0\pi^0$) for K^0_S ($E > 1.5GeV$) determined from $D^+_s \to K^0_S\, K^\pm$ and a comparison between data and Monte Carlo.

4.4.1 K^0_S to $\pi^0\pi^0$ Reconstruction

$K^0_S \to \pi^0\pi^0$ is reconstructed when both the π^0 s are resolved as 2 distinct γs (referred to as a composite π^0). They are also reconstructed when one of the π^0 s is observed as a single cluster in the EMC (known as a merged π^0) and the other is seen as 2 γs.

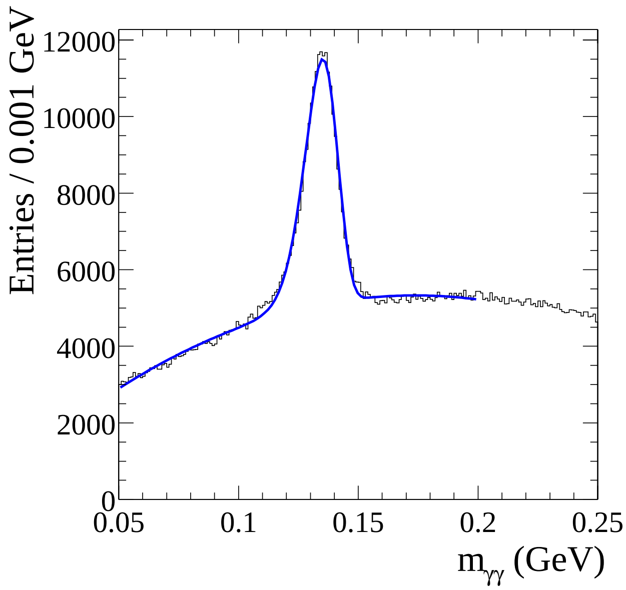

Figure 4.2: Inclusive $\gamma\gamma$ invariant mass

Photon Selection

The list of photons is created from neutral calorimeter objects. These are single bumps that are not matched with any tracks, have a minimum raw energy of 30 MeV, and a maximum lateral moment[1] [24] of 0.8. Electromagnetic showers have a lateral moment peaked at about 0.25.

π^0 Selection

The energy of reconstructed composite π^0 s is required to be $E_{\pi^0} > 200\,\mathrm{MeV}$, and the mass is required to be in the range 100-155 MeV/c^2 [2]. Fig 4.2 shows the inclusive $\gamma\gamma$ invariant mass ($E_\gamma > 30MeV, E_{\pi^0} > 300MeV$).

Photons from very high energy π^0s may be so close together in the Calorimeter that they cannot be resolved individually. These are included

[1]The lateral moment is a measure of the radial energy profile of the cluster, defined as $LAT = \frac{\sum_{i=3}^{N} E_i r_i^2}{\sum_{i=3}^{N} E_i r_i^2 + E_1^2 r_0^2 + E_2 r_0^2}$ where the cluster is composed of N crystals, of energy $E_1, E_2, ..., E_N$ ordered highest to lowest energy. r_0 is the average distance between the centers of the faces of neighboring crystals (about 5cm at BaBar). r_i is the distance between the crystal at the center of the cluster to crystal i.

[2]This mass is calculated with the assumption that the π^0 decayed at the origin.

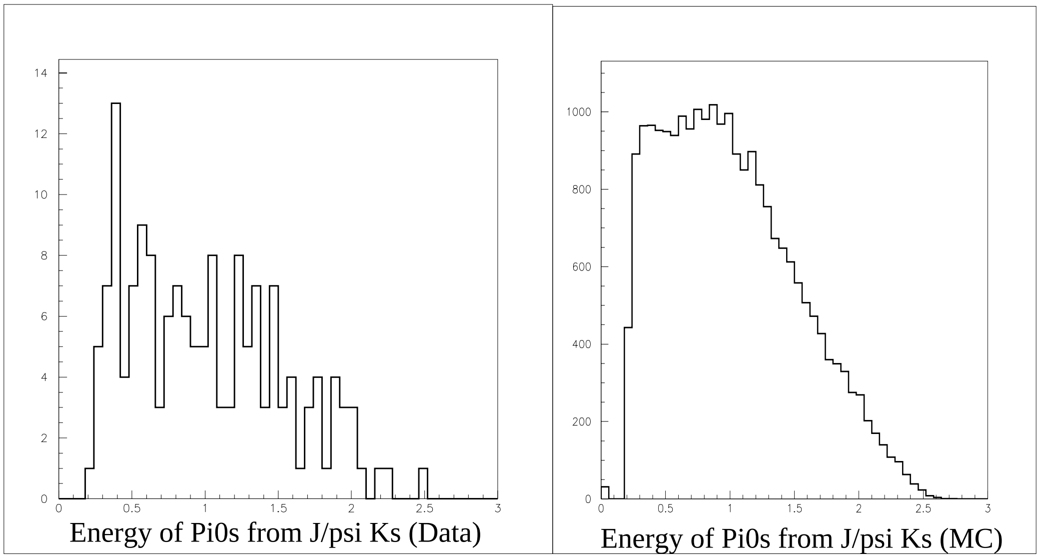

Figure 4.3: Energy of π^0s from $B^0 \rightarrow J/\psi K^0_S$ events, Data (left) and Monte Carlo (Right)

in the selection. Single bump merged π^0 candidates are Neutral Calorimeter objects with $E > 2.1GeV$ and a likelihood selection based on the shape of the cluster in the EMC. If the same EMC cluster candidate appears as both a merged π^0 and as part of a composite π^0, preference is given to the composite π^0 candidate.

Although merged π^0s are included in the selection, none of the final selected events are reconstructed from them (signal and Monte Carlo). This is expected - single bump merged π^0s effectively switch on at $3GeV$ and the π^0s from this decay are rare above $2GeV$ and effectively non-existent above $2.5GeV$ (see figure 4.3).

Mass fit of π^0 s

A mass fit is performed (at the origin) on composite π^0 s before they are used to reconstruct a K^0_S

Particle	Energy cut	Mass cut (MeV/c^2)
γ	30(MeV)	-
merged π^0	1(GeV)	-
composite π^0	200(MeV)	110-155
K_S^0	800(MeV)	340-600

Table 4.3: Summary of the cuts before fitting the K_S^0

K_S^0 Reconstruction (pre fit)

When $K_S^0 \to \pi^0\pi^0$ is reconstructed, $E_{K_S^0}$ is required to be $> 800\,\mathrm{MeV}$. The K_S^0 mass is required to be between 340 and $600\,\mathrm{MeV}/c^2$ [3]. Table 4.3 is a summary of all the cuts performed up to this point.

The K_S^0 fitting procedure

Figure 4.4 is a rough description of the procedure used to fit the K_S^0. The momentum of the K_S^0 (with its composite π^0 s fitted to their mass with the assumption that they decayed at the origin) is used to define the direction in which the K_S^0 is traveling. This direction is combined with the primary vertex of the event to define a flight path along which the candidate K_S^0 is believed to have traveled.

A region from -10cm to +40cm is defined along the length of this flight path (with zero being the primary vertex). The composite π^0 s are re-fitted (to their mass) at 2cm steps along this region, with the assumption that they both decayed at that point. For each point, the product of the fit probabilities $\mathrm{P}_1(\chi^2) \times \mathrm{P}_2(\chi^2)$ for the two π^0 s is recorded (for merged π^0 s, the probability is taken to be 1).

The point with the highest probability is assumed to be the K_S^0 decay point. The composite π^0 s are fitted to their mass with the assumption that they decayed at this point and the K_S^0 is reconstructed from them.

The inclusive invariant mass distribution for K_S^0 to $\pi^0\pi^0$ from run 1 data is shown in Fig 4.5.

[3] This mass is calculated with the assumption that the K_S^0 decayed at the origin.

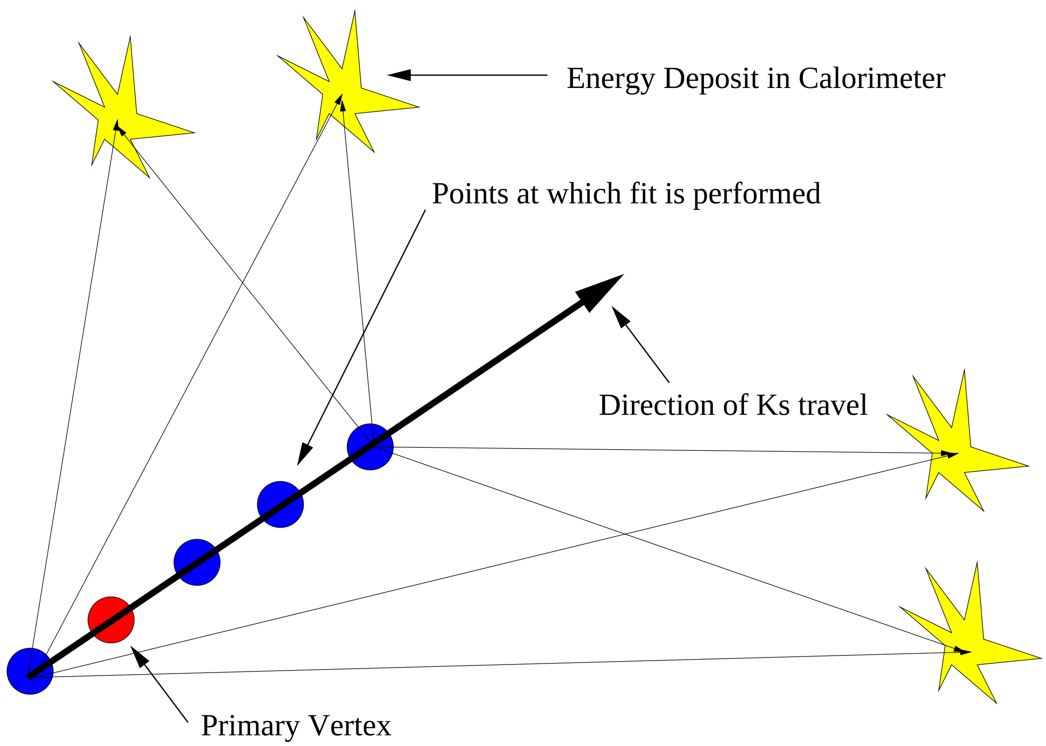

Figure 4.4: Schematic describing K_S^0 to $\pi^0\pi^0$ fit.

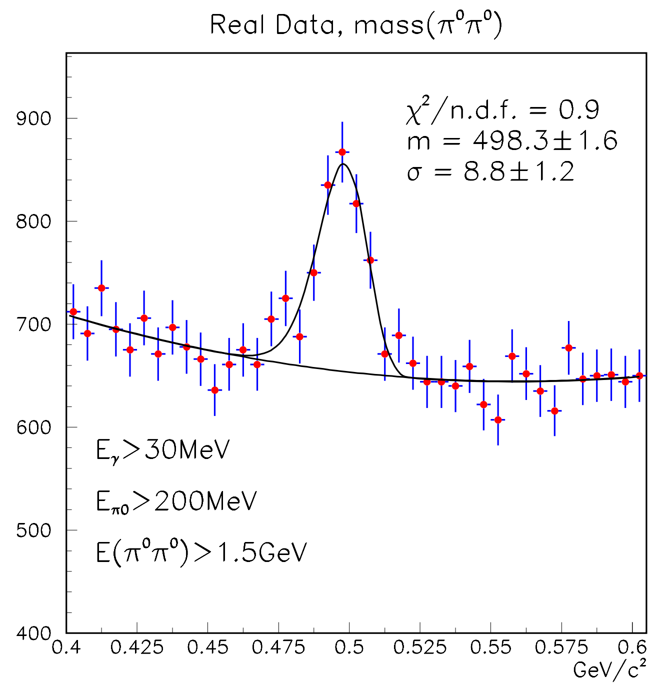

Figure 4.5: Invariant mass of the $K_S^0 \to \pi^0\pi^0$

MC type	number of events (10^6)	Equivalent Luminosity(fb^{-1})
$B^0\overline{B}^0$	4.203	8.0
$B^+ B^-$	4.933	9.4
$c\overline{c}$	12.086	9.3
uds	19.476	9.3

Table 4.4: Generic Monte Carlo used

Final K_S^0 to $\pi^0\pi^0$ Selection

After the fitting procedure described above, the invariant mass of the K_S^0 candidate is required to lie in the range 470 to $550 MeV/c^2$. In addition, when the K_S^0 is subjected to the fit, there must be one and only one point at which the probability is a local maximum. This an effective means of rejecting combinatoric background.

4.4.2 The properties of the K_S^0

Introduction

The MC sample used in this study is shown in table 4.4. Corrections were applied (described in section 5.2) to improve data - Monte Carlo agreement.

Mass resolution

Fig 4.6a shows the mass resolution of all truth matched K_S^0. The fit shown is a double Gaussian, with the two being of almost equal size, one with $\sigma_{mass} = 14.7 \pm .1\,\mathrm{MeV}$ and the other with $\sigma_{mass} = 8.4 \pm .1\,\mathrm{MeV}$. With a single Gaussian fit $\sigma_{mass} = 11.9 \pm .1\,\mathrm{MeV}$, and the peak is found to be at $498.3 \pm .1\,\mathrm{MeV}$.

Energy resolution

Fig 4.6b shows the reconstructed energy of the K_S^0 minus the true energy. It is fitted with a double Gaussian. The smaller, wider Gaussian is centered at $\delta_E = -44.0 \pm .3\,\mathrm{MeV}$ and has a width of $\sigma = 91.2 \pm .5\,\mathrm{MeV}$. The larger, narrower Gaussian is centered at $\delta_E = -9.29 \pm .01\,\mathrm{MeV}$ and has a width

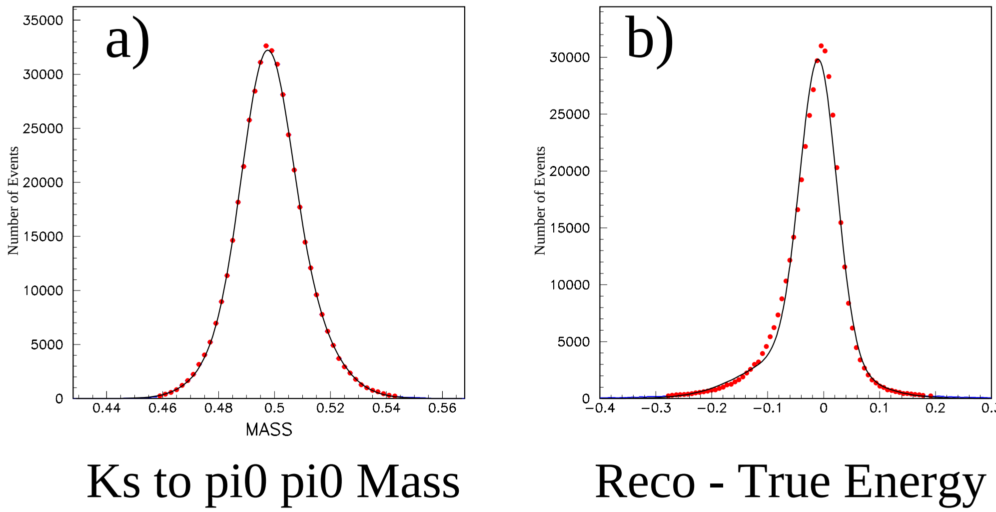

Figure 4.6: From $Ks \rightarrow \pi^0\pi^0$ truth matched Monte Carlo: Reconstructed K_S^0 mass (left) and Reconstructed-True Energy (right).

of $\sigma = 32.84 \pm .01\,\mathrm{MeV}$. The ratio of events in the narrow to those in the wide Gaussian is $\sim 6/1$. The smaller, broader Gaussian corresponds to K_S^0 candidates where 3 of the 4 photons are from a true K_S^0 and the fourth is from background.

Vertex resolutions

Reconstructed decay length - true decay length is shown in figure 4.7a. It is fitted with a double Gaussian. The smaller($\sim$ 1/3 of events), broader Gaussian is centered around +3cm and has a width of $\sigma = 6.37 \pm .02cm$, the larger and narrower is centered at +1mm, with a width of $\sigma = 2.96 \pm .02cm$.

Figure 4.7b shows the dependence of the energy resolution on the accuracy of the decay vertex - underestimating the radial distance causes an overestimation of the energy, and vice versa.

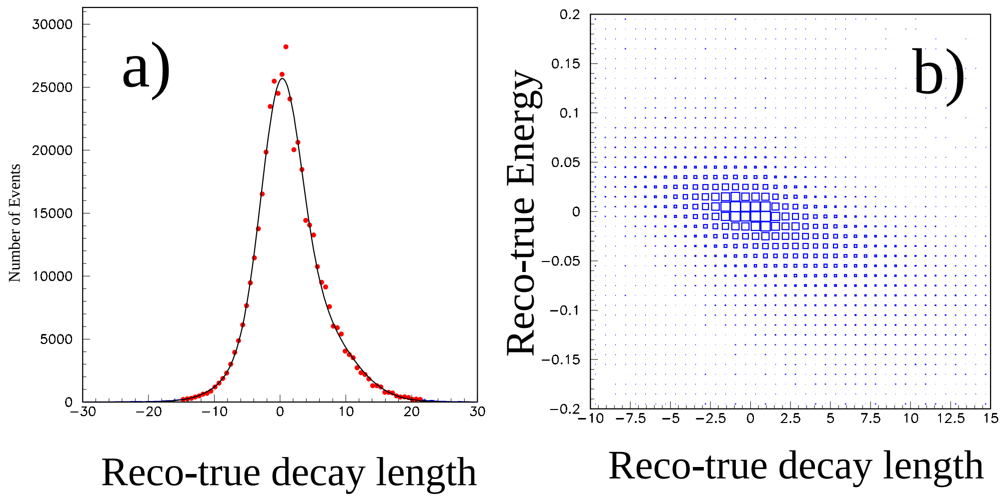

Figure 4.7: Decay length resolution (left) and energy resolution vs decay length resolution (right).

4.4.3 Relative efficiency of the $K_S^0 \to \pi^0\pi^0$ to $K_S^0 \to \pi^+\pi^-$

Introduction

Given that the reconstruction of the decay $K_S^0 \to \pi^+ \pi^-$ is simpler and easier to understand than the decay $K_S^0 \to \pi^0\pi^0$, and its efficiency therefore inherently easier to know, it makes sense to study the relative efficiency of reconstruction of the two decay channels rather than the absolute efficiency of $K_S^0 \to \pi^0\pi^0$. Here, the decays $D_s^+ \to K_S^0\ K^\pm$ are used to get a handle on the relative efficiency. With the non K_S^0 parts of the selection kept identical, the yields from $K_S^0 \to \pi^0\pi^0$ and $K_S^0 \to \pi^+ \pi^-$ give the relative efficiency.

Reconstruction of $D_s^\pm \to K_S^0\ K^\pm$

$K_S^0 \to \pi^0\pi^0$ are reconstructed as described in section 4.4.1. In addition, to clean up the signal a cut is applied to the helicity angle of the pions (to the direction of the K_S^0). The absolute value of it's cosine is require to be $< .8$. This cut was found to reduce efficiency by 20 ± 5(sys)% (systematic determined from cut variation).

$K_S^0 \to \pi^+ \pi^-$ are formed from two charged tracks. An invariant mass cut

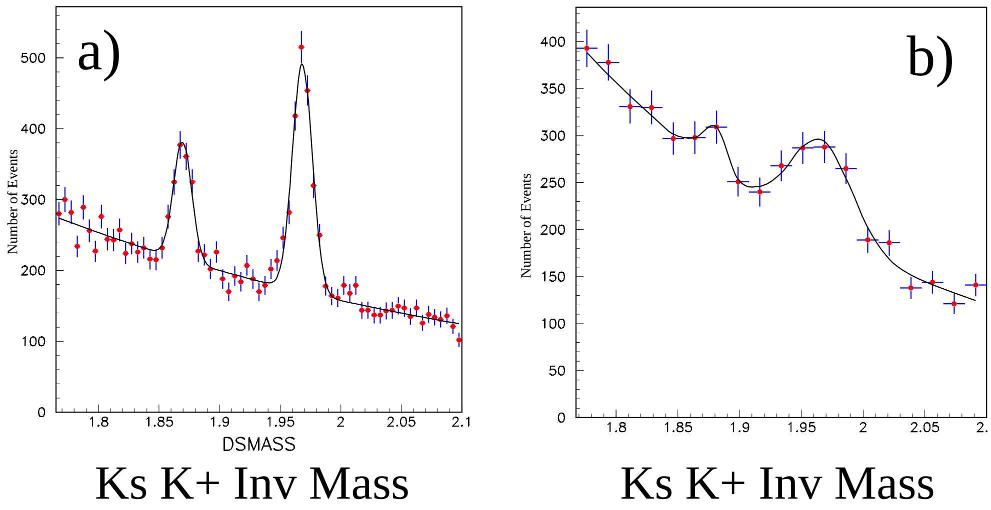

Figure 4.8: $K_s K^{\pm}$ Invariant mass in data: $K_s \to \pi^+\pi^-$ (left) and $K_s \to \pi^0\pi^0$ (right)

(489-507 MeV) is applied, and the decay vertex is required to be more than 1mm (in 3D) from the primary vertex. The K_S^0 is combined with a track which has been identified as a kaon by the DIRC. A cut of 3.2 GeV/c (in the center of mass) is applied to the momentum of the $D_s^{\pm}$.

Relative efficiency in Data from $D_s^{\pm} \to K_S^0\ K^{\pm}$

$20.7 fb^{-1}$ of data was used for this measurement. The invariant mass for the $K_S^0 \to \pi^0\pi^0$ plus an identified $K^{\pm}$ (reconstructed as described above) is shown in Fig 4.8b. The peak at 1.87 GeV is from $D^{\pm} \to K_S^0\ K^{\pm}$. The peak at 1.97 GeV is from $D_s^{\pm} \to K_S^0\ K^{\pm}$. The fit is two Gaussian plus an exponential background. At present, the fit on the $D^{\pm} \to K_S^0\ K^{\pm}$ peak is not convincing enough for it to be used in the efficiency measurement.

The invariant mass for the $K_S^0 \to \pi^+\ \pi^-$ plus an identified $K^{\pm}$ (reconstructed as described above) is shown in Fig 4.8a. Again, peaks from $D_s^{\pm} \to K_S^0\ K^{\pm}$ and $D^{\pm} \to K_S^0\ K^{\pm}$ are apparent. Two Gaussians plus an exponential background are used in the fit. The center of the D_s peak is found to be at $(1.967 \pm 0.004) GeV/c^2$ (this compares to the value of $(1.9685 \pm .0006) GeV/c^2$ quoted by [12]). Its width is measured to be $(24.3 \pm 3.2) MeV/c^2$.

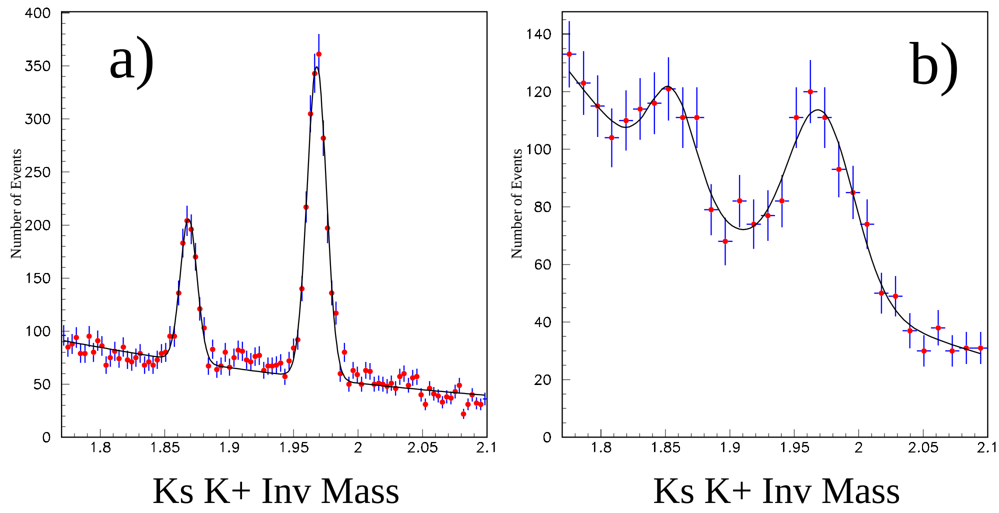

Figure 4.9: $K_s K^{\pm}$ Invariant mass from Monte Carlo: $K_s \to \pi^+\pi^-$ (left) and $K_s \to \pi^0\pi^0$ (right)

From the Gaussian fit, there are 349.8 $D_s^{\pm} \to K_S^0\ K^{\pm}$ where the $K_S^0 \to \pi^0\pi^0$, and 1889.9 where the $K_S^0 \to \pi^+\ \pi^-$. Since BR($K_S^0 \to \pi^0\pi^0$)=31.39±0.28% , BR($K_S^0 \to \pi^+\ \pi^-$)=68.6±0.28% and the effect of the helicity cut is to reduce the efficiency by 20%, the ratio efficiency($K_S^0 \to \pi^0\pi^0$)/efficiency($K_S^0 \to \pi^+\ \pi^-$) $= .51 \pm .03 \pm .03$.

Relative efficiency in MC from $D_s^{\pm} \to K_S^0\ K^{\pm}$

For this study, the Monte Carlo sample described in Table 4.4 was used. Corrections were applied (as described in section 5.2) to improve data - Monte Carlo agreement, but only to the K_S^0. The tracking efficiency and PID for the $K^{\pm}$ are not corrected, since that would reduce the statistics without improving the systematic. Scaling was used to ensure that different types of event were in the correct ratio.

The invariant mass of the K_S^0 plus an identified $K^{\pm}$ are shown in Fig 4.9b ($K_S^0 \to \pi^0\pi^0$) and Fig 4.9a ($K_S^0 \to \pi^+\ \pi^-$). Exponential plus 2 Gaussian functions are used for the fit, as for data. $D_s^{\pm}$ mass resolution is found to be $(26.7 \pm 3.4) MeV/c^2$ (in data, it was $(24.3 \pm 3.2) MeV/c^2$). Calculating as before, the ratio efficiency($K_S^0 \to\pi^0\pi^0$)/ efficiency($K_S^0 \to\pi^+\ \pi^-$) $= 0.56 \pm$

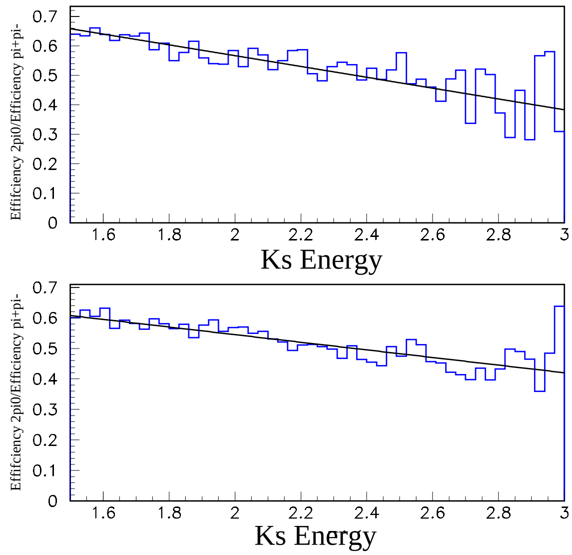

Figure 4.10: Relative efficiency, $K_S^0 \to \pi^0\pi^0/K_S^0 \to \pi^+\ \pi^-$ (DCH at 1900V top, 1960V bottom). Data/MC discrepancies introduce an 8% systematic.

0.03 ± 0.05.

Relative efficiency in MC, from $K_S^0 \to \pi^0\pi^0$ and $K_S^0 \to \pi^+\ \pi^-$.

Again, the Monte Carlo sample described in Table 4.4 was used. The $K_S^0 \to \pi^0\pi^0$ was reconstructed as described in section 4.4.1. The $K_S^0 \to \pi^+\ \pi^-$ is reconstructed as in section 4.4.3.

The relative efficiency as a function of energy is shown in Fig 4.10. Data/MC discrepancies introduce an 8% systematic on the relative efficiency (see for the means of evaluating K_S^0 systematics) if data and Monte Carlo are to be compared.

Conclusions to relative efficiency study

The relative efficiency ($K_S^0 \to \pi^0\pi^0/K_S^0 \to \pi^+\ \pi^-$) for K_S^0 ($E > 1.5GeV$) was determined from $D_s^+ \to K_S^0\ K^\pm$ (Data) and found to be $.51 \pm .03 \pm .03$. This compares well with the the same calculation from Monte Carlo, which is found to be $.56 \pm .03 \pm .05$. It also compares well with the inclusive K_S^0

relative efficiency in Monte Carlo, shown in Fig 4.10.

4.5 Reconstructing the B and final selection

The B is reconstructed from the addition of the J/ψ and the K_S^0. A helicity cut (see section 4.5.1) is performed, and then the events are divided up according to ΔE and m_{ES} (see section 4.5.2 for definition) into those reguarded as signal and those used for evaluating background.

4.5.1 Helicity

The helicity angle θ_l, defined as the angle (in the J/ψ rest frame) between the $l^-$and the K_S^0, is a powerful discriminator between signal and background. In the decay $B^0 \to J/\psi K_S^0$, since the K_S^0 is a pseudoscalar, the J/ψ must be longitudinally polarized, and the resulting θ_l distribution is proportional to $sin^2\theta_l$. For fake events, where the J/ψ candidate comes from light quark background, the θ_l distribution are observed to follow a $1+cos^2\theta_l$ distribution. Light quark events will be jet like, with fake J/ψs unlikely to be formed from two pions from the same jet. The K_S^0 will lie in one of the two jets and will be close in phase space to one of the candidate leptons. Hence signal peaks at $\cos(\theta_l) = 0$, and background at ± 1. Fig 4.11 shows signal and background distributions for $|\cos(\theta_l)|$, from data. For signal, events that pass all cuts (apart from helicity) and which fall in the signal box (as defined in Section 4.5.2) were used. Background events are taken from the ΔE signal region (Section 4.5.2), with masses below that required be in the signal box. The signal shown in this plot is background subtracted. Events with $|\cos(\theta_l)|$ greater than 0.9 are excluded from this plot.

$|\cos(\theta_l)|$ is required to be less than 0.7 and 0.8 for $J/\psi \to e^+e^-$and $J/\psi \to \mu^+\mu^-$ events respectively.

4.5.2 ΔE and m_{ES}

To isolate the B meson signal we use two variables which rely on true Bs being known to only come from $\Upsilon(4S) \to B^0\overline{B}^0$ decays (with the $\Upsilon(4S)$ being at

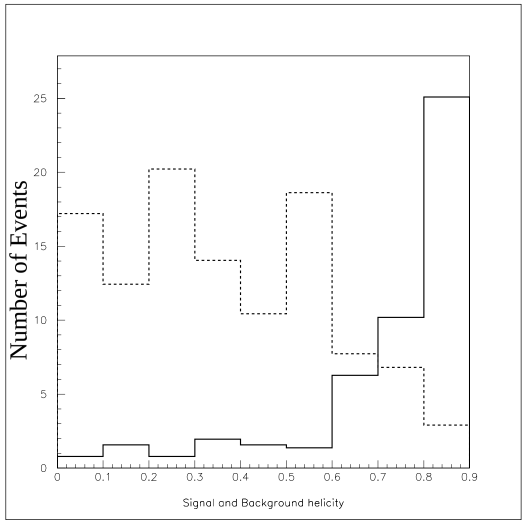

Figure 4.11: Background subtracted Signal (dotted line) and background (solid line) distributions of $|\cos(\theta_l)|$ (Data).

rest in the centre of mass) due to PEP-II's design.

ΔE is the difference between the reconstructed and expected energy of the B candidate in the centre of mass frame. $m_{\rm ES}$ is the energy substituted mass, defined as $m_{\rm ES} = \sqrt{(E_{cms}^2 - p_B^2)}$, where p_B is the momentum of the reconstructed B in the centre of mass frame and E_{cms} is the centre of mass energy derived from the beam energies. The calculation is performed using the beam energy recorded at the time the data was taken.

Events are divided up according to where they fall in the ΔE vs $m_{\rm ES}$ plane. Fig 4.12 shows where events lie in the ΔE vs $m_{\rm ES}$ plane for signal Monte Carlo . It also illustrates the different regions that it is divided up into. The *Grand Sideband* (or GSB) is defined as being $-.12GeV < \Delta E < .12GeV$, $5.2GeV < m_{\rm ES} < 5.3GeV$. The ΔE *region* is defined as the area of the GSB in which $-.1GeV < \Delta E < .1GeV$. The ΔE *sideband region* is defined as the area of the GSB in which $|\Delta E| > .1GeV$. The $m_{\rm ES}$ *region* is defined as the area of the GSB in which $|m_{\rm ES}| < M_{B^0_{PDG}} \pm .009GeV$ where $M_{B^0_{PDG}}$ comes from [12]. The *signal region* is defined as the area where the ΔE *region* and the $m_{\rm ES}$ *region* overlap, i.e. $|\Delta E| < .1GeV, |m_{\rm ES}| < M_{B^0_{PDG}} \pm .009GeV$.

Fig 4.13 (left) shows the $m_{\rm ES}$ in signal Monte Carlo from the selected

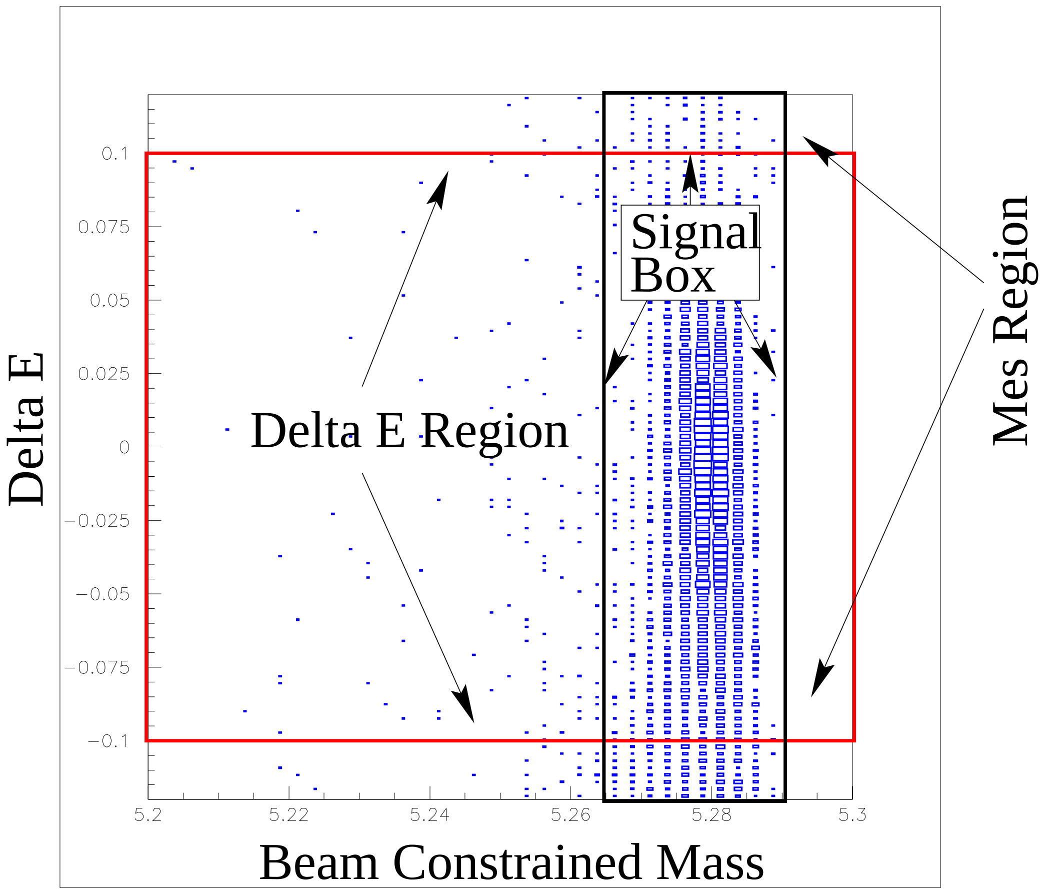

Figure 4.12: ΔE vs m_{ES}, Signal Monte Carlo

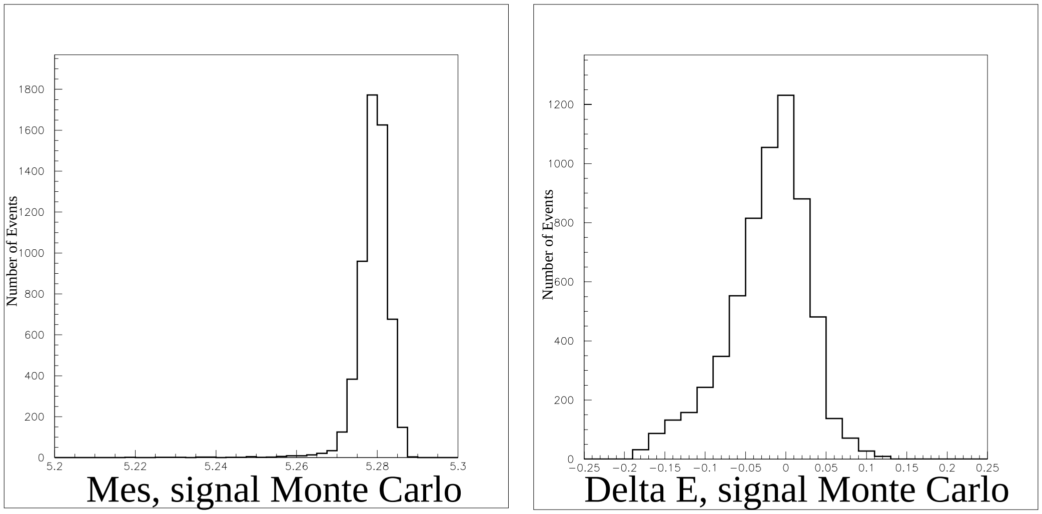

Figure 4.13: From Signal Monte Carlo: m_{ES} (left) and ΔE (right)

events which fall into the ΔE *region*. σm_{ES} is measured to be $(2.9 \pm 0.5) MeV/c^2$ in data.

Fig 4.13 (right) shows the ΔE in signal Monte Carlo from the selected events which fall into the m_{ES} *region*. $\sigma_{\Delta E}$ is measured to be $(37 \pm 9) MeV$ from data.

4.5.3 Multiple Candidates per Event

Only one exclusive candidate per event is considered possible (true to within 10^{-6}). In those cases where multiple candidates pass all cuts (except ΔE and m_{ES}, see section 4.5.2) the candidate with the smallest $|\Delta E|$ is taken and all others are rejected.

Chapter 5

Branching Fraction

5.1 Introduction

This chapter describes the measurement of the branching fraction BR($B^0 \rightarrow J/\psi K^0$), measured using the event selection described in Chapter 3 . On top of these requirements, however, an additional "fiducial" cut is applied. This ensures that the tracks are within the region of the detector in which particle identification is well understood. Both tracks of the J/ψ must be within $0.41rad < \theta < 2.409rad$ for electrons, within $0.3rad < \theta < 2.7rad$ for muons. $20.7fb^{-1}$ of data taken at the $\Upsilon(4S)$ at *BABAR* were used for this measurement. The additional $8.4fb^{-1}$ used for the sin2β analysis (see Chapter 5) was taken at a different time. The effects that possible changes in the detector might have on the efficiency of the selection have not yet been fully studied, so only the $20.7fb^{-1}$ from *BABAR* 's first year of running are used.

The branching fraction measurement is performed using the observed yield of $B^0 \rightarrow J/\psi K^0_S(K^0_S \rightarrow \pi^0\pi^0)$ in data, the estimated efficiency from Monte-Carlo, and the total number of BB events measured from data. The method of the measurement and the determination of its systematic errors are described in this chapter.

This analysis has already been published as a part of [6].

	$B^0 \to J/\psi K^0_S\, J/\psi \to e^+e^-$	$B^0 \to J/\psi K^0_S\, J/\psi \to \mu^+\mu^-$
Raw MC	16.2%	18.7%
+PID cor.	15.2%	18.5%
+γ eff. cor.	14.0%	17.2%
+ track smear	13.9%	17.2%
+trk eff. cor.	13.9%	17.1%

Table 5.1: Efficiency of selection, showing the cumulative effects of MC corrections.

5.2 Monte Carlo Correction

To reduce the systematic from Data/Monte Carlo discrepancies, an attempt was made to correct the Monte Carlo (the Monte Carlo sample is described in section 3.11.2) until it matched data more closely. Corrections were applied to:

- Lepton PID selection efficiency
- Photon detection efficiency
- Track momentum resolution
- Tracking efficiency

The cumulative effects of each of the efficiency corrections is shown in table 5.1 .

5.2.1 PID Selection Correction

The Monte Carlo fails to correctly describe the efficiencies for identifying leptons. This is corrected by replacing the normal PID selection with one using tables (in θ, ϕ,p_T) of efficiencies for lepton identification. The tables are worked out from real data, using tracks identified by some other means - for example Bhabhas where the other track has been identified as an electron.

5.2.2 Photon efficiency selection

It is necessary to adjust the single photon efficiency in Monte Carlo to match that which has been measured in the data . 2.5% of photons are randomly killed in Monte Carlo. This fraction is determined from a study of π^0 efficiency from τ 1-on-1 events [27]. This analysis also shows that no correction to the energy resolution or central value is appropriate.

5.2.3 Track momentum resolution

To correct for observed data/Monte Carlo discrepancies in the momentum resolution of tracks, the Monte Carlo is smeared according to a Gaussian distribution, by 1.32 times the default error on the momentum. This scale factor is determined by comparing the $\sigma_{\Delta E}$ of selected $J/\psi K^{\pm}$events (a clean, high statistics mode, see [6]) in data and Monte Carlo and choosing the value that makes the MC match the data. This is then cross-checked by comparing the J/ψ mass resolutions from the same events, were it is also seen to provide a close match to the data.

5.2.4 Tracking Efficiency Correction

The tracking efficiency was corrected by weighting B candidates for each track they contain, according to tables divided up in θ, ϕ,p_T and drift chamber voltage. The efficiency of the track selection is determined by identifying tracks in the SVT and observing what fraction also passes the track selection. The differences between data and Monte Carlo are then used to create the tables. These tables were then validated by an independant analysis using $\tau^+\tau^-$ 3-1 events.

5.3 Background

5.3.1 Background Evaluation

The sources of background can be divided up into two categories, according to its source:

- Background from continuum events and $B\overline{B}$ events without a J/ψ.
- Background from other $B \to J/\psi$ events.

It can also be divided up according to its expected shape in m_{ES}, within the ΔE *region*:

- "Continuum like" background that follows an Argus distribution [26].
- "Signal like" background that follows a Gaussian distribution and appears under the signal.

"Continuum like" background is evaluated in this analysis through fitting an Argus function[1] [26] plus a Gaussian function to the ΔE *region*.. The Gaussian accounts for the signal plus the "signal like" background. The Argus distribution follows the shape of the "Continuum like" background. Fig 5.1 shows this fit for $B \to J/\psi K^0_S (J/\psi \to e^+e^-, K^0_S \to \pi^0\pi^0)$. For these events, the "Continuum like" background is evaluated to be 7.3 ± 2.9[2]. Fig 5.2 shows this fit for $B \to J/\psi K^0_S (J/\psi \to \mu^+\mu^-, K^0_S \to \pi^0\pi^0)$. For these events, the "Continuum like" background is evaluated to be 4.9 ± 2.3.

"Signal like" background is estimated from Monte Carlo. It is found to come only from other $B \to J/\psi$ events (see sections 5.3.2). $B \to J/\psi$ Monte Carlo (the sample described in Section 3.11.2) was used to determine this background. Events passing the full selection and ending up in the ΔE *region* were fitted with an Argus plus Gaussian, as with the Data. In the signal region, the number of events under the Argus function was subtracted from the total number of events to give the "Signal like" background (after scaling to the appropriate luminosity). This was found to be 1.4 ± 0.7 for $B \to J/\psi K^0_S (J/\psi \to e^+e^-, K^0_S \to \pi^0\pi^0)$ and 0.9 ± 0.5 for $B \to J/\psi K^0_S (J/\psi \to \mu^+\mu^-, K^0_S \to \pi^0\pi^0)$.

[1] The Argus function is defined by $\frac{dN}{dM} = C \times M \times \sqrt{1 - \frac{M^2}{E^2_{beam}}}$ where M is the reconstructed mass and C is a constant. It is derived from the assumption that the background is uniformly distributed in the available phase space.

[2] This is the area of the Argus function within the signal box, i.e. $5.27 GeV < m_{\mathrm{ES}} < 5.288$

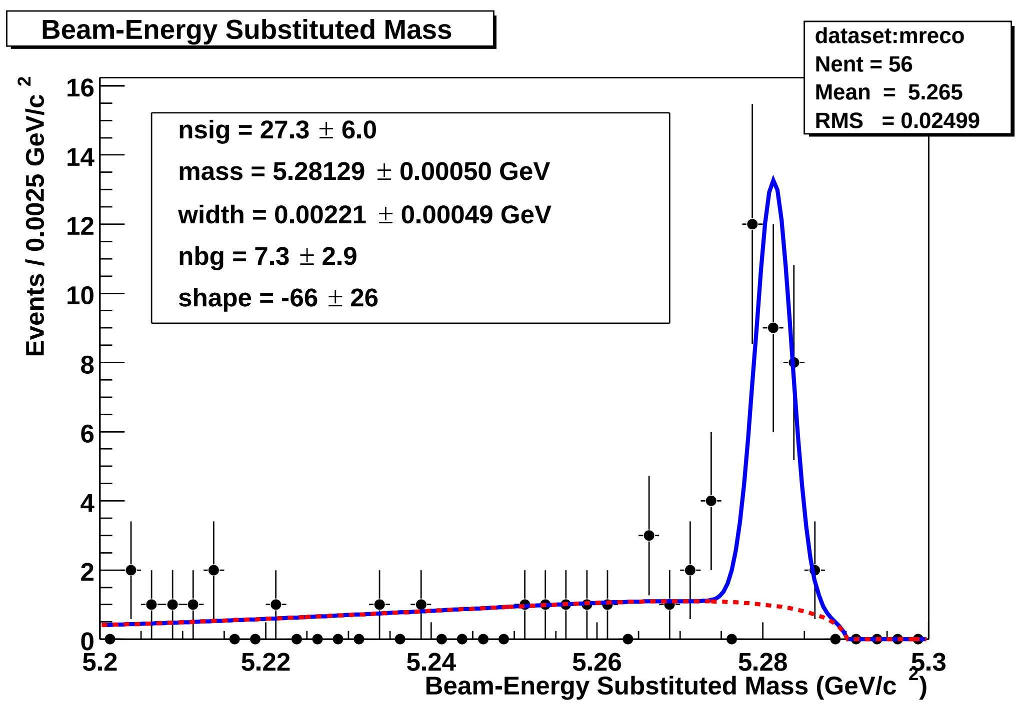

Figure 5.1: m_{ES} for $B \to J/\psi K_S^0 (J/\psi \to e^+e^-, K_S^0 \to \pi^0\pi^0)$ events in the ΔE *region*, fitted with Argus + Gaussian

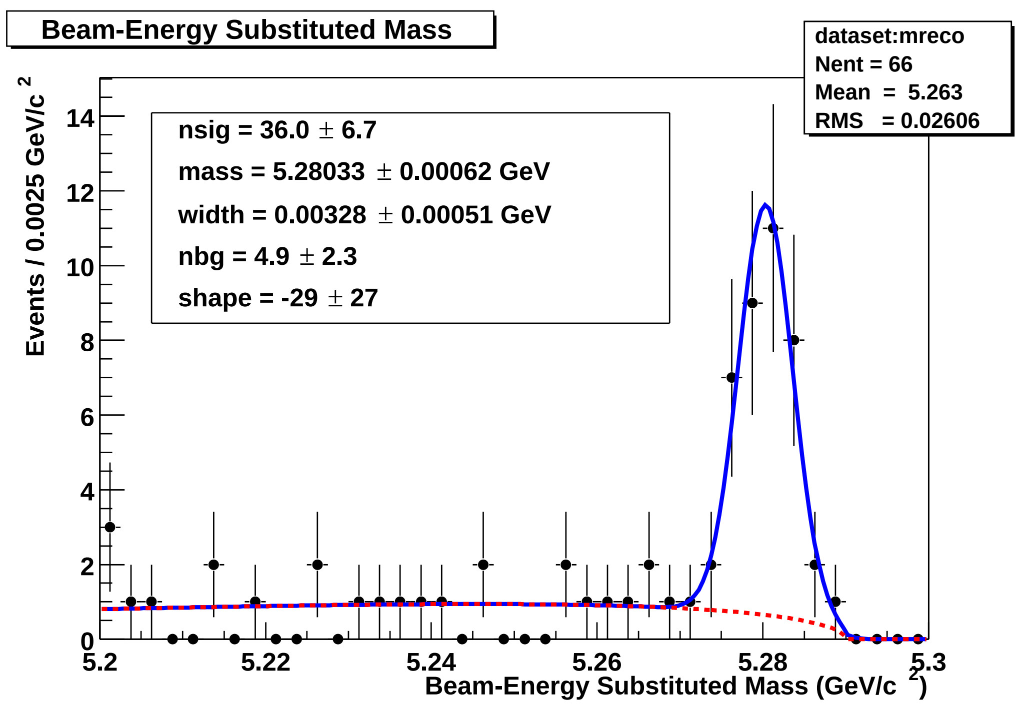

Figure 5.2: m_{ES} for $B \to J/\psi K_S^0 (J/\psi \to \mu^+\mu^-, K_S^0 \to \pi^0\pi^0)$ events in the ΔE *region*, fitted with Argus + Gaussian

	$J/\psi \to e^+e^-$	$J/\psi \to \mu^+\mu^-$	All
J/ψ mass sideband data	3.2 ± 1.4	2.6 ± 0.5	5.8 ± 2.2
Monte Carlo	5.8 ± 2.3	6.0 ± 2.2	11.8 ± 3.2

Table 5.2: Non J/ψ background data /Monte Carlo comparison

	$J/\psi \to e^+e^-$	$J/\psi \to \mu^+\mu^-$	All
Data	7.3 ± 2.9	4.9 ± 2.3	12.2 ± 3.7
Monte Carlo	6.5 ± 2.3	7.7 ± 2.2	14.2 ± 3.2

Table 5.3: Argus background data /Monte Carlo comparison.

5.3.2 Cross-checks on Background estimation

It is possible to make a comparison between non J/ψ data and non J/ψ Monte Carlo. To do this it is necessary to exclude real J/ψs in data by using the sidebands of the J/ψ mass[3]. After an Argus fit, the number of events predicted by the Argus function to be in the signal box is compared to the appropriate mixture of $u\ d\ s$, $c\ \bar{c}$ and $B\overline{B}$ Monte Carlo events (with true J/ψ events removed). Table 5.2 shows reasonable agreement.

The "Continuum like" background evaluated from the Argus fit to the data can be compared with the values estimated from an Argus fit to Monte Carlo ($u\ d\ s$, $c\ \bar{c}$ $B\overline{B}$ and J/ψ inclusive). The comparison is shown in table 5.3.

The evaluation of the "Signal like" background is cross-checked by comparing the ΔE sideband region in Data and Monte Carlo ($u\ d\ s$, $c\ \bar{c}$ $B\overline{B}$ and J/ψ inclusive and signal). There is a large fraction of "Signal like" background in this region, and little true signal. The size of the Gaussian in a combined Argus + Gaussian fit to data in this region can be compared with the value predicted by Monte Carlo. The normalisation of the signal Monte

[3]The definition of the sidebands depends on the decay mode of the J/ψ. For the decay $J/\psi \to \mu^+\mu^-$ the sideband is defined as the regions of invariant mass $3.156 < M_{\mu\mu} < 3.3$ Gev/c^2 and $2.98 < M_{\mu\mu} < 3.024\ GeV/c^2$. For the decay $J/\psi \to e^+e^-$the sideband is defined as the mass region $3.156 < M_{ee} < 3.3\ GeV/c^2$. The results are multiplied by a scaling factor in order to give the correct normalization for events which would lie within the J/ψ mass window.

	$J/\psi \to e^+e^-$	$J/\psi \to \mu^+\mu^-$	All
Data	5.4 ± 4.8	4.6 ± 2.2	10.0 ± 5.3
Monte Carlo	3.8 ± 0.7	4.1 ± 0.8	7.9 ± 1.1

Table 5.4: Gaussian fit in sidebands, data and Mont Carlo.

Carlo is from the value of the $J/\psi K^0$ branching ratio quoted in [12]. Fitting Argus+Gaussian, the comparison of the Gaussian integrated between 5.27 and 5.288 in M_{ES} is shown in Table 5.4. The agreement is good, and the difference is used to determine the systematic on the "signal like" background (see Section 5.5.5).

5.4 Branching Fraction Calculation

5.4.1 Efficiency calculation

The efficiency is defined as the fraction of events in the signal Monte Carlo (Section 3.11.2) after correction (Section 5.2) which pass the analysis cuts and are reconstructed in the *signal region* in the $\Delta E/m_{\mathrm{ES}}$ plane. The efficiency is measured to be 13.9% for $B^0 \to J/\psi K^0_S (J/\psi \to e^+e^-)$ and 17.1% for $B^0 \to J/\psi K^0_S (J/\psi \to \mu^+\mu^-)$ (statistical errors on these are included in the systematic estimate).

5.4.2 Event Yield

A count is made of the events in the *signal region* in the $\Delta E/m_{\mathrm{ES}}$ plane. This gives 36 ± 6.0[1] $B^0 \to J/\psi K^0_S (J/\psi \to e^+e^-)$ candidate events and 41 ± 6.4 $B^0 \to J/\psi K^0_S (J/\psi \to \mu^+\mu^-)$ candidate events. The "continuum like" background is subtracted from this (7.3 ± 2.9 for $B^0 \to J/\psi K^0_S (J/\psi \to e^+e^-)$ and 4.9 ± 2.3 for $B^0 \to J/\psi K^0_S (J/\psi \to \mu^+\mu^-)$) as is the "signal like" background (1.4 ± 0.7 for $B^0 \to J/\psi K^0_S (J/\psi \to e^+e^-)$ and 0.9 ± 0.5 for $B^0 \to J/\psi K^0_S (J/\psi \to \mu^+\mu^-)$). This leaves 27.3 ± 6.7 observed signal events for $B^0 \to J/\psi K^0_S (J/\psi \to e^+e^-)$ and 35.2 ± 8.1 for $B^0 \to J/\psi K^0_S (J/\psi \to \mu^+\mu^-)$.

[1] At this point, all errors are statistical.

	$J/\psi K^0_S(J/\psi \to e^+e^-)$	$J/\psi K^0_S(J/\psi \to \mu^+\mu^-)$
Events in signal box	36 ± 6.0	41 ± 6.4
"Continuum like" BG	7.3 ± 2.9	4.9 ± 2.3
"Signal like" BG	1.4 ± 0.7	0.9 ± 0.5
Observed signal	27.3 ± 6.7	35.2 ± 8.1
Efficiency from MC	13.9%	17.1%
$\Rightarrow$ Events in Data	196.4 ± 48.2	205.8 ± 47.4

Table 5.5: Summary of Event Yield Calculation

Given the efficiency determined in section 5.4.1, this implies that there were 196.4±48.2 $B^0 \to J/\psi K^0_S(J/\psi \to e^+e^-, K^0_S \to \pi^0\pi^0)$ events and 205.8±47.4 $B^0 \to J/\psi K^0_S(J/\psi \to \mu^+\mu^-, K^0_S \to \pi^0\pi^0)$ events in the data sample analysed.

The values obtained in this section are sumarised in table 5.5.

5.4.3 Branching Fraction Calculation

The branching fraction is determined as follows:

$$BF = \frac{N_{observed}}{N^{B\overline{B}} \times \sum_i \epsilon_i f_i} \tag{5.1}$$

where $N^{B\overline{B}}$ is the number of produced $B\overline{B}$ events, i sums over all the secondary decays considered and f_i and ϵ_i are the associated branching fraction (as quoted in [12]) and the selection efficiency respectively. $N_{observed}$ is the number of signal events observed as given in section 5.4.2.

$N^{B\overline{B}}$ is determined through the use of the B counting analysis described in [22]. When the event selection (described in section 4.2) is applied to the entire data set (pre-skim), the number of events that pass and the known efficiencies for $B\overline{B}$ and $non - B\overline{B}$ events allows $N^{B\overline{B}}$ to be calculated. It is found to be $22.72 \pm 0.36 \times 10^6$.

The statistical error on the branching fraction is determined as:

$$\sigma_{BF} = \frac{\sqrt{N_{observed} + \sigma_{cl}^2 + \sigma_{sl}^2}}{N^{B\overline{B}} \times \sum_i \epsilon_i f_i} \tag{5.2}$$

where σ_{cl}^2 and σ_{sl}^2 are the errors on the "signal like " and "continuum like" backgrounds, respectively.

Performing these calculations, BR($B^0 \to J/\psi K^0$) (calculated from $B^0 \to J/\psi K_S^0 (J/\psi \to e^+e^-)$ events) is $(9.4 \pm 2.3) \times 10^{-4}$ and BR($B^0 \to J/\psi K^0$) (calculated from $B^0 \to J/\psi K_S^0 (J/\psi \to \mu^+\mu^-)$ events) is $(9.8 \pm 2.3) \times 10^{-4}$. Using all events together, BR($B^0 \to J/\psi K^0$) is measured to be $(9.6 \pm 1.5) \times 10^{-4}$ (statistical errors only).

5.5 Systematics on the Branching Fraction Calculation

Systematic errors on the Branching fraction measurement break down into eight categories:

- Systematic error on the number of $B\overline{B}$ events - 1.4%
- Uncertainty on the efficiency calculating arising from Monte Carlo statistics - 1.6%
- Data/Monte Carlo discrepancies for tracks - 4.2%
- Data/Monte Carlo discrepancies for neutrals - 5.2%
- Data/Monte Carlo discrepancies in PID selections - 0.5%
- Uncertainties in the branching fractions of the secondary decays - 1.9%
- Systematic errors in background determination - 2.0%
- Systematics brought in through other cuts and selection. - 2.6%

The details are considered below.

5.5.1 Systematic error on the number of $B\overline{B}$ events

This error is determined as part of the "B counting" analysis [22]. It is found to be 1.4%.

5.5.2 Monte Carlo Statistics

52,000 Monte Carlo events are used to determine the efficiency. The statistical error on these events is 1.6%.

5.5.3 Data/Monte Carlo discrepancies for tracks

It is possible that there is a difference in the momentum scale between data and Monte Carlo. Flaws in the determination of the SVT alignment, an imperfect description of the detector geometry or material and uncertainties in the magnetic field can all lead to this effect. To determine the potential systematic error, the smearing parameter (described in Section 5.2.3) was varied around the central value used to correct the Monte Carlo. The analysis which determined the smearing value for the correction also evaluated the uncertainty on that correction, and the smearing was varied by $\pm 1\sigma$. The efficiency was found to vary by 0.1%, and this is taken as the systematic.

All the reasons above could also lead to a difference in the efficiency of track reconstruction and selection between data and Monte Carlo. This systematic is evaluated to be 1.2% per track (the uncertainty in the measured track efficiency in data - see section 5.2.1). These errors are combined linearly.

In addition, to account for any difference in the shape or central value of the J/ψ mass spectrum (in particular through a failure in the modelling of Bremsstrahlung) J/ψ mass cuts were varied by $\pm 1\sigma$, and the branching fraction measurement was repeated. The Branching ratio was found to change by 3.4%. This was taken as an additional systematic.

Combined in quadrature, $\sqrt{0.1^2 + (2 \times 1.2)^2 + 3.4^2} = 4.2\%$.

5.5.4 Data/Monte Carlo discrepancies for neutrals

An imperfect description of the EMC efficiency and resolution for neutral particles in Monte Carlo would lead to systematic errors in the branching fraction, as would incorrect moddeling of material in the inner part of the detector. The tau analysis [27] used in Section 5.2.4 to give the correction to the Monte Carlo also gives the limits to how well the efficiency, resolution and energy scale are known. The energy resolution is known to within $\pm 1.5\%$, and the possible shift of central values for energy is measured to be $0 \pm 0.75\%$. Smearing of photon resolution (at $\pm 1.5\%$) and shift of photon energy (at $\pm 0.75\%$) is carried out on Signal Monte Carlo events. The systematic from these effects is measured to be 1.4%.

As an additional systematic check, the BF calculation was repeated with the mass cut on the K^0_S varied by $\pm 1\sigma$. There was a difference of 1.2% between the two extremes, suggesting a systematic effect of $\pm 0.6\%$. Since this is significantly smaller than 1.4% smearing/shifting systematic which should be included in it, no additional systematic was added.

The τ analysis evaluates the single photon efficiency to within 1.25%. The systematic is therefore determined to be $1.25\% \times 4 = 5.0\%$ (added linearly).

Combined in quadrature, $\sqrt{1.4^2 + 5.0^2} = 5.2\%$

5.5.5 Data/Monte Carlo discrepancies in PID selections

This systematic comes from lack of knowledge of the lepton identification efficiencies. This has been determined by evaluating the efficiencies of the PID selections from inclusive J/ψ yields, and taking the difference between this and the efficiency predicted by Monte Carlo. It is found to be 0.1% for e^+e^-, 0.5% for $\mu^+\mu^-$, which when combined in quadrature gives a systematic of 0.5%.

5.5.6 Uncertainties in the branching fractions of the secondary decays

These are taken from from [12]. The uncertainty in the branching fraction of $K^0_S \to \pi^0\pi^0$ is 0.9%. The uncertainty in the $J/\psi \to e^+e^-$branching fraction is 1.7%. The uncertainty in the $J/\psi \to \mu^+\mu^-$ branching fraction is also 1.7%. Combined in quadrature, $\sqrt{0.9^2 + 1.7^2} = 1.9\%$.

5.5.7 Systematic errors in background determination

A possible source of systematic error is in the shape of the Argus function which is used to model the background. In the fit used to determine the "continuum like" background, the parameters of the Argus function are not constrained. To determine the systematic error from the fit, an additional fit is performed where the parameters of the Argus function, except for the normalisation, are fixed instead to those obtained from fits to the ΔE sidebands. The branching fraction is found to change by 1.9%

Another source of systematic error is the quality of modelling of "signal like" background in the Monte Carlo. ΔE *sidebands* are studied, as they contain a much larger proportion of J/ψ background than the signal box. By comparing the observed Gaussian component in the sideband with that predicted by Monte Carlo, any failure in the Monte Carlo is apparent. A scale factor is taken from the difference between data and Monte Carlo. The *signal like* background is scaled by this factor, and the change in the BF is taken as the systematic error. It is found to be 0.6%.

Combined in quadrature, $\sqrt{1.9^2 + 0.6^2} = 2.0\%$.

5.5.8 Systematics brought in through other cuts and selection.

There are two additional cuts whose effects on the systematic error are not covered by any of the evaluations above[1]. The systematic from the helicity cut is evaluated by varying it by± 0.05 and re-evaluating the branching ratio, and this is found to be 0.3%. The systematic brought in by requiring that that the K_S^0 has one and only one maximum in its probability is determined by repeating the measurement without the cut - the branching fraction changes by 0.5%, and this is taken as the systematic.

The selection of a B candidate (when there is more than one in an event) on the basis of it having the lowest ΔE is a potential source of systematic error. This error is evaluated by repeating the branching fraction calculation

[1]The systematics of the event selection cuts (section 4.2) are covered in the systematic error on the number of $B\overline{B}$ events.

Sample	$BR(B^0 \to J/\psi K^0) \times 10^{-4}$
$J/\psi K^0_S(K^0_S \to \pi^0\pi^0)$	$9.6 \pm 1.5_{stat} \pm 0.7_{syst}$
$J/\psi K^0_S(K^0_S \to \pi^+\pi^-)$	$8.5 \pm 0.5_{stat} \pm 0.6_{syst}$
$J/\psi K^0_L$	$6.8 \pm 0.8_{stat} \pm 0.8_{syst}$
Combined BABAR result	$8.3 \pm 0.4_{stat} \pm 0.5_{syst}$
PDG2001	9.6 ± 0.9

Table 5.6: Measured values of $BR(B^0 \to J/\psi K^0)$

with candidates selected randomly, rather than by ΔE. The error is found to be 2.5%.

Combined in quadrature, $\sqrt{0.3^2 + 0.5^2 + 2.5^2} = 2.6\%$

5.6 Summary of BF Measurement

$BR(B^0 \to J/\psi K^0)$ was measured to be $9.6 \pm 1.5_{stat} \pm 0.7_{syst}$ using events where one of the Bs had decayed to $J/\psi K^0_S$ (with the J/ψ decaying to two leptons and the K^0_S decaying to $\pi^0\pi^0$) from data collected at the *BABAR* experiment. $BR(B^0 \to J/\psi K^0)$ has been previously measured at other experiments and is listed in [12]. $BR(B^0 \to J/\psi K^0)$ can also be measured with other decays, and these independent measurements can be used for comparison (values taken from [6]). Table 7.1 shows all the measurements of $BR(B^0 \to J/\psi K^0)$ made at *BABAR,* and the PDG value. The BaBar results shown here have been approved for publication [6]. In addition, the agreement between the $J/\psi K^0_S(K^0_S \to \pi^0\pi^0)$ measurement and all the others proves that the composition of the sample is well understood (important when it is used to measure sin2β in the next chapter).

Chapter 6

sin2β

6.1 Introduction

This chapter describes a measurement of the Unitary Triangle parameter sin2β. The event selection described in Chapter 3 is used to provide a sample of events where one of the Bs is reconstructed in a CP eigenstate. In addition, another sample of events is used in one B is reconstructed in a state which identifies its flavour. This sample (referred to as B_{flav}) is described in Appendix A.

The data sample used is the $20.7 fb^{-1}$ from BaBar's first year of running together with $8.4 fb^{-1}$ from its second year. Although many aspects of the data from the second year have not been fully studied at time of writing, anything that could affect the sin2β measurement has been analysed very thoroughly (e.g. vertex resolution and mistag rates).

Since the effect to be observed is a (time dependent) difference in the decay rate between B^0 and $\overline{B}^0$, a measurement of B flavour is required. Experiments operating at CM energies above the $\Upsilon(4S)$ resonance [31, 33, 32] can tag the flavour of the B which decays to the CP eigenstate (the "CP B") from particles in the same jet. BaBar, however, tags the flavour of the other B (the "tagging B"). Since the $B^0\overline{B}^0$ pair evolve coherently, this identifies the flavour of the CP B at the time of the tagging B's decay (the CP B continues to oscillate until it too decays). The method used to tag the B is described in Section 2.

As mentioned in Chapter 1, the CP violation expected to be observed in $J/\psi K_S^0$ decays is time dependent, and indeed over time integrates to 0. It is therefore necessary to measure the decay rate as a function of decay time. $\Upsilon(4S) \to B^0\overline{B}^0$ decays produce Bs almost at rest in the CM, and the CM has a boost of $\beta\gamma = 0.56$ relative to the lab frame. As a result, decay time is measured at BaBar through accurately measuring the position of the decay vertex along the z axis. The method of measuring vertex position is described in Section 3.

To extract sin2β from this information, an unbinned maximum likelihood fit is performed. This procedure is described in section 4. The program used to perform this procedure is tFit [29]. Section 5 describes the systematic errors associated with this measurement.

This analysis contributed to the first observation of CP violation in the B system. This observation was made by BaBar in July 2001 and is published in [1]. It is described in more detail in [30], although that document is out of date on some aspects of the fitting procedure.

6.2 Tagging

6.2.1 Tagging Method

Several different techniques are used to determine the flavour of the "other" B in the event (the one not fully reconstructed[1]). Fast leptons and charged kaons can be used to identify the flavour of the tagging B. If these methods fail, a neural net approach can be used to determine the flavour of the B from the rest of the information in the event. The event is given a category dependent on the method used to tag it. These categories are mutually exclusive and hierarchical. Events that can be tagged by more than one method are assigned the tag and the category of the most accurate technique. The most accurate method is by primary lepton, followed by kaon charge. Neural net tags are split up into two categories, NT1 and NT2, in order of accuracy.

[1] Tracks and neutrals used in the reconstruction of the CP or flavour B are excluded from the tagging.

	Very Tight
$dE/dx_{measured-expected}$	-2.2σ to $+4\sigma$
E/p	0.89-1.2
$N_{crystals}$	> 3
LAT	0.1-0.6
Efficiency(%)	91.5
MissID(%)	0.13

Table 6.1: Electron PID summary

Tagging performance can be described using a number of parameters. Efficiency (ϵ) is the fraction of B^0 events for which a tag can be established (right or wrong). ω is the mistag fraction, the percentage of tags that incorrectly determine the B flavour. The dilution $D = 1 - 2w$ is the scaling factor to account for the distortion of the sin2β result by mistags. Finally $Q = \epsilon(1-2\omega)^2$ is a measure of the quality of the tagging - the error on sin2β goes as $1/\sqrt{Q}$.

Primary Lepton Tagging

Primary leptons, i.e. from the direct decay $B^0 \to l^+\nu_l X$ +c.c., are an effective means of tagging the flavour. They generally have high energies, enabling them to be discriminated from cascade leptons ($b \to c \to l$) by a p^*cut (1.0 GeV for electrons, 1.1 GeV for muons). PID requirements are also placed on them - similar to those used in J/ψ track selection, but tighter. They are shown in tables 6.1 and 6.2. Terms are explained in section 4.3.4.

Charged Kaon Tagging

According to [12], B^0 decays to a final state involving a K^+ $78 \pm 8\%$ of the time, with $\overline{B}^0$ going to K^- with the same probability. Although $B^0 \to K^- + X$ decays can occur, they are much rarer, and therefore total kaon charge is a very effective tagging method.

Kaons are identified at BaBar by using the DIRC (see section 3.5). Fig 3.7 shows the discriminating power and efficiency of this method. If the total

	Tight
$E_{EMC}(GeV)$	$< 0.4, > 0.05$
N_{layers}	> 1
N_{λ}	> 2
$\lvert N_{\lambda} - N_{\lambda}(exp)\rvert$	< 1
$< N_{hit} >$	< 8
RMS_{hit}	< 4
f_{hit}	> 0.3
χ^2_{IFR}	$< 3 \times N_{layers}$
χ^2_{match}	$< 5 \times N_{layers}$
Efficiency(%)	75
Miss ID(%)	3.0

Table 6.2: Muon PID summary

charge of all the kaons in the event is positive, the B is tagged as a B^0, and vice versa.

Neural Net Tagging

Neural nets are used to identify kaon or direct lepton tags that may have been missed by the cut based approaches. In addition, a Neural net is devoted to trying to tag the event using soft pions from $D^{*\pm}$ decays, where a soft π^-implies a B^0(and c.c.). The results of each of these three sub-nets are combined to provide a single output, the probability that the tagged B is a B^0. Events with a high probability are tagged as B^0, and those with a low probability as $\overline{B}^0$. In addition, depending on the probability, the tags are placed in one of two categories - NT1, rarer but less likely to be wrong, and NT2, more common but less accurate. Figure 6.1 shows the output of the Neural net, the way the tagging decisions are made and a comparison between data and Monte Carlo.

Since all the best information has already been used by the two other tagging methods, the Neural Network makes only a small contribution to the tagging.

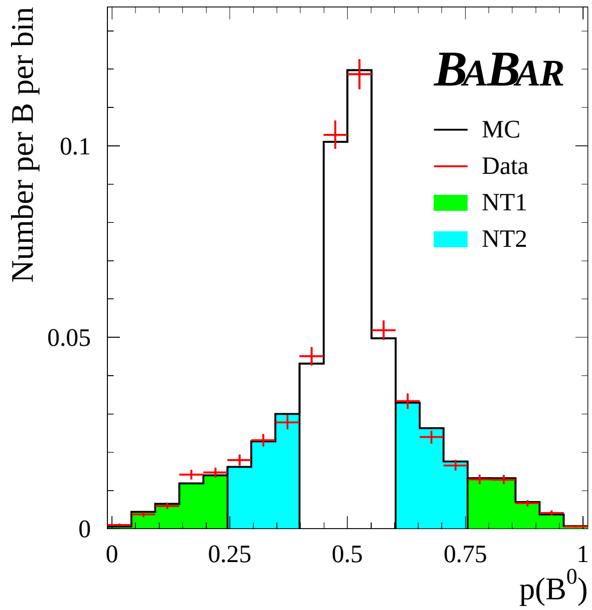

Figure 6.1: Neural net output

6.2.2 The Mistag Fraction and Tagging Efficiency

The tagging performance can be measured using the B_{flav} sample (Appendix A), i.e. fully reconstructed Bs of known flavour. Since the flavour of one B is determined very accurately, any dilution in the mixed and unmixed amplitudes arises purely from the tagging. The B_{flav} sample is large enough to determine mistag fractions for each tagging category individually. This study can also be split into B^0 and $\overline{B}^0$ to catch any possible difference in mistag rates between the two flavours (for example, kaon ID may be more accurate for K^+ than K^-). Also, extracting the tagging efficiency from this large, pure sample of Bs is trivial. Hence the efficiency, mistag fraction and difference in mistag fraction between B^0 and $\overline{B}^0$ can all be estimated.

It is vital that this information is retrieved - as the fraction of wrong tags increases, the result becomes more and more diluted with events with the opposite asymmetry, and the naive value of $\sin(2\beta)$ becomes smaller and smaller. However, if the dilution ($D = 1 - 2w$) can be measured, then it can simply be multiplied with the naive value of $\sin(2\beta)$ to give the unbiased value.

	$\epsilon(\%)$	$\omega(\%)$	$\Delta\omega(\%)$	$Q(\%)$
Lepton	10.9 ± 0.3	8.9 ± 1.3	0.9 ± 2.2	7.4 ± 0.5
Kaon	35.8 ± 0.5	17.6 ± 1.0	-1.9 ± 1.5	15.0 ± 0.9
NT1	7.8 ± 0.3	22.0 ± 2.1	5.6 ± 3.2	2.5 ± 0.4
NT2	13.8 ± 0.3	35.1 ± 1.9	-5.9 ± 2.7	1.2 ± 0.3
All	68.4 ± 0.7	-	-	26.1 ± 1.2

Table 6.3: Tagging performance

	B^0	$\overline{B}^0$	Total
Lepton	3	7	10
Kaon	19	18	37
NT1	1	2	3
NT2	10	4	14
Total Tagged	33	31	64
No Tag	N/A	N/A	47
Tagging $\epsilon(\%)$	N/A	N/A	57.7 ± 4.7

Table 6.4: Results of tagging

Although this information could be retrieved from an entirely separate study, using only the B_{flav} sample, instead it is obtained from the combined B_{flav}+B_{CP} fit described in section 6.3. Table 6.3 shows the efficiency (ϵ), wrong tag fraction (ω), difference ($B^0 - \overline{B}^0$) in mistag fraction ($\Delta\omega$) and quality $Q = \epsilon(1 - 2\omega)^2$ recovered from this fit.

Figure 6.2 shows the efficiency vs mistag fraction for each of the tagging methods.

6.2.3 Results of Tagging

The number of tagged events (in the signal box) in each category is shown in table 6.4.

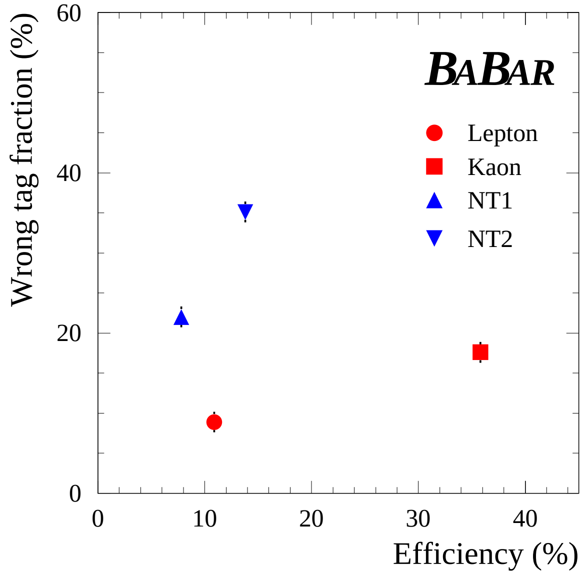

Figure 6.2: Efficiency vs mistag fraction for each of the tagging methods

6.3 Vertexing

Finding the position of the vertex of the CP (or flavour) B is relatively straightforward - the tracks used to reconstruct the J/ψ candidate give an easily identified vertex, with a resolution of $\sim 70\mu m$. However, it is also necessary to reconstruct the vertex of the other, or "tagging" B.

The tagging vertex is reconstructed by fitting a common vertex to all tracks that do not belong to the fully reconstructed B (B_{CP} or B_{flav}). When a K_s^0 or Λ candidate is reconstructed, it is used instead of its daughter tracks. γ conversions are also reconstructed and excluded from the fit.

Charm decays are a potential source of bias to the fit. To reduce this effect, any track which contributes a χ^2 of more than 6 is removed, and the fit repeated. This continues until no track contributes more than 6 to the χ^2. In addition, the centre of mass four momentum of the tagging B is known from the momentum of the reconstructed B, and can be used with the beam spot to define a pseudo-trajectory. The tracks are required to be compatible with this pseudo-trajectory. In addition, the tracks that make up the tagging B are required to be consistent with the beam spot, within errors that include the lifetime of the B.

Once the two vertices have been reconstructed, Δt (the time interval between the two decays) is determined from the Δz measurement. A correction is applied to every event according to the direction of the B in the $\Upsilon(4S)$ frame. Candidates are only accepted if the fits to both the tagging and fully reconstructed Bs converge, if the error in Δz is less than $400\mu m$ and the measured $|\Delta z|$ is less than 3mm.

The error on Δt is, at might be expected, entirely dominated by the tagging vertex resolution. This is the justification behind the implicit assumption that measurements of Δt from the CP sample have the same resolution as those from the B_{flav} sample. $\sigma_{\Delta t}$ is worked out event by event from the χ^2 of the vertex fits. It is used in the resolution function (see Section 6.4), along with a scaling factors (free parameters of the fit) to give both the resolutions and offsets[1] of the Gaussians.

The resolution functions were found to differ between "Run 1" and "Run 2" data. Figure 6.3 shows the two signal resolution functions for the two different periods. As a result, two different resolution functions were used for the two data periods. Their parameters were allowed to vary independently in the fit.

6.4 $\sin 2\beta$ Fit Method

From equations 2.44 and 2.78, it can be seen that if $|\lambda| = 1$ the decay distributions of B^0 and $\overline{B}^0$ to $J/\psi K_S^0$ are:

$$f_{\pm}(\Delta t_{true}) = \Gamma \frac{e^{-\Gamma|\Delta t_{true}|}}{4} \left\{1 \pm \sin 2\beta \sin(\Delta m_d \Delta t_{true})\right\} \tag{6.1}$$

where $\pm$ represents B^0 and $\overline{B}^0$tags, respectively. This corresponds to the decay distributions shown in figure 6.4. To take into account the possibility

[1]The resolution functions are found to have a slight bias away from zero which is correlated with the event by event error (seen in MC and verified with the B_{flav} sample. It is attributed to the presence of secondary (D) decay tracks in the tagging vertex - they induce an average displacement and larger errors.

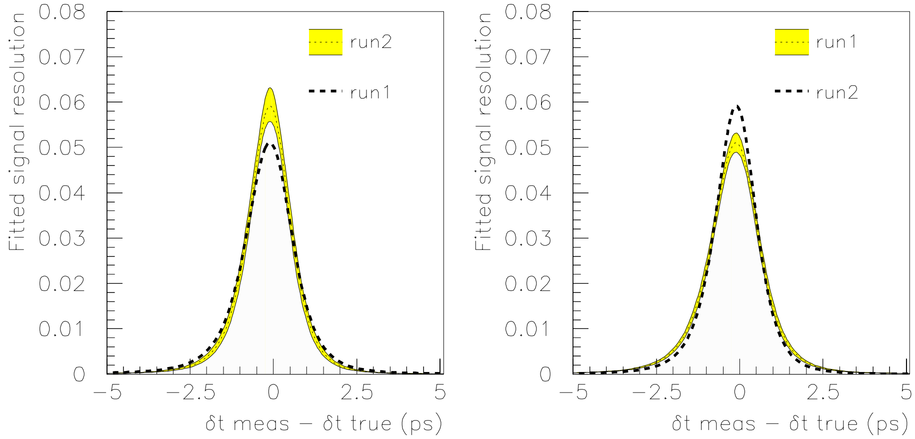

Figure 6.3: Resolution functions, Run1 and Run2

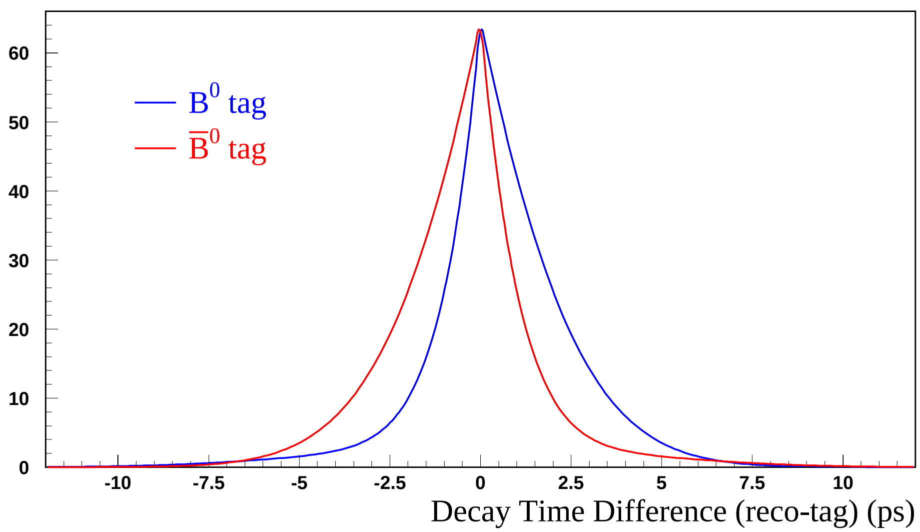

Figure 6.4: Decay distributions for B^0 and $\overline{B^0}$ ($\sin 2\beta$ =0.7)

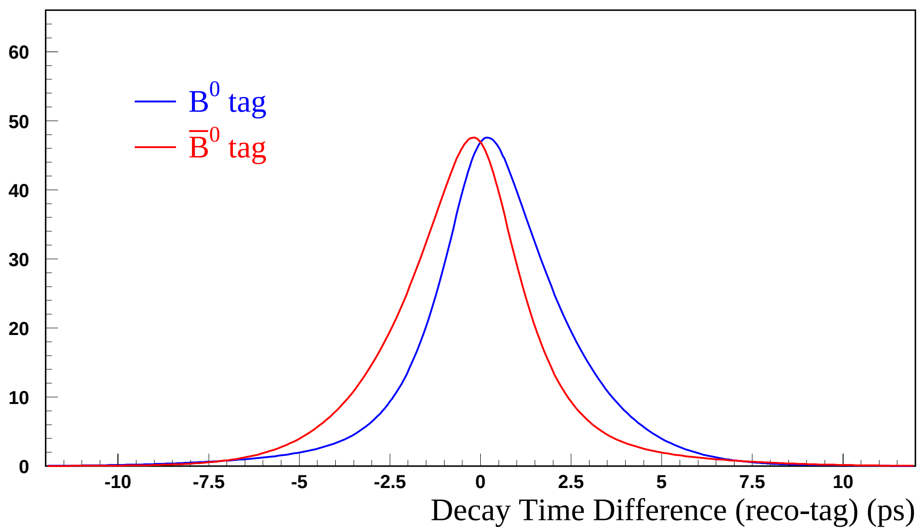

Figure 6.5: Decay distributions for B^0 and $\overline{B^0}$ with finite wrong tag probability and resolution. ($\sin 2\beta$ =0.7)

of wrong tags $\mathcal{D} = 1 - 2\omega$, the dilution, must be introduced. Also, detector resolution is finite, so $f_{\pm}$ must be convoluted with a time resolution function $\mathcal{R}(\delta_t = \Delta t - \Delta t_{true}; \widehat{a})$:

$$\mathcal{F}_{sig\pm}(\Delta t; \Gamma, \Delta m_d, \omega, \sin 2\beta, \widehat{a}) = f_{\pm}(\Delta t; \Gamma, \Delta m_d, \omega, \sin 2\beta) \otimes \mathcal{R}(\delta_t; \widehat{a}) \quad (6.2)$$

where $\widehat{a}$ represents the set of parameters describing the resolution function. The decays distributions then appear as in Figure 6.5. The value of $\sin 2\beta$ can then be extracted by maximising the likelihood function:

$$\begin{aligned} \ln \mathcal{L}_{CP} = & \sum_{B^0 tag} \ln \mathcal{F}_{sig+}(\Delta t; \Delta m_d, \widehat{a}, \omega, \sin 2\beta) \\ & + \sum_{\overline{B^0} tag} \ln \mathcal{F}_{sig-}(\Delta t; \Delta m_d, \widehat{a}, \omega, \sin 2\beta) \end{aligned} \quad (6.3)$$

This is the method used to extract $\sin 2\beta$ in this analysis, although it is complicated by having several different tagging categories, each with its own mistag fraction, and additional terms to account for backgrounds and their time dependence.

sin2β can be extracted from an unbinned maximum likelihood fit to $\mathcal{L}_{CP}$ but $\widehat{a}$ and ω are needed as inputs for the measurement. These can be determined from the B_{flav} sample, described in Appendix A. In an analogous way to the B_{CP} events,

$$\mathcal{H}_{sig\pm}(\Delta t;\Gamma,\Delta m_d,\omega,\widehat{a}) = h_{\pm}(\Delta t;\Gamma,\Delta m_d,\omega)\otimes\mathcal{R}(\delta_t;\widehat{a}) \tag{6.4}$$

where $h_{\pm}(\Delta t_{true}) = \Gamma\frac{e^{-\Gamma|\Delta t_{true}|}}{4}\{1\pm\mathcal{D}\cos(\Delta m_B \Delta t_{true})\}$. Minimising

$$\begin{aligned}\ln\mathcal{L}_{mix} = &\sum_{unmixed}\ln\mathcal{H}_{sig+}(\Delta t;\Delta m_d,\widehat{a},\omega)\\ &+\sum_{mixed}\ln\mathcal{H}_{sig-}(\Delta t;\Delta m_d,\widehat{a},\omega)\end{aligned} \tag{6.5}$$

(where a mixed event is one in which the reconstructed Bs flavour equals that of the tagging B) allows the simultaneous extraction of ω, the resolution parameters $\widehat{a}$ and the the mixing rate Δm_d (when this fit is used for this analysis, however, Δm_d is fixed to the PDG value). In order to properly incorporate the correlations between these parameters and sin2β, the fit is performed simultaneously on both samples, to maximise the sum $\ln\mathcal{L}_{CP} + \ln\mathcal{L}_{mix}$.

6.4.1 The Resolution Function

Three Gaussians are used to describe the signal resolution function - core, tail, and outlier:

$$\begin{aligned}\mathcal{R}(\delta_t;\widehat{a}) = &\sum_{k=1}^{2}\frac{f_{core,tail}}{\sigma_{core,tail\sqrt{2\pi}}}\exp\left(-\frac{(\delta_t-\delta_{core,tail})^2}{2\sigma_{core,tail}}\right)\\ &+\frac{f_{outlier}}{\sigma_{outlier}\sqrt{2\pi}}\exp\left(-\frac{\delta_t^2}{2\sigma_{outlier^2}}\right)\end{aligned} \tag{6.6}$$

The core Gaussian has a width of the error on Δt (measured event by event) multiplied by a scale factor (a free parameter of the fit) while the outlier Gaussian has its scale factor fixed to 8, and the tail Gaussian to 3. The outlier Gaussian is centred at zero.

Separate resolution functions are used for Run 1 and Run 2, both for signal and background contributions. The resolutions are found to be 2σ different between the two periods.

The resolution function is assumed be the same for the *CP* data and the B_{flav} data, but differences between the signal and background contributions are allowed for in the systematic.

6.4.2 Background Modeling

The *CP* Sample

To account for background events, it is necessary to modify equations 6.2 and 6.4 by changing the definitions of $\mathcal{F}_{\pm}$ and $\mathcal{H}_{\pm}$ to include descriptions of background events. With this addition,

$$\begin{aligned} \mathcal{F}_{\pm} =& f_{sig}^{CP}\mathcal{F}_{sig\pm}(\Delta t;\Gamma,\Delta m_d,\omega,\sin 2\beta,\widehat{a}) \\ &+f_{peak}^{CP}\mathcal{B}_{\pm,peak}^{CP}(\Delta t;\widehat{a}) \\ &+f_{cont}^{CP}\sum_{\beta=bkgd}\mathcal{B}_{\pm,\beta}^{CP}(\Delta t;\widehat{b}) \end{aligned} \tag{6.7}$$

Here, the types of background considered are "signal like", with the PDF $\mathcal{B}_{\pm peak}$, and potentially several different types of "continuum like" background, with PDFs $\mathcal{B}_{\pm,\beta}^{CP}(\Delta t;\widehat{b})$. It is worth noting here that "signal like" background uses the same resolution function as real signal ($\widehat{a}$). The "continuum like" backgrounds use a separate resolution function ($\widehat{b}$). These two background PDFs provide an empirical description of the Δt distribution of the background events in the sample. They are normalised such that $\int_{-\infty}^{\infty} d\Delta t(\mathcal{B}_{+}+\mathcal{B}_{-})=1$.

In equation 6.7 the probability of an event being signal or background is given by $f_{sig}^{CP}, f_{peak}^{CP}$ and f_{cont}^{CP}. As shown in chapter 5, the $m_{\rm ES}$ distribution of these events can be described by an Argus + Gaussian fit. Taking the parameters from this fit, if the Gaussian is described by $\mathcal{G}(m_{\rm ES})$ and the Argus function by $\mathcal{A}(m_{\rm ES})$ then the probability of an event of given $m_{\rm ES}$ being signal or "signal like" background is

$$f_{sig}^{CP} + f_{peak}^{CP} = \frac{\mathcal{G}(m_{\mathrm{ES}})}{\mathcal{G}(m_{\mathrm{ES}}) + \mathcal{A}(m_{\mathrm{ES}})}, \tag{6.8}$$

and the probability of continuum like background is

$$f_{cont}^{CP} = \frac{\mathcal{A}(m_{\mathrm{ES}})}{\mathcal{G}(m_{\mathrm{ES}}) + \mathcal{A}(m_{\mathrm{ES}})}. \tag{6.9}$$

The fraction of the Gaussian peak made up of "signal like" background, δ_{peak}, is determined from Monte Carlo, so

$$f_{sig}^{CP} = \frac{(1-\delta_{peak})\mathcal{G}(m_{\mathrm{ES}})}{\mathcal{G}(m_{\mathrm{ES}}) + \mathcal{A}(m_{\mathrm{ES}})} \tag{6.10}$$

$$f_{peak}^{CP} = \frac{\delta_{peak}\mathcal{G}(m_{\mathrm{ES}})}{\mathcal{G}(m_{\mathrm{ES}}) + \mathcal{A}(m_{\mathrm{ES}})} \tag{6.11}$$

In order to determine the parameters of the background, all events in the "signal ΔE" region with m_{ES} above $5.2GeV$ are used in the fit. Essentially all events bellow $5.27GeV$ are "continuum like" background, and in this region $f_{sig}^{CP} + f_{peak}^{CP} \simeq 0$ and $f_{cont}^{CP} = 1$.

Rather than attempting to determine the sources of background, they are dealt with empirically in the likelihood fit, allowing for various time dependencies. "Continuum like" events are allowed two possible time dependencies: they can either be prompt or have a finite lifetime, corresponding to PDFs of

$$\mathcal{B}_{\pm,\beta=1}^{CP} = (1/2)\delta(\Delta t_{true}) \otimes \mathcal{R}(\delta_t;\widehat{b}) \tag{6.12}$$

$$\mathcal{B}_{\pm,\beta=2}^{CP} = (\Gamma_{\beta=2}^{CP}/4)(1 \pm \mathcal{D}_{\beta=2}^{CP} \sin\Delta m_d \Delta t_{true})e^{-\Gamma_{\beta=2}^{CP}|\Delta t_{true}|} \otimes \mathcal{R}(\delta_t;\widehat{b}) \tag{6.13}$$

The "signal like" background is also allowed a finite lifetime,

$$\mathcal{B}_{\pm peak}^{CP} = (\Gamma_{peak}^{CP}/4)(1 \pm \mathcal{D}_{peak}^{CP} \sin\Delta m_d \Delta t_{true})e^{-\Gamma_{peak}^{CP}|\Delta t_{true}|} \otimes \mathcal{R}(\delta_t;\widehat{a}) \tag{6.14}$$

The lifetimes and dilutions here have no physical meaning. They are simply free parameters, allowed to assume the values that best describe the data.

The B_{flav} Sample

The background parameterisation of the B_{flav} sample is almost identical to that of the *CP* sample. The signal PDF must again be replaced with one describing both signal and background:

$$\begin{aligned}\mathcal{H}_{\pm} =& f_{sig}^{flav}\mathcal{H}_{sig\pm}(\Delta t;\Gamma,\Delta m_d,\widehat{a}) \\ &+ f_{peak}^{flav}\mathcal{B}_{\pm,peak}^{flav}(\Delta t;\widehat{a}) \\ &+ f_{cont}^{flav}\sum_{\beta=bkgd}\mathcal{B}_{\pm,\beta}^{flav}(\Delta t;\widehat{b})\end{aligned} \tag{6.15}$$

where the fs are determined from Argus+Gaussian fits, as before. The "signal like" background is described by the PDF

$$\mathcal{B}_{\pm peak}^{flav} = (\Gamma_{peak}^{flav}/4)(1\pm\mathcal{D}_{peak}^{flav}\cos\Delta m_{peak}\Delta t_{true})e^{-\Gamma_{peak}^{flav}|\Delta t_{true}|}\otimes\mathcal{R}(\delta_t;\widehat{a}) \tag{6.16}$$

where $\widehat{a}$ is the same resolution function used for the *CP* sample, but Γ and $\mathcal{D}$ are independent. The mixing parameter δm_{peak} is an additional free parameter, allowed to take the value that best fits the data. In the B_{flav} sample, there are assumed to be three types of "continuum like" backgrounds - prompt, finite lifetime and mixing backgrounds[1]. These have the PDFs:

$$\mathcal{B}_{\pm\beta=1}^{flav} = (1\pm\mathcal{D}_{\beta=1}^{flav})\delta(\Delta t_{true})\otimes\mathcal{R}(\delta_t;\widehat{b}) \tag{6.17}$$

$$\mathcal{B}_{\pm\beta=2}^{flav} = (1\pm\mathcal{D}_{\beta=2}^{flav})e^{-\Gamma_{\beta=2}^{flav}|\Delta t_{true}|}\otimes\mathcal{R}(\delta_t;\widehat{b}) \tag{6.18}$$

$$\mathcal{B}_{\pm\beta=3}^{flav} = (\Gamma_{\beta=3}^{flav}/4)(1\pm\mathcal{D}_{\beta=3}^{flav}\cos\Delta m_{\beta=3}\Delta t_{true})e^{-\Gamma_{\beta=3}^{flav}|\Delta t_{true}|}\otimes\mathcal{R}(\delta_t;\widehat{b}) \tag{6.19}$$

with $\widehat{b}$ here the same background resolution function as for the *CP* sample.

6.4.3 Separation of Tagging Categories

So far, for simplicity only a single tagging category has been assumed. However, there are four different tagging categories, all with potentially different

[1]In the fit to determine the value of sin2β, no mixing background is allowed - its fraction is set to zero. This term is only included for a systematic study (see Section 6.5.2)

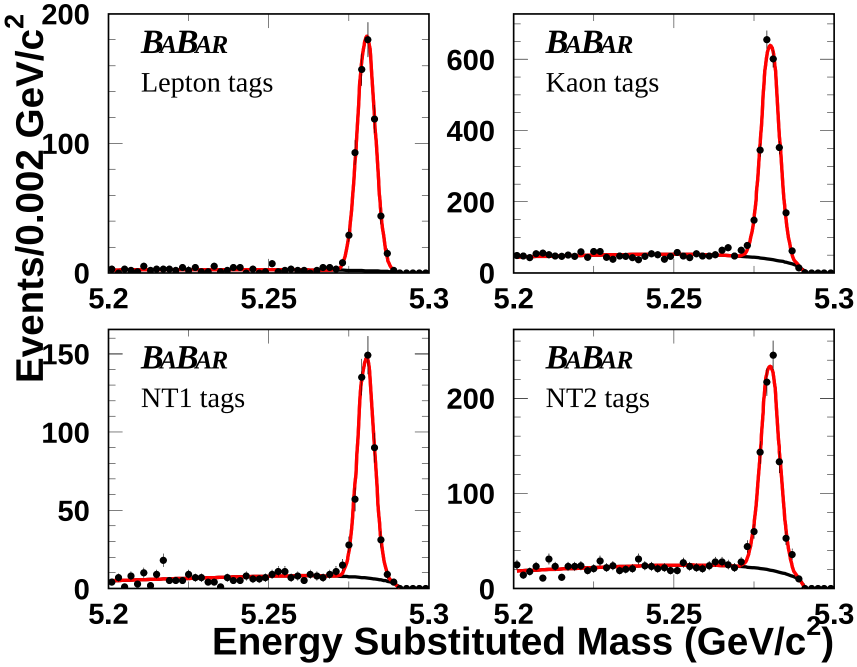

Figure 6.6: $m_{\rm ES}$ of events in different tagging categories (B_{flav} sample).

dilutions, resolutions and backgrounds. Therefore, the full PDF contains four terms for each one described above. Some of the parameters described may vary between tagging categories: some are kept identical. The details of the fit parameters are described in Section 6.4.5, below. Also, the background fractions f are worked out separately for each tagging category. Fig 6.6 shows the dependence of the purity on the tagging category. Tagging works as an extra cut against continuum background, particularly in the case of the primary lepton tag.

6.4.4 Inputs to the Fit

- $\Delta m_d : 0.472 \pm 0.017 ps^{-1}$
- $\tau_{B^0} : 1.548 \pm 0.032 ps$

The values of Δm_d and τ_{B^0} are taken from [12], their uncertainties are accounted for in the systematic error.

6.4.5 Free parameters in the fit

There are 45 free parameters:

Signal contribution dilutions

In each of the four tagging categories, an average (B^0 and $\overline{B}^0$) dilution and a $\Delta D \equiv D(B^0) - D(\overline{B}^0)$ are allowed to float in the fit. The signal dilutions are constrained to be between 0 and 1.

Mixing background dilutions

Two background dilutions are allowed per tagging category. There is a prompt ($\tau = 0$) fit contribution and a finite lifetime contribution.

Resolution function

Eight parameters for signal contributions are allowed to float, all of which may take different values in run1 and run2:

- Core scale factors (1 parameters).
- One core bias scaling factor per tagging category (4 parameters).
- Tail bias scaling factor (1 parameter).
- Fraction of events in tail and outlier Gaussians (2 parameters).

Two Gaussians are used to model the background resolution function. Three parameters are free, all of which may take different values in run1 and run2:

- Core scale factor
- Core bias scaling factor (same for all tagging categories)
- Fraction of outliers

There is no allowance for a tail Gaussian contribution,

The fraction of each of the Gaussians is constrained to be between 0 and 1 for the signal and background resolution functions.

Tag category	Dilution
Lepton	0.912
Kaon	0.762
NT1	0.562
NT2	0.264

Table 6.5: $B^{\pm}$ dilutions used for peaking background in B_{flav} sample

Background contribution in the mixing sample

The fraction of $\tau = 0$ background and the lifetime of the $\tau > 0$ background is determined in the full likelihood fit. The lifetime for the $\tau > 0$ background is a free parameter, but is assumed to be the same for all tagging categories. It is assumed that none of the background mixes, but the possibility that it does is accounted for in the systematic error (see section 6.5.2)

There is also a small contribution from "signal like" background, from $B^{\pm}$ decays. Table 6.5 shows the dilutions used for this fit contribution. B^0 decays also contribute "signal like" background, however its properties are identical to that of signal, and so it is used as such (background here means only that its decay mode was not identified correctly).

The resolution function used for the peaking background is the same one used for signal events.

Background contribution to the CP sample

The "Continuum like" background contribution is assumed to have either $\tau = 0$ or the B^0 lifetime. The fraction with $\tau = 0$ is left free, but is fixed across tagging categories. The "Signal like" background is assumed to have the B^0 lifetime, and the resolution function and dilutions of the signal are used. The *CP* of the background with the B^0 lifetime is fixed to 0, but the possibility of a non-zero *CP* is accounted for in the systematic error (see section 6.5.2).

6.4.6 Summary of parameters

- sin2β

- 4 signal dilutions
- ΔD for 4 signal categories
- 8 parameters in the signal resolution function ($\times 2$, separate for run1 and run2)
- 8 background dilutions
- 3 parameters in the background resolution function ($\times 2$, separate for run1 and run2)
- Fraction of prompt CP background (1 parameter)
- Lifetime and fractions of B_{flav} background (5 parameters)

Which gives a total of 45 free parameters.

The program used to perform this procedure is tFit [29].

6.5 Systematics

This section describes the techniques used to determine each part of the error, and cross-checks done do verify the estimations.

6.5.1 Signal Parameters

Implicit in this analysis is the assumption that the resolution function and the dilutions are the same in the B_{flav} and CP samples. Differences between the two are accounted for in the systematic error. The systematics are summarised in table 6.6.

Dilutions

Dilutions are extracted from large samples of B_{flav} and CP Monte Carlo, and compared. The sin2β fit is repeated, with the dilutions fixed to the MC_{CP} and then the $MC_{B_{flav}}$ values, and the difference in sin2β is assigned as the systematic error.

Source	Contribution to error
Δt signal resolution	± 0.005
Δt signal resolution outliers	± 0.003
Resolution difference between right and wrong tag	± 0.020
signal dilutions	± 0.046
Δt resolution model	± 0.015

Table 6.6: Contribution to Systematic Error from Signal Parameters

Resolution function parameters

Resolution functions are extracted from large samples of B_{flav} and CP Monte Carlo, and compared. The difference in sin2β using the two sets of resolution function parameters is used as the systematic error.

This is then cross-checked in data. The parameters are extracted from a fit with fixed lifetime to all neutral and charged Charmonium events (giving a sample of $\sim$ 3000 events). When a sin2β fit is performed using these parameters for the resolution function, the observed difference to the fit using B_{flav} derived parameters shows excellent agreement to the MC study.

To check that the fitting procedure returns an appropriate resolution function, fits are performed on signal MC, both floating the resolution function parameters and fixing them to values extracted using MC truth information. The difference between the two is 0.005 ± 0.004. Since this statistical error is already included in the MC statistics error (see Section 6.5.5), no systematic error is quoted.

Resolution Difference Between Right and Wrong Tag

To determine the systematic from this effect, a sample of MC events is split into "wrong tags" and "right tags". A fit to sin2β and the resolution function parameters is performed on the two subsamples, and on all events together. The dilutions are fixed to -1 and 1 in the wrong and right tags respectively, while they are fixed to the MC truth value in the fit to all the MC. When the weighted average of the "wrong" and "right tag" fits is compared to the fit to all the MC events, the difference is taken as the systematic error.

Outlier Δt signal resolution

To evaluate this systematic, the outlier contribution to the resolution function is varied. The width of the outlier Gaussian is varied between 4 and 12 ps, and its bias is varied between -2ps and +2ps. The change is taken as the systematic. In addition, to evaluate the effect on the systematic error of the assumption that the outliers follow a Gaussian distribution, it is instead fitted with a PDF flat in Δt within the accepted region of $-17 < \Delta t < 17ps$.

Signal resolution model

The systematic error brought in by the assumption of a triple Gaussian resolution model is evaluated by replacing it with a Gaussian + Exponential model. An explicit outlier term is added after convolution with the decay model. The triple Gaussian resolution model and 3 different free parameter versions of the G+Exp model were tried:

1. A single lifetime and Gaussian fraction parameter
2. Separate life time parameters per tagging category
3. Separate Gaussian fraction parameters per tagging category.

sin2β fits are performed on a high statistics full MC sample, using the G+Exp and default models. The largest difference is between the standard triple Gaussian model and 3., and this is taken as the systematic.

6.5.2 Background parameters

Background parameters are extracted either from a fit to the data (Argus + Gaussian) which identifies signal and background events, or from MC. In this section, a number of variations are considered and the corresponding changes in sin2β are taken as systematic errors. They are summarised in table 6.7.

Signal purity

The effect of uncertainty in the signal purity on sin2β is estimated by varying it by one sigma around its measured value (from an Argus+Gaussian fit) and

Source	Contribution to error
Signal purity:CP sample	± 0.024
Signal purity:B_{flav} sample	± 0.002
M_{ES} endpoint	± 0.002
CP background peaking componet	± 0.007
CP background CP content (Argus)	± 0.060
CP background CP content (Peak)	± 0.007
CP background τ	± 0.021
CP background resolution	± 0.029
B_{flav} background mixing contribution	± 0.002
B_{flav} background peaking contribution	± 0.004

Table 6.7: Contribution to Systematic Error from Background Parameters

observing the effect on the sin2β measurement. This is carried out both for the CP events and the B_{flav} sample.

An error in m_{ES} fit results from uncertainty in the beam energy is also possible. This is accounted for by varying the end point of the Argus background shape by $\pm 2MeV$ around the standard value of 5.291 GeV. (Events with greater B mass are excluded from the global likelihood fit). At $-2MeV$ 21 candidates are excluded from the hadronic decay modes, and none from the CP sample.

CP background peaking component

Background contributions that peak in m_{ES} are estimated by running on the inclusive J/ψ Monte Carlo. A systematic error on sin2β is assigned using the change in sin2β results when this background is varied by 1σ around the central values (taking into account the uncertainty on the branching fractions as well as Monte Carlo statistics).

CP content of background

The assumed CP of the "Continuum like" background contribution is changed from 0 to ± 1. The CP of the peaking component is varied in the same way.

Source	Contribution to error
B^0 Lifetime	± 0.013
Δm_d	± 0.015
z scale + boost	± 0.005
Beam spot	± 0.003
SVT alignment	± 0.046
Monte Carlo Statistics	± 0.020

Table 6.8: Contribution to Systematic Error from External Parameters, Detector Effects and Monte Carlo.

Half the total (-1 to +1) difference is taken as the systematic.

Lifetime and resolution function for *CP* background

The first of these systematics was estimated by varying the lifetime of *CP* background from 0.7 to 2.5ps and taking the change in the value of sin2β as the error contribution. The resolution function of the background for the *CP* sample is by default taken from the B_{flav} background. The shift in sin2β when the signal resolution function is used instead is taken as the systematic error introduced by this assumption.

Mixing contribution to the B_{flav} background

In the fit , the $\tau > 0$ background in the B_{flav} sample is assumed to not mix. As a systematic check, a fit is performed where it is allowed to mix. The shift in sin2β is taken as the systematic error.

Peaking background in the B_{flav} background

The peaking background in the B_{flav} sample is found to be $(1.5 \pm 1.0)\%$, from Monte Carlo. This uncertainty gives a systematic error on sin2β of ± 0.004

6.5.3 External parameters

The B^0 lifetime and Δm_d are varied according to PDG 2000. The slope for the change in $\sin2\beta$ with respect to these parameters is:

$\frac{d\sin2\beta}{d\Delta m_d} = -0.9ps$

$\frac{d\sin2\beta}{d\tau_{B^0}} = -0.41ps^{-1}$

The systematics are shown in table 6.8.

6.5.4 Detector effects

The possibility of forms of mis-reconstruction of the data that might not be properly accounted by the measurement technique has been explored. The possible effects considered (and summarised in table 6.8) are:

Uncertainty on Boost and *z* scale

In order to evaluate a possible effect from the uncertainty on the boost and z-scale, the measurement of Δt has been scaled by $\pm0.6\%$[1] upwards and downwards in full MC, and the effect on the measured value of $\sin2\beta$ taken as the systematic.

SVT misalignment

The effect of a possible local misalignment has been studied by reconstructing the same sample of Monte Carlo (with $\sin2\beta$ =0.7) events with different sets of alignment constants. Miss-alignments significantly worse than the actual, measured alignment were simulated. The effects on the value of $\sin2\beta$ were taken as the systematic.

[1]This limit is taken from extensive studies of the SVT before and after installation, measurement of the position of modules using high momentum charged tracks and by comparing the known positions of mechanical features at the end of the beampipe with their apparent positions measured by charged tracks passing throught the SVT. Beam energy is constsntly monitored, and its uncertainty is 0.1%.

6.5.5 Monte Carlo correction

A set of high statistics full MC studies on *CP* signal events has been performed in order to evaluate possible biases in the measurement. The mean pull is consistent with 0, so no correction is applied and a systematic error, based on the statistics of the Monte Carlo, is included in the total error (and shown in table 6.8).

6.6 Results

The output of the fit is $\sin 2\beta = 0.76 \pm 0.52 \pm 0.12$[1].This is shown as the solid line in figure 6.7, while the data points are the raw asymmetry divided by the average dilution. The Log Likelihood, plotted as a function of $\sin 2\beta$, is shown in figure 6.8. The output values of the other 44 free parameters of the fit are included in Appendix B.

[1]For a maximum likelihood fit such as this the statistical error is not necessarily symmetrical around the central value. In this case it is $+0.516, -0.523$ symmetrical to the quoted accuracy.

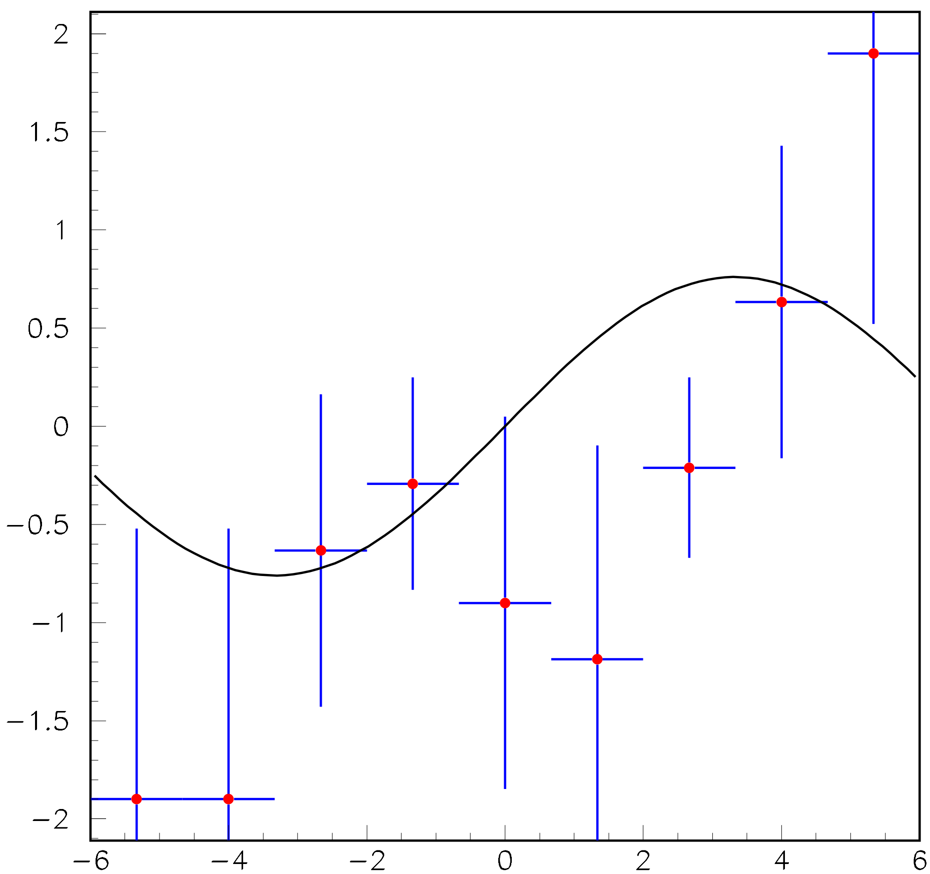

Figure 6.7: Raw, binned asymmetry scaled by average dilution factor, with unbinned maximum likelihood fit result ($\sin 2\beta = 0.76 \pm 0.52 \pm 0.12$) as solid line ($J/\psi K_S^0, K_S^0 \to \pi^0\pi^0$)

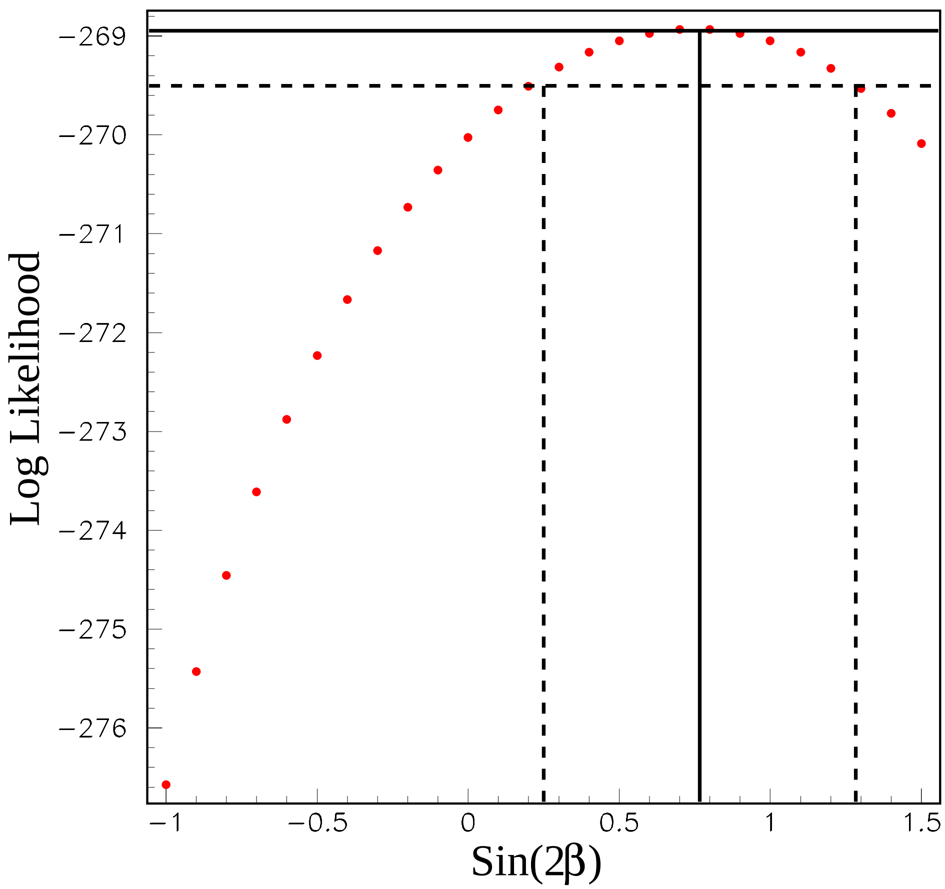

Figure 6.8: Log Likelihood as a function of sin2β. Solid black line shows output value of fit, dotted lines show 1 standard deviation limit.

Chapter 7

Conclusions

7.1 Branching Ratio Measurement

7.1.1 Comparison With Other Measurements

In Chapter 4, $BR(B^0 \to J/\psi K^0)$ was measured to be $(9.6 \pm 1.5_{stat} \pm 0.7_{syst}) \times 10^{-4}$ using events where one of the Bs had decayed to $J/\psi K^0_S$ (with the J/ψ decaying to two leptons and the K^0_S decaying to $\pi^0\pi^0$) from data collected at the *BABAR* experiment. $BR(B^0 \to J/\psi K^0)$ has been previously measured at other experiments and is listed in [12]. $BR(B^0 \to J/\psi K^0)$ can also be measured with other decays, and these independent measurements can be used for comparison (values taken from [6]). Table 7.1 shows all the measurements of $BR(B^0 \to J/\psi K^0)$ made at *BABAR,* the PDG value, and the recent result from Belle [34].

Sample	$BR(B^0 \to J/\psi K^0) \times 10^{-4}$
$J/\psi K^0_S (K^0_S \to \pi^0\pi^0)$	$9.6 \pm 1.5_{stat} \pm 0.7_{syst}$
$J/\psi K^0_S (K^0_S \to \pi^+\pi^-)$	$8.5 \pm 0.5_{stat} \pm 0.6_{syst}$
$J/\psi K^0_L$	$6.8 \pm 0.8_{stat} \pm 0.8_{syst}$
Combined BABAR result	$8.3 \pm 0.4_{stat} \pm 0.5_{syst}$
PDG2001	9.6 ± 0.9
Belle	$7.7 \pm 0.4_{stat} \pm 0.7_{syst}$

Table 7.1: Measured values of $BR(B^0 \to J/\psi K^0)$

7.1.2 Comparison With Theory

For comparison with theory, it is useful to consider the ratio of $BR(B^0 \to J/\psi K^0)$ to $BR(B^0 \to J/\psi K^{\pm})$ and $BR(B^0 \to J/\psi K^{*0})$. These ratios are free of some of the uncertainties that enter into a full calculation of the branching fraction.

One model independent prediction can be derived from isospin symmetry, that

$$\frac{BR(B^0 \to J/\psi K^0)}{BR(B^{\pm} \to J/\psi K^{\pm})} = 1 \tag{7.1}$$

From [6], $BR(B^0 \to J/\psi K^{\pm})$ is measured to be $(10.1 \pm 0.3 \pm 0.5) \times 10^{-4}$, therefore

$$\frac{BR(B^0 \to J/\psi K^0)}{BR(B^{\pm} \to J/\psi K^{\pm})} = 0.95 \pm 0.15_{stat} \pm 0.08_{syst} \tag{7.2}$$

This shows agreement with 1 to within errors. Interestingly, if BaBar's other measurements of $BR(B^0 \to J/\psi K^0)$ used as well, this gives a value of:

$$\frac{BR(B^0 \to J/\psi K^0)}{BR(B^{\pm} \to J/\psi K^{\pm})} = 0.83 \pm 0.05_{stat} \pm 0.03_{syst} \tag{7.3}$$

which is significantly different from 1. This has been interpreted as a difference in the rates $BF(\Upsilon(4S) \to B^+B^-)$ and $BF(\Upsilon(4S) \to B^0\overline{B}^0)$.

The ratio

$$\frac{BR(B^0 \to J/\psi K^{*0})}{BR(B^0 \to J/\psi K^0)} \tag{7.4}$$

is an important input to phenemonological models of B decay [9, 10, 8]. From [6], $BR(B^0 \to J/\psi K^{*0}) = (12.4 \pm 0.5_{stat} \pm 0.9_{syst}) \times 10^{-4}$, so

$$\frac{BR(B^0 \to J/\psi K^{*0})}{BR(B^0 \to J/\psi K^0)} = 1.29 \pm 0.21_{stat} \pm 0.13_{syst} \tag{7.5}$$

.

In addition, the ratios to $B^0 \to \psi(2S)K^0$ and $B^0 \to \chi_{c1}K^0$ can be determined, using the branching fractions from [6]:

$$\frac{BR(B^0 \to \psi(2S)K^0)}{BR(B^0 \to J/\psi K^0)} = 0.72 \pm 0.16_{stat} \pm 0.12_{syst} \tag{7.6}$$

$$\frac{BR(B^0 \to \chi_{c1}K^0)}{BR(B^0 \to J/\psi K^0)} = 0.56 \pm 0.17_{stat} \pm 0.12_{syst} \tag{7.7}$$

These are also useful inputs for phenemonological models.

7.2 sin2β

7.2.1 Comparison With Other Measurements

In Chapter 5, sin2β was measured to be $0.76 \pm 0.52_{stat} \pm 0.12_{syst}$ using events where one of the Bs had decayed to $J/\psi K_S^0$ (with the J/ψ decaying to two leptons and the K_S^0 decaying to $\pi^0\pi^0$) from data collected at the $BABAR$ experiment. The first comparison that can be made is with sin2β measurements made with different CP eigenstates using the data collected at $BABAR$. Table 7.2 shows the comparison between the various modes, and the combined result (taken from [1]). It can be seen that there is good agreement between the measurement made with $J/\psi K_S^0(K_S^0 \to \pi^0\pi^0)$ and with all the other modes (other individual modes shown with statistical error only). The result can also be compared against those obtained at other experiments. Table 7.3 shows all other existing measurements of sin2β [31, 7, 32, 33].

7.2.2 Comparison With Theory

The measured value, $0.76 \pm 0.52_{stat} \pm 0.12_{syst}$, excludes a zero value of sin2β at the 1.43σ level.

Figure 7.1 shows the compatibility of the measurement with the Standard Model. The $\overline{\rho\eta}$ plane is shown, where $\overline{\rho}$ and $\overline{\eta}$ are related to ρ and η (defined

Sample	measured value of sin2β
$J/\psi K_S^0(K_S^0 \to \pi^0\pi^0)$	$0.76 \pm 0.52_{stat} \pm 0.12_{syst}$
$J/\psi K_S^0(K_S^0 \to \pi^+\pi^-)$	$0.45 \pm 0.18_{stat}$
$\psi(2S)K_S^0(K_S^0 \to \pi^+\pi^-)$	$0.47 \pm 0.42_{stat}$
$\chi_{c1}K_S^0(K_S^0 \to \pi^+\pi^-)$	$2.59 \pm 0.67_{stat}$
$J/\psi K_L^0$	$0.70 \pm 0.34_{stat}$
$J/\psi K^{*0}(K^{*0} \to K_S^0\pi^0)$	$0.82 \pm 1.00_{stat}$
All modes	$0.59 \pm 0.14_{stat} \pm 0.05_{syst}$

Table 7.2: sin2β results at *BABAR*

Experiment	measured value of sin2β
CDF	$0.79^{+0.41}_{-0.44}$
Belle	$0.99 \pm 0.14_{stat} \pm 0.06_{syst}$
ALEPH	$0.84^{+0.82_{stat}}_{-1.04} \pm 0.16_{syst}$
OPAL	$3.2^{+1.8_{stat}}_{-2.0} \pm 0.5_{syst}$

Table 7.3: Comparison with other experiments

in Section 2.4.3) by $\overline{\rho} = \rho(1 - \lambda^2/2)$ and $\overline{\eta} = \eta(1 - \lambda^2/2)$[1]. The dotted lines represent the central value.

The upper error extends into an unphysical region (sin2$\beta > 1.$), and the multiple possible solutions for β mean that all of $\overline{\rho} < 1, \overline{\eta} > 0$ and $\overline{\rho} > 1, \overline{\eta} < 0$ cannot be excluded at the 1σ level. The black, hatched regions are excluded at the 3σ level.

Figure 7.1 was created using the CKMFitter software package [35]. The other constraints shown in this figure are those placed on $\overline{\rho}$ and $\overline{\eta}$ by measurements of other CKM parameters (in general, limits on the lengths of the sides of the unitary triangle). Appendix C includes the values used to create this plot. The red bounded region shows the limitations on the values of $\overline{\rho}$ and $\overline{\eta}$ by the Standard Model, given all the other constraints. The sin2β measurement is compatible with this.

When the $J/\psi K_S^0(K_S^0 \to \pi^0\pi^0)$ events are combined with the others pro-

[1] $\overline{\rho}$ and $\overline{\eta}$ originate from the extended Wolfenstein parameterisation, which includes terms up to $\mathcal{O}(\lambda^6)$. The difference is small. As seen in Section 2.4.3, $1 - \lambda^2/2 \sim 0.98$.

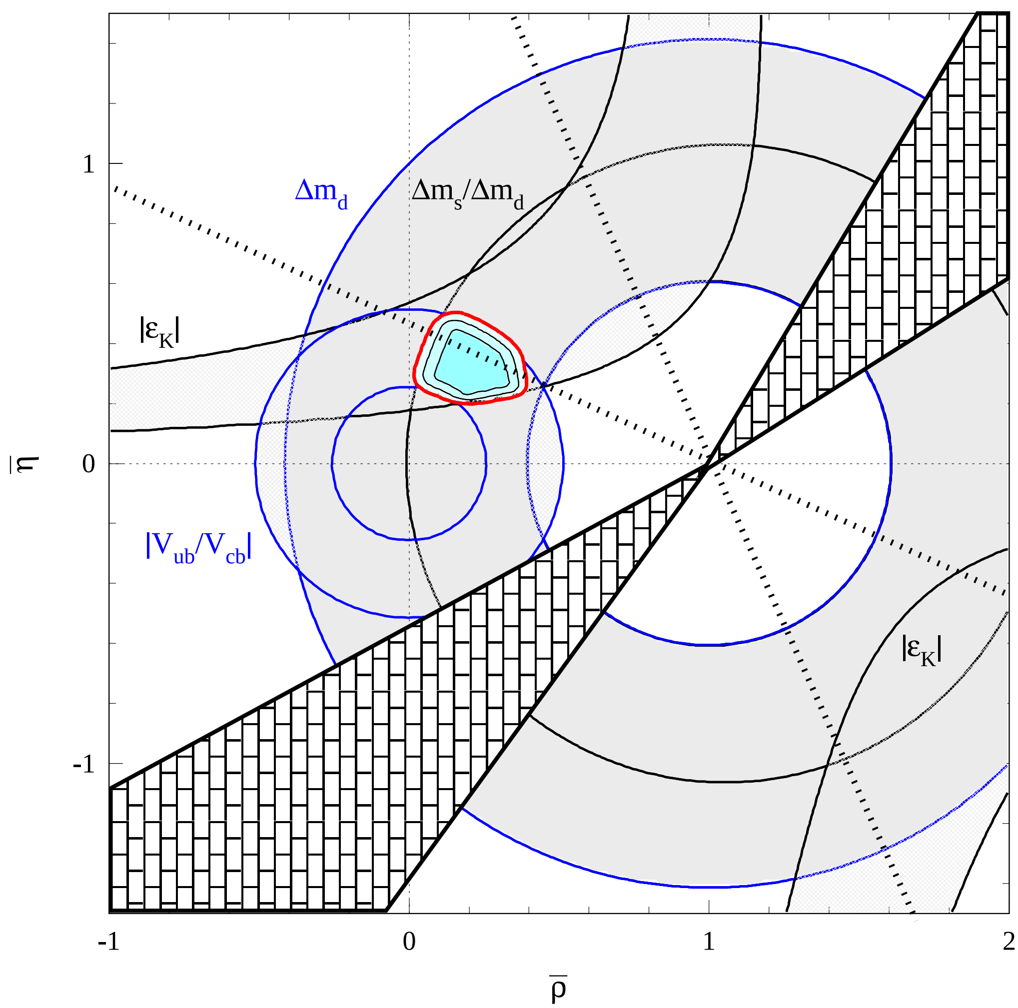

Figure 7.1: $\overline{\rho,\eta}$ Plane with constraints from measured CKM parameters shown. Straight dotted lines represent central value of sin2β measured in this thesis. Black hatched regions are excluded at the 3σ level.

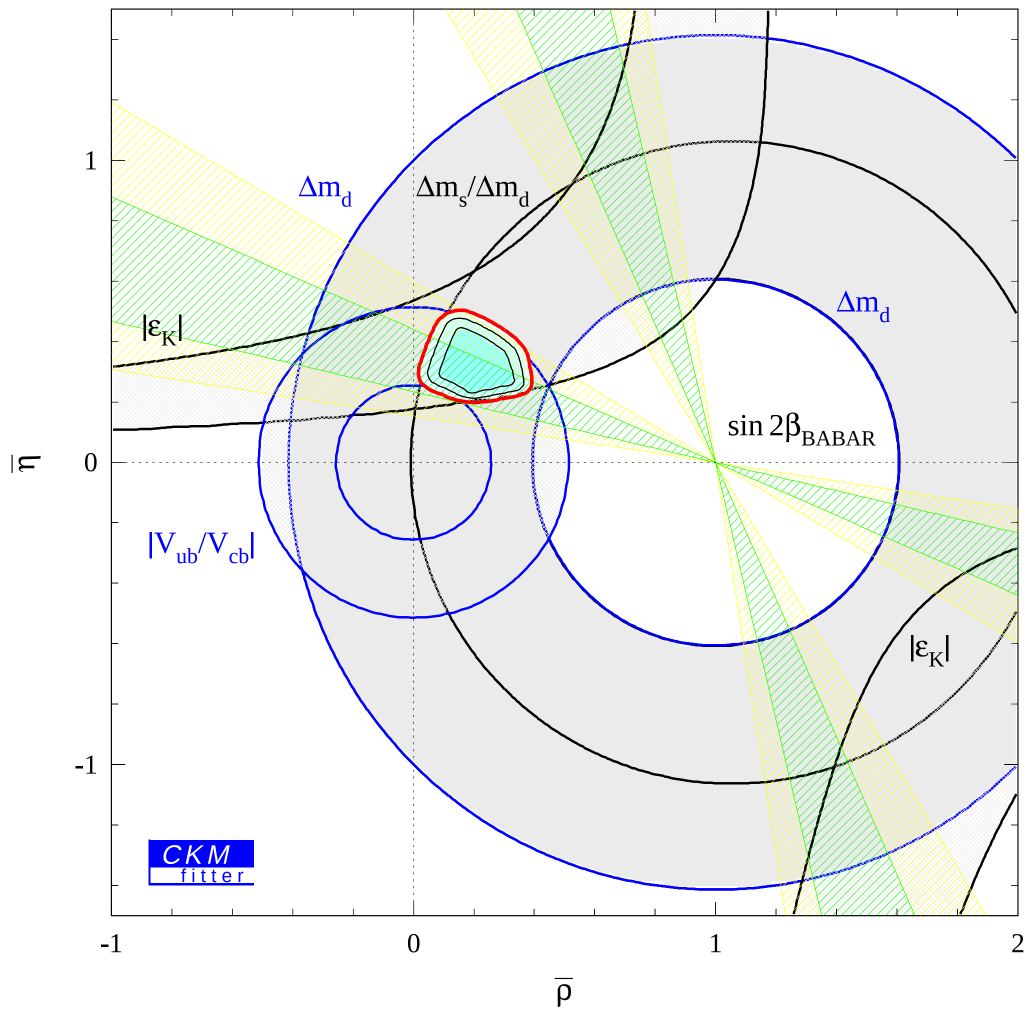

Figure 7.2: $\overline{\rho, \eta}$ Plane with constraints from measured CKM parameters shown. BaBar's sin2β result is shown (events described in this thesis are a subsample). The 2σ limit is shown in green, 3σ in yellow.

duced at BaBar, (see table 7.2), the constraints placed on the $\overline{\rho}\ \overline{\eta}$ plane are shown in Figure 7.2. The absence of CP violation in the B system is excluded at the 4.1σ level. This result was the first observation of CP violation in the B system.

Appendix A

The B_{flav} Sample

In addition to the sample of events in which one B has been reconstructed as decaying into $J/\psi K^0_S$, to perform the $\sin 2\beta$ measurement it is also necesary to have a sample of events in which one of the Bs has decayed into a state that identifies its flavour. This is known as the B_{flav} sample. It consisits of the modes $B^0 \to D^{(*)}\pi, B^0 \to D^{(*)}\rho, B^0 \to D^{(*)}a_1$ and $B^0 \to J/\psi K^{*0}(K^{*0} \to K^{\pm}\pi^{\mp})$.

In the course of this chapter some shorthand is used for compactness:

- *GoodTracksVeryLoose* must pass close to the nominal interaction point (within 1.5cm in xy and 3 cm in z). They are also required to have a transverse momentum of less that 10 GeV.

- *GoodTracksLoose* are *GoodTracksVeryLoose* that are required to provide at least 12 hits in the drift chamber. They must also have $p_T > 100 MeV/c$.

- *SMSNotAPion* are tracks that pass a loose DIRC based PID designed to reject the pion hypothesis.

A.1 $D^{0,\pm}$ reconstruction

The D^0 is reconstructed in the modes $K^{\pm}\pi^{\mp}$, $K^{\pm}\pi^{\mp}\pi^0$, $K^0_S\pi^+\pi^-$ and $K^{\pm}\pi^{\mp}\pi^{\mp}\pi^{\pm}$ and $D^{\pm}$ in the modes $K^0_S\pi^{\pm}$ and $K^{\mp}\pi^{\pm}\pi^{\pm}$. π^0 candidates are selected as described in Chapter 4, section 4.4.1. K^0_S candidates are selected as described

Mode	M_D	K/π track momentumMeV/c
$D^0 \to K^\pm\pi^\mp$	$\pm 18MeV/c^2$	<200
$D^0 \to K^\pm\pi^\mp\pi^0$	$\pm 33.5MeV/c^2$	<150
$D^0 \to K_S^0\pi^+\pi^-$	$\pm 33.5MeV/c^2$	<150
$D^0 \to K^\pm\pi^\mp\pi^\mp\pi^\pm$	$\pm 17MeV/c^2$	<150
$D^\pm \to K_S^0\pi^\pm$	$\pm 3\sigma$	$< 200(K), 150(\pi)$
$D^0 \to K^\pm\pi^\mp\pi^\mp\pi^\pm$	$\pm 3\sigma$	<200

Table A.1: Cuts on the reconstructed D^0masses

in Chapter 3, section 4.4.3 - only $K_S^0 \to \pi^+\pi^-$candidates are considered. In addition, the angle between the flight direction and the momentum vector of the K_S^0 must be less than $200mr$, the χ^2 of the vertex fit must be less than 0.001 and its vertex must be at least 2mm away from the primary vertex of the event. $\pi^\pm$ are selected from the *GoodTracksLoose* list, with the appropriate mass asignment (except in the case $D^0 \to K^\pm\pi^\mp\pi^\mp\pi^\pm$, where *GoodTracksVeryLoose* is used). $K^\pm$ are selected from the *SMSNotAPion* list.

The (mode dependent) cuts on the reconstructed D^0 masses and on the momenta of the $K^\pm$ and $\pi^\pm$[1] are shown in table A.1. In addition, all D^0 candidates are required to have momentum greter than $1.3GeV/c$ in the $\Upsilon(4S)$ frame. They are also required to have a χ^2 greater than 0.1 when a vertex fit is applied. In addition, the decay $D^0 \to K^\pm\pi^\mp\pi^0$ is reconstructed when it decays via $K^-\rho^+$, requiring the $\pi^0\pi^+$ mass to be within $150MeV$ of the nominal ρ mass and the K^- ρ^+ angle in the $\pi^0\pi^+$ centre of mass ,$\theta^*_{K\pi}$, to satisfy $|\cos\theta^*_{K\pi}| > 0.4$.

A.2 $D^{*\pm}$ Reconstruction

$D^{*\pm}$candidates are reconstructed from the mode $D^0\pi^\pm$. D^0 candidates are selected as described in section A.1. $\pi^\pm$ candidates are taken from *GoodTracksVeryLoose*.

The momentum of the pion must be between 70 and $450MeV/c$ in the

[1]When $D^0 \to K^\pm\pi^\mp$ is used in the reconstruction of $\overline{B}^0 \to D^{*+}\pi^-$ or $D^{*+}\rho^-$ a momentum cut of $100MeV$ is used instead.

Decay Mode	Branching Ratio ($\times 10^{-3}$)
$B^0 \to D^{*\pm}\pi^{\mp}$	2.7
$B^0 \to D^{*\pm}\rho^{\mp}$	7.0
$B^0 \to D^{*\pm}a_1^{\mp}$	12.2
$B^0 \to D^{\pm}\pi^{\mp}$	3.0
$B^0 \to D^{\pm}\rho^{\mp}$	8.2
$B^0 \to D^{\pm}a_1^{\mp}$	6.0

Table A.2: Hadronic B^0 modes and their Branching ratios

$\Upsilon(4S)$ frame. The invariant mass of the combination must be within $\pm 3\sigma$ of the nominal $D^{*\pm}$ mass ($2009.93 MeV/c^2$). The mass difference between the reconstructed $D^{*\pm}$ candidate and the reconstructed $D^{\pm}$ candidate must be between 130 and 160 MeV/c^2.

A.3 B^0 Reconstruction

The modes used to reconstruct B^0s are shown in table A.2.

Tracks that pass the *GoodTracksLoose* criteria and have momenta greater than $500 MeV/c$ are used as $\pi^{\pm}$ candidates. ρ^{+}s are reconstructed by pairing a charged track (*GoodTracksLoose*) and a π^0 candidate (as described in Chapter 4, section 4.4.1), both with momentum greater than $200 MeV/c$ and requiring that the invariant mass be within $\pm 150 MeV/c^2$ of the PDG2000 $\rho^{\pm}$ mass. $a_1^{\pm}$ candidates are reconstructed from three charged tracks from the *GoodTracksLoose* list and are required to have an invariant mass between 1.0 and 1.6 GeV/c^2, as well as having a $\chi^2 > 0.1\%$ when a vertex fit is performed.

A.4 Event Shape

For each event, R_2 is required to be less than 0.5. In addition, a cut is performed on the 'thrust angle', θ_{th} of the $B^0 \to D^{\pm}X$ modes. These have higher background because they lack the distinctive presence of a soft pion. θ_{th} is defined as the angle between the thrust axis of the particles which form the reconstructed B candidate and the thrust axis of the remaining tracks

Mode	$\|\cos\theta_{th}\|$ cut
$B^0 \to D^{\pm}\pi^{\mp}$	< 0.9
$B^0 \to D^{\pm}\rho^{\mp}$	< 0.8
$B^0 \to D^{\pm}a_1^{\mp}$	< 0.7

Table A.3: Thrust angle cuts for each B decay mode.

and calorimieter clusters, in the $\Upsilon(4S)$ rest frame. $|\cos\theta_{th}|$ is essentially flat for $B\overline{B}$ events (which are produced almost at rest in the $\Upsilon(4S)$ frame) and peaks strongly at 1 for continuum events (which are much more jet like in character). The cuts are mode dependent, and are shown in Table A.3.

A.5 ΔE and M_{ES} cuts

The ΔE and M_{ES} resolutions vary between modes. They are shown in Table A.4. The signal regions are defined with 2.5σ cuts in both.

A.6 The Selected B_{flav} Sample

The energy substsituted mass in the signal ΔE region is shown in Fig A.1 for the entire B_{flav} sample (before tagging). There are a total of 9794 ± 203 events in this sample.

B^0mode	D mode	$\sigma_{\Delta E}$	$\sigma_{M_{ES}}$
$B^0 \to D^{*\pm}\pi^{\mp}$	$D^0 \to K^{\pm}\pi^{\mp}$	19.2 ± 1.0	2.7 ± 0.1
“	$D^0 \to K^{\pm}\pi^{\mp}\pi^0$	22.4 ± 1.7	3.1 ± 0.2
“	$D^0 \to K^0_S\pi^+\pi^-$	16.7 ± 2.2	2.8 ± 0.2
“	$D^0 \to K^{\pm}\pi^{\mp}\pi^{\mp}\pi^{\pm}$	18.0 ± 1.0	2.8 ± 0.1
$B^0 \to D^{*\pm}\rho^{\mp}$	$D^0 \to K^{\pm}\pi^{\mp}$	23.2 ± 2.9	3.0 ± 0.2
“	$D^0 \to K^{\pm}\pi^{\mp}\pi^0$	26.7 ± 3.3	2.8 ± 0.2
“	$D^0 \to K^0_S\pi^+\pi^-$	not available	3.6 ± 0.1
“	$D^0 \to K^{\pm}\pi^{\mp}\pi^{\mp}\pi^{\pm}$	25.1 ± 3.2	3.1 ± 0.2
$B^0 \to D^{*\pm}a_1^{\mp}$	$D^0 \to K^{\pm}\pi^{\mp}$	17.0 ± 1.3	2.8 ± 0.2
“	$D^0 \to K^{\pm}\pi^{\mp}\pi^0$	18.5 ± 0.6	3.0 ± 0.3
“	$D^0 \to K^0_S\pi^+\pi^-$	21.6 ± 4.0	2.7 ± 0.7
“	$D^0 \to K^{\pm}\pi^{\mp}\pi^{\mp}\pi^{\pm}$	12.8 ± 1.3	2.9 ± 0.2
$B^0 \to D^{\pm}\pi^{\mp}$	$D^{\pm} \to K^0_S\pi^{\pm}$	18.5 ± 0.6	2.7 ± 0.1
“	$D^{\mp} \to K^{\pm}\pi^{\mp}\pi^{\mp}$	15.6 ± 1.3	2.8 ± 0.2
$B^0 \to D^{\pm}\rho^{\mp}$	$D^{\pm} \to K^0_S\pi^{\pm}$	34.7 ± 2.5	3.0 ± 0.1
“	$D^{\mp} \to K^{\pm}\pi^{\mp}\pi^{\mp}$	not available	2.9 ± 0.3
$B^0 \to D^{\pm}a_1^{\mp}$	$D^{\pm} \to K^0_S\pi^{\pm}$	12.1 ± 0.8	2.7 ± 0.2
“	$D^{\mp} \to K^{\pm}\pi^{\mp}\pi^{\mp}$	12.5 ± 2.8	2.3 ± 0.4

Table A.4: ΔE and M_{ES} Resolutions for Hadronic B decays

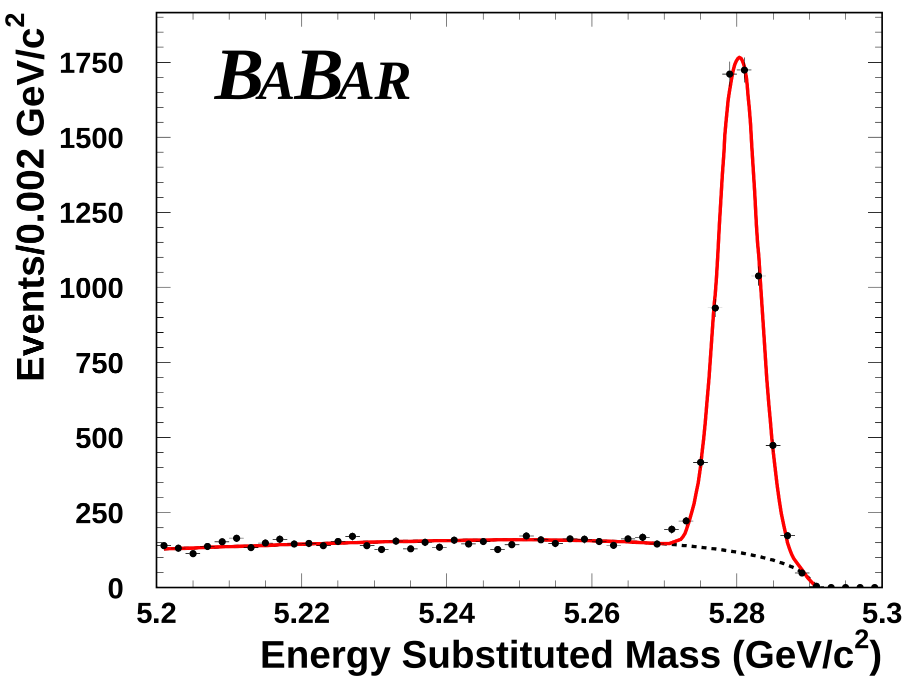

Figure A.1: The energy substituted mass of the B_{flav} sample

Appendix B

Output values of the $\sin 2\beta$ fit

There are 45 free parameters to the Maximum Likelihood fit. The value of $\sin 2\beta$ is returned as 0.76 ± 0.52. The other 44 parameters (11 of which are the same parameters allowed to take different values between run1 and run2) are shown here, in tables B.1 to B.7.

Parameter	Fitted value
Scale(core)	1.25 ± 0.11
$\delta(\Delta t)$ lepton(core)	0.056 ± 0.128
$\delta(\Delta t)$ Kaon(core)	-0.273 ± 0.079
$\delta(\Delta t)$ NT1(core)	-0.153 ± 0.152
$\delta(\Delta t)$ NT2(core)	-0.344 ± 0.113
$\delta(\Delta t)$ tail	-1.5454 ± 1.5618
f(tail)	0.066 ± 0.059
f(outlier)	0.006 ± 0.003

Table B.1: Run 1 Signal Resolution Function

Parameter	Fitted value
Scale(core)	1.14 ± 0.12
$\delta(\Delta t)$ lepton(core)	0.056 ± 0.162
$\delta(\Delta t)$ Kaon(core)	-0.196 ± 0.100
$\delta(\Delta t)$ NT1(core)	-0.346 ± 0.213
$\delta(\Delta t)$ NT2(core)	-0.197 ± 0.158
$\delta(\Delta t)$ tail	-3.3534 ± 3.4765
f(tail)	0.033 ± 0.048
f(outlier)	0.000 ± 0.002

Table B.2: Run 2 Signal Resolution Function

Parameter	Fitted value
$< D >$, lepton	0.821 ± 0.027
$< D >$. kaon	0.649 ± 0.020
$< D >$, NT1	0.556 ± 0.042
$< D >$, NT2	0.299 ± 0.038
ΔD, lepton	-0.026 ± 0.045
ΔD, kaon	0.036 ± 0.031
ΔD, NT1	-0.124 ± 0.067
ΔD, NT2	0.098 ± 0.056

Table B.3: Signal Dilutions

Parameter	Fitted value
τ, mixing background	$(1.28 \pm 0.08) ps$
$f(\tau = 0)$, CP background	0.682 ± 0.163
$f(\tau = 0)$, B_{flav} background, lepton	0.312 ± 0.097
$f(\tau = 0)$, B_{flav} background, kaon	0.652 ± 0.037
$f(\tau = 0)$, B_{flav} background, NT1	0.613 ± 0.058
$f(\tau = 0)$, B_{flav} background, NT2	0.640 ± 0.044

Table B.4: Background properties

Parameter	Fitted value
Scale (core)	1.491 ± 0.040
$\delta(\Delta t)$ core	-0.151 ± 0.042
f(outlier)	0.0174 ± 0.005

Table B.5: Run 1 background resolution function

Parameter	Fitted value
Scale (core)	1.329 ± 0.044
$\delta(\Delta t)$ core	0.022 ± 0.037
f(outlier)	0.017 ± 0.005

Table B.6: Run 2 background resolution function

Parameter	Fitted value
D, lepton, $\tau = 0$	0.343 ± 0.277
D. kaon, $\tau = 0$	0.451 ± 0.035
D, NT1, $\tau = 0$	0.255 ± 0.095
D, NT2, $\tau = 0$	0.102 ± 0.054
D, lepton, $\tau \neq 0$	0.323 ± 0.142
D, kaon, $\tau \neq 0$	0.242 ± 0.060
D, NT1, $\tau \neq 0$	0.054 ± 0.140
D, NT2, $\tau \neq 0$	0.098 ± 0.090

Table B.7: Background Dilutions

Appendix C

Inputs to CKMFitter

Tables C.1, C.2, C.3 and C.4 contain the parameters used to provide the constraints in figures 7.1 and 7.2. A full rundown of the sources for these values is given in [37].

CKM Parameter	Value
$\|V_{ud}\|$	0.97394 ± 0.00089
$\|V_{us}\|$	0.2200 ± 0.0025
$\|V_{ub}\|$	$(3.49 \pm 0.27 \pm 0.55) \times 10^{-3}$
$\|V_{cd}\|$	0.224 ± 0.014
$\|V_{cs}\|$	0.969 ± 0.058
$\|V_{cb}\|$	$(40.75 \pm 0.40 \pm 2.0) \times 10^{-3}$

Table C.1: CKM Parameters

CP and Mixing Observable	Value
$\|\epsilon_K\|$	$(2.271 \pm 0.017) \times 10^{-3}$
Δm_d	$(0.487 \pm 0.014) ps^{-1}$
Δm_s	WA (Beaty2000) amplitude spectrum

Table C.2: CP violating and Mixing Observable

Experimental parameters	Value
m_t	$(166 \pm 5) GeV$
m_K	$(493.677 \pm 0.016) MeV$
Δm_K	$(3.4885 \pm 0.0008) \times 10^{15} GeV$
m_{B_d}	$(5.2794 \pm 0.005) GeV$
m_{B_s}	$(5.3696 \pm 0.0024) GeV$
m_W	$(80.419 \pm 0.056) GeV$
G_F	$1.16639 \pm 0.00001) \times 10^{-5} GeV^{-2}$
f_K	$(159.8 \pm 1.5) MeV$

Table C.3: Experimental Parameters

Theoretical Parameter	Value
m_e	$(1.3 \pm 0.1) GeV$
B_K	$0.87 \pm 0.06 \pm 0.13$
η_{cc}	1.38 ± 0.53
η_{ct}	0.47 ± 0.04
η_{tt}	0.574 ± 0.004
$\eta_B(\overline{MS})$	0.55 ± 0.01
$f_{B_d \sqrt{B_d}}$	$(230 \pm 28 \pm 28) MeV$
ξ	$1.16 \pm 0.03 \pm 0.05$

Table C.4: Theoretical Parameters

Bibliography

[1] "Observation of CP Violation in the B^0 Meson System." By BaBar Collaboration (B. Aubert et al.) Phys.Rev.Lett.87:091801,2001

[2] "Evidence for the 2 Pi Decay of The K(2)0 Meson" By J.H. Christenson, J.W. Cronin, V.L. Fitch, R. Turlay Published in Phys.Rev.Lett.13:138-140,1964

[3] "CP Violation in the Renormalizable Theory of Weak Interaction". By M. Kobayashi, T. Maskawa Published in Prog.Theor.Phys.49:652-657,1973

[4] "Exclusive Semileptonic Decays of Heavy Mesons" By M. Wirbel, B. Stech, Manfred Bauer Published in Z.Phys.C29:637,1985

[5] "Exclusive Nonleptonic Decays of D, $D(S)$, and B Mesons" By Manfred Bauer, B. Stech (Heidelberg U.), M. Wirbel (Dortmund U.) Published in Z.Phys.C34:103,1987

[6] "Measurement of Branching Fractions for Exclusive B decays to Charmonium Final States" By BaBar Collaboration (B. Aubert et al.) Phys.Rev.D Pending, e-Print Archive: hep-ex/0107025

[7] "Observation of Large CP Violation in the Neutral B Meson System." By Belle Collaboration (K. Abe et al.) Phys.Rev.Lett.87:091802,2001

[8] "Factorization and SU(2) Heavy Flavour Symmetry for B-Meson Decays Producing Charmonium" M. Gourdin, Y. Y. Keum and X. Y. Pham Published in Phys.Rev.D52:1597-1613,1995

[9] "Factorization, Charming Penguins and all that" M. Ciuchini, R. Contino, E. Franco, G. Martinelli, L. Silvestrini Nucl.Instrum.Meth.A408:28-32,1998

[10] "Factorization Theorems, Effective Field Theory, and Nonleptonic Heavy Meson Decays" Tsung-Wen Yeh, Hsiang-nan Li Phys.Rev.D56:1615-1631,1997

[11] "The BaBar physics book: Physics at an asmmetric B factory" The BaBar Collaboration (Editors P.F. Harrison and H.R. Quin) Section 1.2.3 (1998)

[12] "The Review of Particle Physics" D.E. Groom *et al* (The particle Data Group) Eur.Phys.Jour.C15, 1 (2000)

[13] "Unitary Symmetry and Leptonic Decays" By N. Cabibbo Published in Phys.Rev.Lett.10:531-532,1963

[14] "The BaBar physics book: Physics at an asmmetric B factory" The BaBar Collaboration (Editors P.F. Harrison and H.R. Quin) Section 1.4.1 (1998)

[15] "B Decays - Introduction and Overview" B Decays Editor Sheldon Stone (1994)

[16] *"B Decays and CP Violation"* M. Neubert Int.J.Mod.Phys.A11:4173-4240,1996

[17] "The BaBar physics book: Physics at an asmmetric B factory" The BaBar Collaboration (Editors P.F. Harrison and H.R. Quin) Section 1.2.4 (1998)

[18] "Parameterization of the Kobayashi-Maskawa Matrix" Lincoln Wolfenstein Published in Phys.Rev.Lett.51:1945-1947,1983

[19] "Commutator of the Quark Mass matricies in the Standard Electroweak Model and a Measure of Maximal CP Nonconservation" C. Jarlskog Phys.Rev.Let.55:1039-1042,1985

[20] "The BaBar physics book: Physics at an asmmetric B factory" The BaBar Collaboration (Editors P.F. Harrison and H.R. Quin) Section 5.1.1.1

[21] "The BaBar physics book: Physics at an asmmetric B factory" The BaBar Collaboration (Editors P.F. Harrison and H.R. Quin) Section 1.5.1

[22] "Measurement of the Number of $\Upsilon(4S)$ Mesons Produced in Run 1 (B Counting)" Chris Hearty, BaBar Analysis Document 134

[23] "Measurement of the CP-violation parameter eta(00) using tagged anti-K0 and K0" A. Angelopoulos et al. (CPLEAR collaboration), published in Phys.Lett. B 420 (1998), 191

[24] "Shower Shape Analysis and Longitudinal Sampled Electromagnetic Calorimeters" By H. Grassmann, H.G. Moser (Aachen, Tech. Hochsch.). PITHA 84-33, Nov 1984. 18pp. Published in Nucl.Instrum.Meth.A237:486,1985

[25] "Event Shapes in e^+e^- Annihilation" G. Fox and S. Wolfram Published in Nucl.Phys. B149, 413,1979

[26] "Reconstruction of B Mesons" ARGUS Collaboration (H. Albrecht et al.) Published in Phys.Lett.B185:218,1987

[27] "Study of pi0 Efficiencies in RUN1 Data using Tau 1-on-1 Decays" BaBar Analysis Document 196 (T. Colberg and C. Touramanis)

[28] "The BaBar Detector" By BABAR Collaboration (B. Aubert et al.). Submitted to Nucl.Instrum.Meth. e-Print Archive: hep-ex/0105044

[29] "tFit - a program to fit decay time (difference) distributions to study $B^0/B^{\pm}$ lifetimes, $B^0\overline{B^0}$ Oscillations and CP asymmetry parameters" BaBar Analysis Document 101 (S. Prell et al.)

[30] "Supporting document for the summer, 2001 sin2β analysis" (J. Beringer et al.) BaBar Analysis Document 205

[31] "A Measurement of sin 2 Beta From B —> J / PSI K0(S) with the CDF Detector. By CDF Collaboration (T. Affolder et al.). Published in Phys.Rev.D61:072005,2000 e-Print Archive: hep-ex/9909003

[32] "Study of the *CP* Asymmetry of B0 —> J / PSI K0(S) Decays in ALEPH". By ALEPH Collaboration (R. Barate et al.) Published in Phys.Lett.B492:259-274,2000 e-Print Archive: hep-ex/0009058

[33] "Investigation of *CP* Violation in B0 —> J / PSI K0(S) Decays at LEP. By OPAL collaboration (K. Ackerstaff et al.) Published in Eur.Phys.J.C5:379-388,1998 e-Print Archive: hep-ex/9801022

[34] "Measurement of Branching Fractions for Two-Body *B* Meson Decays with Charmonium at Belle" By Belle Colaboration (K.Abe et al.) BELLE-CONF-0101

[35] "CKM Fitter" http://ckmfitter.in2p3.fr/ckm_wellcome.html

[36] "A New Approach to a Global Fit of the CKM Matrix" A. Hocker et al. Published in Eur.Phys.J. C21: 225-259,2001 e-Print Archive: hep-ph/0104062

[37] http://www.slac.stanford.edu:/~laplace/ckmfitter/ckm_measure.html